UC Berkeley
UC Berkeley Electronic Theses and Dissertations

Title
Physical Interactions Between Free-Floating Macrophytes and Environmental Flows

Permalink
https://escholarship.org/uc/item/5zd7m7q8

Author
Downing-Kunz, Maureen Allison

Publication Date
2011

Peer reviewed|Thesis/dissertation

eScholarship.org Powered by the California Digital Library
University of California

Physical Interactions Between Free-Floating Macrophytes and Environmental Flows

by

Maureen Allison Downing-Kunz

A dissertation submitted in partial satisfaction of the
requirements for the degree of

Doctor of Philosophy

in

Engineering - Civil and Environmental Engineering

in the

Graduate Division

of the

University of California, Berkeley

Committee in charge:

Professor Mark T. Stacey, Chair
Professor Evan A. Variano
Professor Mimi A. R. Koehl

Fall 2011

Physical Interactions Between Free-Floating Macrophytes and Environmental Flows

Copyright © 2011
by
Maureen Allison Downing-Kunz

Abstract

Physical Interactions Between Free-Floating Macrophytes and Environmental Flows

by

Maureen Allison Downing-Kunz

Doctor of Philosophy in Engineering - Civil and Environmental Engineering

University of California, Berkeley

Professor Mark T. Stacey, Chair

Free-floating macrophytes are unique in that they live at the air-water interface, leading to the development of two distinct structural assemblages, or canopies: leaf canopies comprising above-water structures and root canopies comprising submerged structures. Certain species are considered invasive weeds, owing to characteristics such as high growth rates aided by asexual reproduction, formation of dense floating mats that out-compete other plant species, and unanchored root systems that allow dispersal by passive drifting. Invasions of these weeds harm native ecosystems and impede human activities. This research examines physical interactions between free-floating macrophytes and surrounding air and water flows to better understand the fluid-dynamic effects of free-floating macrophytes and the transport mechanisms that govern ecological dispersal.

Laboratory and field experiments were performed to address these goals. In the laboratory, experiments were conducted on leaf and root canopies of the free-floating macrophyte *Eichhornia crassipes* (Mart.) Solms to both measure flow-induced forces and observe surrounding flow fields. For a given raft geometry, forces and drag coefficients in water exceeded those in air. Over similar Reynolds number (Re) regimes, water drag coefficients decreased with increasing Re while air drag coefficients were relatively constant. Force-velocity relationships indicate root canopies reconfigured by streamlining in higher flow velocities while leaf canopies did not. Root canopy streamlining is further explained through biomechanical testing: the major vegetative structures of *E. crassipes* (roots, stolons, and petioles) had similar moduli of elasticity but second moments of area were three orders of magnitude smaller in roots compared to stolons or petioles, leading to significantly lower flexural rigidity in roots. Flow interactions with the root canopy differed for an individual plant compared to a raft assemblage. These results suggest that water currents are the dominant mechanism for *E. crassipes* dispersal.

Based on flow field observations in the laboratory, the presence of *E. crassipes* rafts caused deflection of air and water flows around the canopy structures and increased turbulence in both fluids. In both air and water, increased Reynolds stress and turbulent kinetic energy were observed beyond 50% of canopy lengths, culminating in large wake regions downstream. As upstream water velocity increased, the distance to fully-developed conditions decreased and turbulence levels increased for root canopies. In water, vertical profiles of mean streamwise velocity beyond 50% of root canopy length featured inflection points, suggesting mixing layer development; the vertical turbulent structure featured sweeps, coherent vortices, and increased mixing efficiency along the root canopy edge. These findings are analogous to mixing layers seen in submerged aquatic vegetation canopies. Although turbulent mixing was increased outside the root canopy, limited turbulent exchange was observed between the root canopy and the open water. This implies low momentum flux across the canopy-water interface; therefore in root canopies having similar structure to *E. crassipes*, residence time is expected to be dominated by horizontal advection. In air, the spatial development of the mean streamwise velocity profile generally agreed with a model of flow adjustment developed for terrestrial vegetation canopies. As leaf canopy length increased, turbulence levels increased, particularly in the downwind wake region. Comparing the flow fields in water and air for one particular raft, the root canopy induced a greater flow acceleration and generated a larger-intensity wake region that extended further downstream. These results suggest the fluid-dynamic effects of the root canopy exceed those of the leaf canopy.

Field experiments were performed in a tidal channel to observe free-floating macrophyte transport under varying water velocities and nearly-constant wind velocities. A free-floating macrophyte raft was equipped with a global positioning system and an acoustic Doppler velocimeter to measure raft position and relative water velocity. Results indicate that water currents dominated raft transport during ebb and flood tides, and that wind dominated transport during slack tide. Raft and water velocities were correlated during ebb and flood tides and anticorrelated during slack tide. During ebb tide, wind opposed one component of the raft velocity, reducing its magnitude compared to water velocity. In contrast, during flood tide, wind was aligned with one component of the raft velocity, leading to raft velocities that exceeded water velocities. These field observations corroborate the laboratory drag force measurements, suggesting water currents, when present, are the dominant dispersal mechanism for free-floating macrophytes. However, wind plays an important secondary role and must be considered along with ecosystem geometry. This research builds upon existing vegetation canopy studies and provides the foundation for a predictive model of free-floating macrophyte dispersal based on physical processes.

for Dad

Contents

List of Figures

List of Tables

Acknowledgements

Many people have been instrumental in the completion of this endeavor. First and foremost I thank my advisor, Professor Mark Stacey, for his guidance and support at every stage of my graduate studies. He regularly dispensed wisdom, energy, and compassion, ingredients vital to my successful completion of this degree. He pushed me to dismiss my self-imposed limits and to embrace my abilities and training. His enthusiasm for gaining and sharing knowledge has made my time at Berkeley truly outstanding.

I sincerely thank Professors Mimi Koehl and Evan Variano for their thoughtful discussions during early phases of this research. Their helpful support and feedback has tremendously improved the quality of this dissertation. In addition, I am grateful to Professors Jim Hunt, Tina Katopodes Chow, and Kara Nelson for serving as exam committee members and encouraging my work. Professor Joe Hagerty was an early source of inspiration through his role as advisor of my M.Eng. project, during which he exuded a contagious excitement for both the academic setting and scholarly research. Throughout my doctoral program, he remained an important source of advice, encouragement, and support.

I was lucky to participate in such a supportive and exciting research group as the Environmental Fluid Mechanics Lab at Berkeley. In particular, Lissa MacVean, Megan Daniels, Mary Cousins, Rudi Schuech, Wayne Wagner, Audric Collignon, Rusty Holleman, Andreas Brand, Bowen Zhou, Cristina Poindexter, Ian Tse, Megan Williams, Rebecca Leonardson, Paul Koster Van Groos, and Maureen Martin have all provided assistance and helpful discussions. Outside of this group, fellow students Andrew Tinka, Vi Rapp, Eve Robinson, Yonatan Munk, Dennis Evangelista, Robby Zeller, Christian Braudrick, and Tom Libby provided both equipment and helpful assistance during experimental setup. The help of Berkeley staff members Phillip Wong and Negassi Hadgu is greatly appreciated. I am grateful to Professors Alex Bayen, Bill Dietrich, Bob Full, Mimi Koehl, Kara Nelson, and Evan Variano for allowing me use of their equipment.

I was even luckier to find wonderful friends outside of the lab that shared my interests in physical as well as intellectual pursuits. Emma Worldpeace, Jen Aengst, Tsering Alleyne, Jack Tisdale, Anand Varma, Sumitra Nadarajah, Stacy Marple, and Rob Dahl have all inspired me in both aspects, adding an exciting and important dimension to my life during graduate school.

I am blessed with a wonderfully-supportive family; in particular, my mom Susan, my late grandmother Leah, and my aunts Karen and Monica have encouraged and supported me throughout graduate school by taking an active interest in my studies. My mom has been a tremendous source of encouragement and continues to be a model of the strong and independent woman I hope to become. My dad Martin bestowed upon me the love of learning and inspired scientific inquiry from an early age. Although his physical presence was sorely missed throughout my graduate studies, his spirit did and continues to both encourage and inspire.

Finally, I extend my deepest and most sincere gratitude to Mark French. He planted the initial seed of my higher learning and patiently nurtured my development as a scientist. Throughout my time at Berkeley he provided unwavering support, guidance, and love. He provided crucial emotional support through the hardest of times, and celebrated even the smallest of achievements along the way. He has been a model of kindness, dedication, and grace. Without his involvement this goal could not be realized.

Curriculum Vitæ

Maureen Allison Downing-Kunz

Education

2004	B.S., Civil and Environmental Engineering University of Louisville
2004	M.Eng., Civil and Environmental Engineering University of Louisville
2007	M.S., Civil and Environmental Engineering University of California, Berkeley
2011	Ph.D., Civil and Environmental Engineering University of California, Berkeley

Chapter 1

Introduction

Free-floating macrophytes are macroscopic aquatic plants with buoyant leaves and unanchored roots that live at the water surface. This research explores physical interactions between free-floating macrophytes and the surrounding wind and water flows. Although these flow-biota interactions are fundamental controls on both ecological dispersal and water quality impacts, they are poorly understood. This research fills a knowledge gap by exploring these interactions in two contexts: *1*) effects of flow on free-floating macrophytes (i.e., fluid-dynamic drag); and *2*) effects of free-floating macrophytes on flow (i.e., mean and turbulent flow structure).

1.1 Motivation

Primarily found in freshwater systems, free-floating macrophytes play a structuring role in their ecosystems (*Meerhoff et al.* 2003) by mediating trophic interactions (e.g., *Toft et al.* 2003; *Padial et al.* 2009), influencing nutrient dynamics (e.g., *Mazzeo et al.* 1995), and moderating species succession (*Sculthorpe* 1967; *Adams et al.* 2002). Examples include duckweed, *Lemna spp.*; water fern, *Salvinia spp.*; water lettuce, *Pistia spp.*; and water hyacinth, *Eichhornia spp.* (*Mackie* 2004). Free-floating macrophytes typically grow in dense mats along the margins of water bodies (Figure 1.1) and prefer lower-energy environments (*Azza et al.* 2006). Unstable hydrologic conditions, as during storms or floods, can break segments of this fringing vegetation and form smaller, free-floating rafts that are held together by a tangled mass of roots and stems and transported throughout their ecosystem by wind and water currents (*Gay* 1960; *Adams et al.* 2002). In addition to expanding their own species distribution, free-floating macrophyte mats have been identified as an important mechanism (known as rafting) for the dispersal for a wide range of species of flora and fauna that are often non-native (e.g., *Shaffer et al.* 1995; *Adams et al.* 2002; *Azza et al.* 2006; *Thiel and Haye* 2006).

Several free-floating macrophyte species (in particular, *Eichhornia crassipes* (Mart.) Solms, *Pistia stratiotes* L., and *Salvinia molesta* D.Mitch.) have exceptionally high growth rates under eutrophic conditions and can rapidly colonize aquatic ecosystems, leading to their distinction as noxious aquatic weeds (*Cook* 1990; *Heard and Winterton* 2000; *Henry-Silva et al.* 2008). For these three species in particular, high growth rates are due in part to asexual reproduction through the formation of ramets (*Cook* 1990). In *E. crassipes*, sexual reproduction is known to be rare despite widespread flowering; however, seeds can survive in dormancy for 15-20 years (*Penfound and Earle* 1948; *Malik* 2007). *E. crassipes* is one of the fastest-growing plant species in the world, capable of doubling in mat size every two weeks (*Penfound and Earle* 1948). The dense mats formed by these species cover large areas of the water surface, out-competing less vigorous plants for both light and space and interfering with human utilization of water resources.

The socioeconomic costs and environmental impacts of invasions of these aquatic weed are high. Problems associated with invasions include sediment deposition, native species displacement, biodiversity reduction, water quality reduction, increased evapotranspiration, serving as habitat for disease vectors, and obstruction of navigation, irrigation, and hydroelectric facilities (*Gopal* 1987; *Toft et al.* 2003; *Opande et al.* 2004; *Bicudo et al.* 2007; *Chukwuka and Uka* 2007; *Coles and Kabatereine* 2008). For the case of *E. crassipes,* water quality is reduced by lowering dissolved oxygen content, pH, and bicarbonate alkalinity (*Gopal* 1987). *E. crassipes* further modifies its environment by changing the functional characteristics of an ecosystem. For example, in a study of the functional roles of *E. crassipes* compared to a native free-floating macrophyte (*Hydrocotyle umbellata* L.) in the Sacramento River-San Joaquin River Delta of California, *Toft et al.* (2003) found that native invertebrates, an important part of native fish diets, were more likely to establish in the native vegetation.

Given the negative impacts of aquatic weeds on ecosystem structure and functioning, numerous studies have been undertaken to explore these plants in various contexts: growth rates for varying environmental conditions (*Boyd and Scarsbrook* 1975; *Lugo et al.* 1978; *Wolverton and McDonald* 1979; *Reddy et al.* 1989; *Henry-Silva et al.* 2008); controlling plant spread via mechanical (*Greenfield et al.* 2007), biological (*Jayanth* 1988), and chemical (*Gopal* 1987) means; and alternative uses including agriculture, energy, and phytoremediation (e.g., wastewater treatment and metals uptake) (*Gunnarsson and Petersen* 2007; *Malik* 2007). Motivated by a desire to mitigate existing invasions and prevent future invasions of aquatic weeds, there have been several predictive modeling efforts for local population dynamics (e.g., *Mitsch* 1976; *Wilson et al.* 2005). Although it is well known that free-floating macrophytes

Figure 1.1: Photographs of *E. crassipes* in Ihema Lake, Rwanda. Free-floating macrophytes grow in dense mats along shorelines that extend into open water (top and bottom left); broken segments of these mats form free-floating rafts of varied sizes (top, in open water) that disperse in response to wind and water currents. *E. crassipes* has leaves and buoyant stems extending above the water surface and dense, feathery root structures extending below (bottom right). Photographs taken by the author.

disperse to new areas by passive drifting on wind and water currents (e.g., *Gay* 1960; *Adams et al.* 2002; *Ngari et al.* 2009), few predictive models actually consider these environmental forcing mechanisms and therefore severely under predict the spatial distribution of an invasion (*Higgins and Richardson* 1996). Additionally, despite the varied water quality impacts of these weeds, little is known of the hydrodynamic interactions that control them.

For free-floating macrophytes, both ecological dispersal and water quality impacts are caused by the interactions between plants and surrounding environmental flows. The objective of this research is improved understanding of flow-biota interactions in free-floating macrophytes, particularly: *1*) the relative importance of wind and water currents in free-floating raft transport; and *2*) the structure of the surrounding shear layers in air and water.

1.2 Floating Body Transport

Free-floating macrophytes exist at the interface of two very different fluids; the motions of a drifting mat are caused by the relative forcing of wind and water currents on its upper and lower faces. The coupling of air and water forcing is an interesting fluid dynamics problem and is not unique to free-floating macrophytes. Other pleuston include certain macroalga (e.g., *Sargassum* spp. and *Macrocystis* spp.) and marine invertebrates (e.g., *Physalia physalis* and *Velella velella*); other floating items of biotic origin include seeds, wood, vascular plants, and animal remains. Abiotic examples include plastic litter, tar lumps, sea ice, icebergs, and volcanic pumice. In general, mechanistic descriptions of floating body transport describe body acceleration based on an assumed force balance, of which fluid-dynamic drag is an essential component. Bulk drag coefficients (C_D) are commonly used to describe the efficiency of momentum transfer and relate flow velocity (U) to drag force (D) through the quadratic drag law (see, e.g., *Hoerner* 1965; *Batchelor* 2000)

$$C_D = \frac{2D}{\rho A U^2}, \tag{1.1}$$

where ρ is the density of the fluid and A is the characteristic area of the body.

Wind and water currents are often the dominant forcing mechanisms of floating objects, as has been shown for the transport of oil spills, pumice, and ice in the ocean (*Weber and Debernard* 2000; *Bryan et al.* 2004). Of these two mechanisms, the dominant one clearly depends on the fluid characteristics (e.g., density and velocity) but is also strongly related to body geometry and composition. For a body of uniform composition, its extent above the water surface (freeboard) relative to its depth below water surface (draft) is an important factor. In general, uniformly-composed bodies

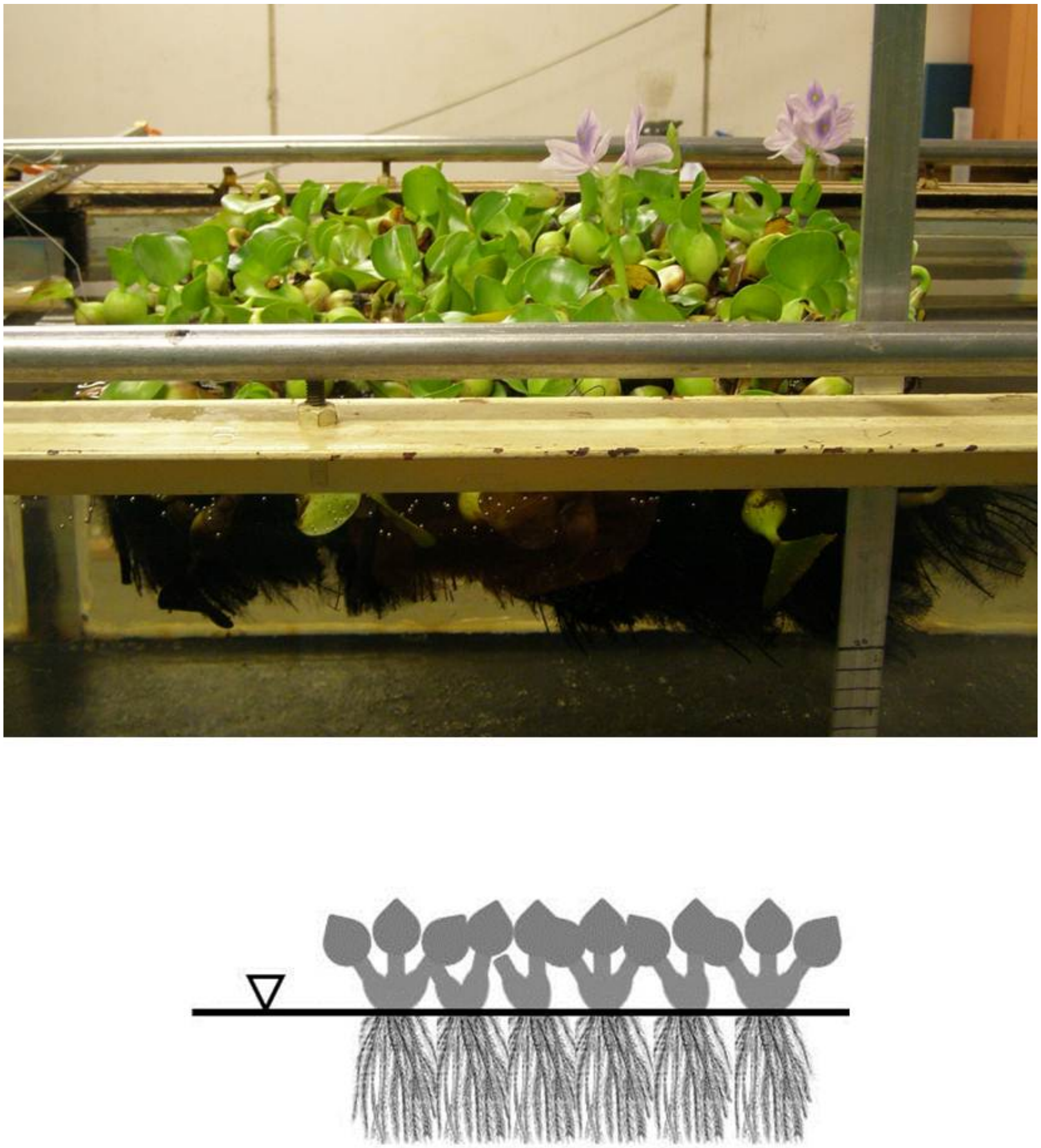

Figure 1.2: Example of free-floating macrophyte raft used in laboratory experiments (top), and simplified schematic showing leaf and root canopies extending above and below water surface, respectively (bottom).

with minimal freeboard (e.g., macroalgae) are dominated by water-driven transport (*Biber* 2007) while high-profile objects (e.g., sea ice, icebergs, *P. physalis* and *V. velella*) are dominated by wind-driven transport (*Thorndike and Colony* 1982; *Francis* 1991; *Iosilevskii and Weihs* 2009). Sea ice and icebergs, which typically have a low freeboard to draft ratio of 0.1-0.2, have been shown to be primarily driven by wind forcing at short timescales (i.e., days to weeks) and water current forcing at longer timescales (*Thorndike and Colony* 1982; *Smith* 1993). For free-floating macrophytes, this ratio of freeboard to draft is $O(1)$, but its above- and below-water structures are very different (Figures 1.1 & 1.2). Qualitative descriptions of free-floating macrophyte transport in the environment have suggested both wind and water forcing to be relevant, but suggest wind forcing is likely the dominant factor when present (*Gay* 1960; *Adams et al.* 2002). For free-floating macrophytes, the distinction between solid and porous bodies is relevant to the momentum transfer and merits additional consideration from the perspective of vegetation canopy flow.

1.3 Flow Dynamics of Vegetation Canopies

Vegetation canopies, the outer-most layer in an assemblage of plants, are essential to the exchange processes of momentum, heat, and mass with the surrounding fluid (*Yi* 2008). Drag is fundamental to these processes, creating velocity gradients and eddies that lead to momentum loss of the fluid. The effectiveness of canopy elements in extracting momentum from the surrounding flow depends on canopy characteristics such as geometry, spacing, flexibility, and arrangement (*Yi* 2008). Studies of vegetation canopies typically find deviations from the quadratic drag law (Equation (1.1)) such that the drag force varies with less than the velocity squared; this is caused by flexibility and reconfiguration of canopy elements in faster flows and results in decreasing relative drag force for increasing flow velocity (*Vogel* 1984; *Ennos* 1999; *Sand-Jensen* 2003).

It has long been recognized in atmospheric literature that turbulence in terrestrial vegetation canopies is dominated by large-scale motions produced by velocity gradients above the canopy (e.g., *Raupach and Thom* 1981); recent studies of submerged macrophyte canopies have found similar results (*Ackerman and Okubo* 1993; *Ghisalberti and Nepf* 2002), although stem-wake production can also be locally important (*Naden et al.* 2006). This body of research has led to the emerging view that flow structure in terrestrial and aquatic vegetation canopies is better described by a mixing layer rather than a rough boundary layer, as traditionally thought. This distinction has strong implications for mixing processes; a mixing layer is characterized by coherent eddies that are generated by inherent instabilities and result in greater momentum transfer in the vertical direction (across the canopy-water interface) than would otherwise be expected in boundary layer flows. This increased transport causes vegetation canopies to strongly affect environmental processes including fluxes of scalar constituents such as nutrients, heat, water vapor, CO_2, and dissolved oxygen, and transport of particulate matter.

Vegetation canopies have been studied in great detail, but existing studies consider plants that are fully immersed in a single fluid (e.g., grasses, crops, trees, and submerged macrophytes). Free-floating macrophytes have two canopies, each in a very different fluid (under the assumption the root assemblage is fundamentally similar to the leaf assemblage with respect to momentum exchange). The literature reviewed here suggests that the presence of free-floating macrophytes will give rise to mixing layers at both interfaces. For ecosystems heavily invaded by free-floating macrophytes (i.e., large surface area coverage), the presence of a mixing layer would be important for characterizing the hydrodynamics.

1.4 Thesis Overview

To gain a better understanding of the physical interactions between free-floating macrophytes and their surrounding flows, I conducted laboratory and field studies on live plants. Given the independent nature of the experiments conducted for this research, the thesis chapters are organized by the separate experiments.

In Chapter 2, I present a model for environmental transport of free-floating macrophytes along with laboratory measurements of flow-induced forces, concluding with discussion of implications for ecological dispersal. This chapter is adapted from published material (*Downing-Kunz and Stacey* 2011). In Chapters 3 and 4, detailed observations of mean and turbulent velocity structure in water and air, respectively, are presented along with implications for mass transport. Results from Chapter 3 have been submitted for publication (*Downing-Kunz and Stacey*, in review). In Chapter 5, I present field observations of free-floating macrophyte raft transport and relate these to the laboratory observations in Chapter 2. Finally, Chapter 6 contains a summary of the findings of this research.

Chapter 2

Flow-Induced Forces on Free-Floating Macrophytes

The distribution and abundance of free-floating macrophytes are the direct result of environmental flows. Despite the negative ecosystem impacts and high costs of control of free-floating aquatic weeds like *E. crassipes*, little is known about the physical processes that govern free-floating raft transport and resulting ecological dispersal. The objective of these experiments was to measure wind- and water-induced drag forces and determine wind and water drag coefficients using direct force measurements on *E. crassipes* rafts. In addition, I tested biomechanical properties of *E. crassipes* to further characterize the flow-biota interactions. Understanding these interactions is paramount to developing a physically-based model of *E. crassipes* dispersal.

2.1 Background

2.1.1 Dispersal and Spatial Dynamics

Dispersal, the movement of a species away from an existing population, is recognized as one of the most important processes in determining invasion success of non-native plants (*D'Antonio et al.* 2001). Dispersal occurs at a wide range of spatial scales; *Pauchard and Shea* (2006) suggest three scales are dominant: global long distance (dominated by human transport but also including bird transport and transoceanic drift), regional long distance (human-influenced but also including landscape corridors such as roads and rivers), and local dispersal (dominated by local environmental conditions such as water currents, winds, and nutrient availability).

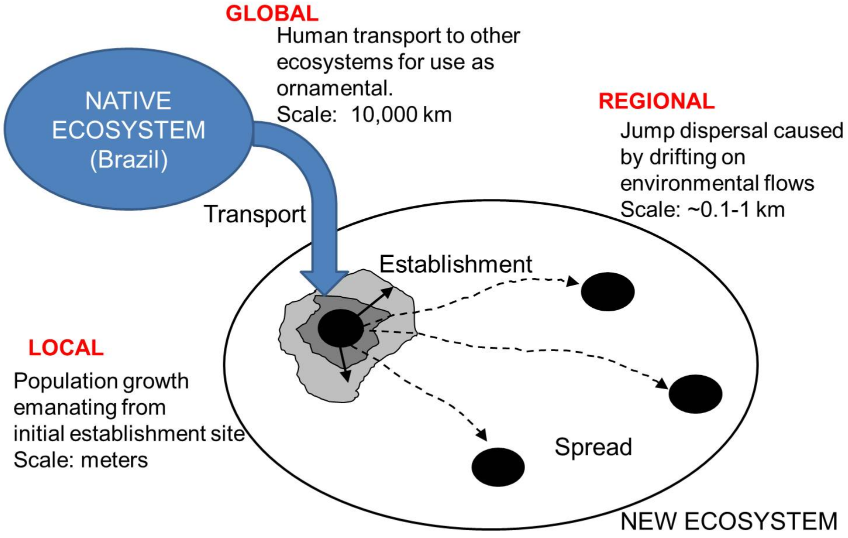

Figure 2.1: Schematic of geographic spread of invasive species, adapted to *E. crassipes*. Three important phases occur at different scales: *transport* from the native ecosystem to a new ecosystem at the global scale; *establishment*, during which the species adapts to the new ecosystem at the local scale; and *spread*, during which the species distribution expands throughout the ecosystem at the regional scale. For *E. crassipes*, transport is human-induced, establishment is rapid under favorable conditions, and spreading occurs by drifting at the water surface, forced by wind and water currents. Illustration adapted from *Lockwood et al.* (2007).

For non-native species, dispersal at each of these scales is important to its successful invasion of a new ecosystem; from a management perspective, successful control requires an understanding of the dispersal mechanisms at each scale. Toward this end, studies of invasion processes need to be based on a multi-scale approach, specifically at the local and regional scales (*Pauchard and Shea* 2006). In the case of invasive free-floating macrophytes, the local scale has been studied extensively in the form of demographic models (*Wilson et al.* 2005; *Henry-Silva et al.* 2008) and drifting rafts are the connection between the local and regional scales. The phases of geographic spread are illustrated in Figures 2.1 and 2.2.

At the regional scale, ecologists wish to characterize the spatial dynamics of a species distribution through dispersal models. Dispersal of invasive plant species is approached following two main methodologies: empirical or mechanistic (or sometimes a combination of the two) (*Higgins and Richardson* 1996; *Jongejans et al.* 2008). Empirical models use historical data records and probability density functions to describe dispersal distances, while mechanistic models use knowledge of ecological

Figure 2.2: Photograph of *E. crassipes* in Ihema Lake, Rwanda, demonstrating all three phases of geographic spread illustrated in Figure 2.1. Photograph taken by the author.

processes and species-environment interactions to describe observed patterns (*Higgins et al.* 1996). Empirical models are useful when dispersal mechanisms are poorly understood, but they are underpinned by empirically-derived constants and thus cannot lead to a predictive understanding of dispersal (*Higgins and Richardson* 1996; *Nathan and Muller-Landau* 2000). Mechanistic models are warranted for species that are strongly affected by spatially-varying and temporally-varying environmental factors (*Jongejans et al.* 2008), and offer potential to predict dispersal across a spectrum of conditions and facilitate generalization to unstudied sites and species (*Nathan and Muller-Landau* 2000). Despite these inherent advantages, mechanistic models remain challenging to develop or otherwise unavailable in many cases and so are not frequently employed; existing mechanistic models of plant dispersal primarily consider airborne transport of seeds from terrestrial plants (*Greene and Johnson* 1989; *Schurr et al.* 2005). For the case of free-floating macrophytes, whose primary dispersal mechanisms are reasonably understood and are tightly coupled to environmental flows (*Gay* 1960), a mechanistic model would greatly improve our understanding of the spatial dynamics—a prerequisite for developing effective management strategies (*Jongejans et al.* 2008).

2.1.2 Transport Model Development

To develop a mechanistic and predictive approach to free-floating macrophyte dispersal, let us first consider the force balance describing the acceleration of a free-floating macrophyte raft. The raft experiences flow-induced drag forces on its above- and below-water structures (herein called leaf and root canopies, respectively). Additionally, there is an inertial force caused by the raft accelerating through the water. A free-floating macrophyte raft is assumed to drift under the influence of water drag F_w, air drag F_a, and the inertial force F_I

$$m_v \frac{du_v}{dt} = F_w + F_a + F_I, \tag{2.1}$$

where m_v and u_v are the raft mass and velocity, respectively. Coriolis forcing, water surface slope, and wave radiation are assumed negligibly small. Following classic drag theory (*Batchelor* 2000), each drag force is parameterized by use of a drag coefficient (C_D^i) defined in terms of flow velocity relative to the raft:

$$F_w = \frac{1}{2}\rho_w C_D^w A_v^w \mid u_w - u_v \mid (u_w - u_v) \tag{2.2}$$

$$F_a = \frac{1}{2}\rho_a C_D^a A_v^a \mid u_a - u_v \mid (u_a - u_v)\,, \tag{2.3}$$

where ρ is the fluid density, subscripts w and a denote water and air, respectively, A_v is the area of the vegetation canopy in each fluid, u_w is the depth-averaged water velocity, u_a is the wind velocity at a reference height, and u_v is the velocity of the vegetation raft. Again using the reference frame of the raft, the inertial force is defined from (*Denny* 1988):

$$F_I = \rho_w V C_m a, \tag{2.4}$$

where V is the volume of the submerged root canopy, C_m is the inertia coefficient, and a is the acceleration of the water relative to the raft, $\frac{d}{dt}(u_w - u_v)$. It is assumed that the inertial force in air is negligible. Substituting Equations (2.2)–(2.4) into (2.1) gives

$$\begin{aligned}\frac{du_v}{dt}\left(\rho_w V C_m + m_v\right) &= \frac{1}{2}\rho_w C_D^w A_v^w \mid u_w - u_v \mid (u_w - u_v) \\ &\quad + \frac{1}{2}\rho_a C_D^a A_v^a \mid u_a - u_v \mid (u_a - u_v) \\ &\quad + \rho_w V C_m \frac{du_w}{dt}\end{aligned} \tag{2.5}$$

Equation (2.5) provides a complete description of the acceleration and resulting unsteady raft velocity u_v. In this work, it is expected that accelerations are small in magnitude and duration, and from an ecological standpoint, longer time scales are most relevant to dispersal; thus the inertial force is not explicitly resolved. For the steady-state solution of Equation (2.5), in which water forcing balances air forcing, u_v will reach a constant value and (2.5) becomes

$$0 = \rho_w C_D^w A_v^w \mid u_w - u_v \mid (u_w - u_v) + \rho_a C_D^a A_v^a \mid u_a - u_v \mid (u_a - u_v) \tag{2.6}$$

This model is illustrated in Figure 2.3. To implement this model for a set of given field conditions, estimates of the drag coefficients (C_D^w, C_D^a) are required. Laboratory experiments were conducted to determine these drag coefficients under steady wind and water currents. The mechanistic model proposed here is based on other studies of floating body transport, as discussed in Chapter 1.2: macroalgae (*Bell and Hall* 1997; *Biber* 2007), marine invertebrates (*Iosilevskii and Weihs* 2009), volcanic pumice (*Bryan et al.* 2004), and icebergs (*Smith* 1993).

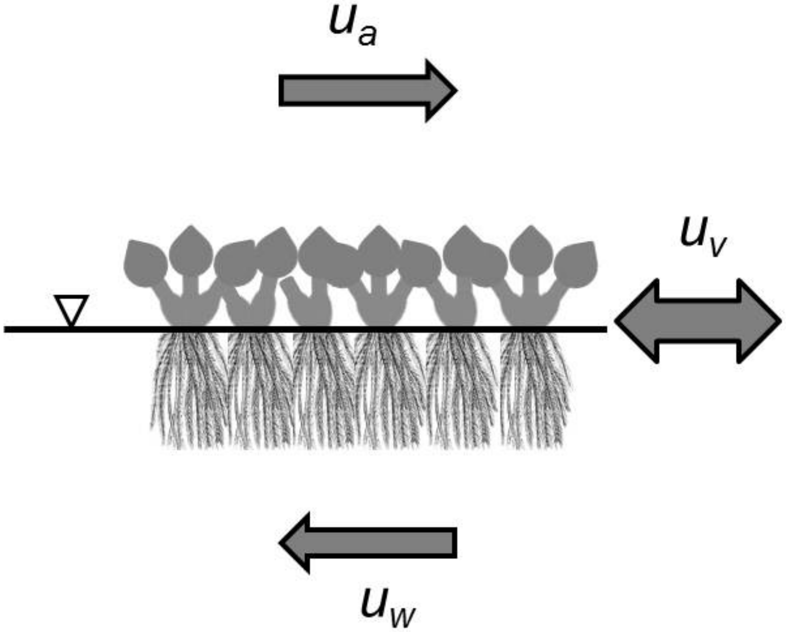

Figure 2.3: Schematic of free-floating macrophyte transport model from Equation (2.6) and definition of velocity variables: wind velocity at a reference height (u_a), depth-averaged water velocity (u_w), and resulting vegetation raft velocity (u_v).

2.2 Materials and Methods

2.2.1 Vegetation

This research was conducted using live *E. crassipes*, also known as common water hyacinth, a tropical macrophyte originating in Brazil. The relevant morphology of *E. crassipes* includes the *leaf*, consisting of a single glossy blade (lamina) attached to a *petiole* originating from the rhizome; the *stolon*, an elongate structure of similar material to the petiole that produces a ramet (asexually-produced plant) at its distal end; and the *root*, having a fibrous and unbranched central axis originating from the rhizome, with numerous feathery, densely-spaced laterals along the length (Figures 2.4-2.5) (*Center and Spencer* 1981; *Gopal* 1987). A bluish purple flower (inflorescence) is produced on single spikes to 60 cm in length. Stems vary in height from a few centimeters to over a meter, and roots range in length from 10 cm to over 50 cm (*Penfound and Earle* 1948). The petiole develops a spongy, bulbous swelling mid-length in young plants growing along the edge of the mat nearest to open water which provides additional buoyancy. The root system of *E. crassipes* is usually suspended in water but may become rooted if stranded in moist soil or in shallow water (*Center and Spencer* 1981).

E. crassipes individuals were obtained via mail order through a pond supply store (Pondplants, Escondido, CA, USA) and grown indoors in 10-gallon aquariums filled with freshwater placed under a 1000 W grow light (Xtrasun by Hydrofarm, Inc., Petaluma, CA, USA) for 12 hours day^{-1}. Plants were supplemented with fertilizer (Miracle-Gro, The Scotts Company LLC, 24-8-16 nutrient ratio). The plants used in this experiment ranged in age from 2–6 months; all plants were small to medium in size (*Penfound and Earle* 1948) and were not flowering during data collection.

To simulate *E. crassipes* dispersal, small rafts of vegetation were constructed in the laboratory using braided spectra fiber line (PowerPro, $< 3\%$ elongation) tied around the perimeter of the raft to maintain plant orientation and density. The line was tied loosely such that raft dimensions were allowed to expand and contract as flow velocity changed; I observed minimal length contraction (1-2 cm) for root canopies at the three highest water velocities. Rafts were constructed with densities of 400–550 leaves m^{-2} (corresponding to 8.8–12.1 kg m^{-2} biomass density) (Table 2.1) representative of seasonal conditions that give rise to floating raft dispersal (*Boyd and Scarsbrook* 1975; *Center and Spencer* 1981). Little is known of the size and number of plants in naturally-occurring *E. crassipes* rafts; qualitative descriptions of rafts range from a single plant (*Bock* 1969) to massive rafts two kilometers in diameter comprising hundreds of plants (*Masifwa et al.* 2001). Because it reproduces asexually, the minimum requirement for successful dispersal of *E. crassipes* is a single, viable plant.

Experiments were conducted to measure water drag and air drag separately. In a flume, water drag was measured on the *root canopy*, consisting of submerged structures: rhizomes and root strands. In a wind tunnel, air drag was measured on the *leaf canopy*, consisting of above-water structures: petioles, leaves, and stolons. In both facilities, rafts were held stationary relative to the flow at a fixed location along the flume/wind tunnel by the spectra line. From the upstream end of each raft, spectra line was extended 0.3 m upstream along the centerline of both the raft and the flume/wind tunnel and attached to a force transducer. Dimensions for root (water forcing) and leaf (air forcing) canopies of experimental rafts are presented in Table 2.1.

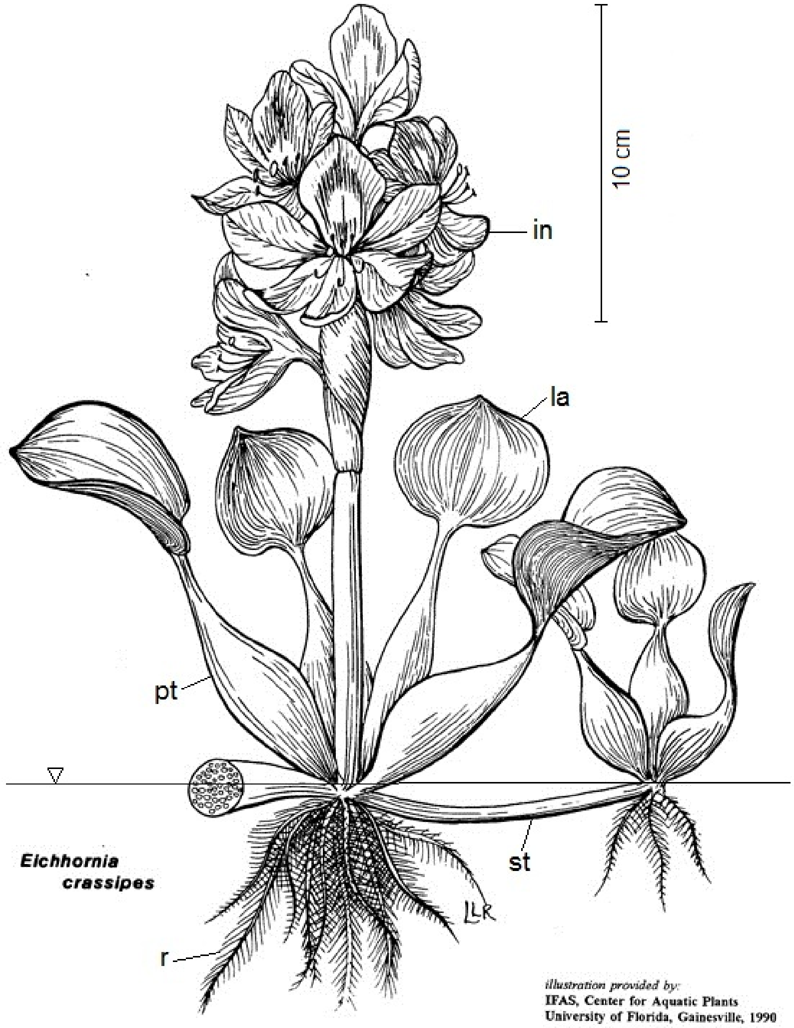

illustration provided by:
IFAS, Center for Aquatic Plants
University of Florida, Gainesville, 1990

Figure 2.4: Vegetative structures of *E. crassipes*: in - inflorescence; la - lamina; pt - petiole; r - root; st - stolon. Mature plant (left) shown with asexually-produced ramet (right). Adapted from *CAIP* (1990). Used with permission.

Figure 2.5: Photograph of *E. crassipes* individuals, showing laminae, petioles, roots, and stolons (see Figure 2.4). Mature plant (left) shown with asexually-produced ramet (right). Scale on right is 30.5 cm.

Table 2.1: Canopy dimensions and leaf density for rafts used in measuring water drag on root (W) and air drag on leaf (A) canopies.

Canopy	Length, L (cm)	Width, b (cm)	Height, h_c (cm)	Leaf Density (total m^{-2})
W1	35	30	10	550
W2	35	30	30	550
W3	55	30	10	540
W4	55	30	30	540
W5	50	55	10	505
W6	60	60	15	400
W7	70	55	14	430
A1	70	62	9	505
A2	100	70	12	537

2.2.2 Experimental Apparatus

Flume

Water drag measurements were obtained in a recirculating laboratory flume of dimensions 20 m length, 0.6 m width, and 0.3 m depth (H_w). The flume was set to a bed slope of 0° and unidirectional flow was created by a variable-drive impeller pump located at the downstream end of the flume. The pump was mounted vertically on a 2.54 cm diameter shaft that forced water downwards through a 45 cm diameter return pipe mounted under the flume body to the opposite end. Water re-entered the flume vertically through the floor of the flume. To condition the turbulence and minimize secondary circulation, three sets of grid containing 1 cm wide square openings were placed at the upstream end of the flume, downstream of the entering water. Surface waves at the inlet were damped by a wooden plank mounted long-edge perpendicular to the flow, extending into the water to 2 cm depth and spanning the entire flume width. For all experiments, water depth was 0.3 m and current velocity over the test section (2 m long and 10 m downstream from the entrance) varied from 0.02 to 0.16 m s^{-1}. Upon completion of the measurement of water velocity and force on the canopy at each increment, the velocity in the flume was increased and allowed to equilibrate for 10 min prior to subsequent measurements.

Wind Tunnel

Air drag measurements were collected in a non-recirculating wind tunnel of dimensions of 4 m length, 0.8 m width, and 0.53 m height (H_a) and an attached basin filled with freshwater to a depth of 0.47 m. This setup allowed the buoyant plants to float and experience wind-induced drag naturally. Unidirectional flow was created by an outward-facing fan (Reynor, USA) located at the downstream exit controlled by a variable autotransformer (Variac). Wind velocity over the test section (2.5 m from the entrance) varied from 0.4 to 1.8 m s^{-1}. Upon completion of the measurement of wind speed and force on the canopy at each increment, the velocity in the tunnel was increased and allowed to equilibrate for 5 min prior to subsequent measurements.

2.2.3 Velocity Measurements

Approach velocities in water and air were measured using an acoustic Doppler velocimeter (ADV) (Vectrino, NortekUSA, Annapolis, MD, USA) and a sonic anemometer (CSAT, Campbell Scientific, Inc., Logan, UT, USA), respectively. The ADV was mounted to a wheeled cart above the flume, and the anemometer was mounted to an aluminum rod projecting from the ceiling of the wind tunnel. In the flume, the sampling volume of the ADV was aligned with the flume centerline; in the wind tunnel, the sampling volume of the CSAT was 7.5 cm to the right (looking downwind) of the wind tunnel centerline. In water, the approach velocity was sampled using the ADV at 25 Hz for 5 min at a depth 0.07 m below the water surface ($z/H_w = 0.77$), outside the bottom boundary layer and approximately at the mid-height of the root canopy (total canopy height 0.1-0.15 m). In air, the approach velocity was sampled using the anemometer at 30 Hz for 5 min at the mid-height of the air space above the water basin ($z = 22.5$ cm, $z/H_a = 0.5$), outside both the air-water and ceiling boundary layers.

To determine whether wind-induced surface water currents affected the measured air drag force, near-surface water velocity was measured in the wind tunnel using an acoustic Doppler velocimeter (ADV) (Vectrino, NortekUSA, Annapolis, MD, USA). The ADV was deployed in side-looking mode, mounted to a stand inside the wind tunnel; the sampling volume was located 2.27 m from the upstream end at a depth of 4.3 cm below water surface and 5 cm left of the CSAT sampling volume (looking downwind).

2.2.4 Drag Measurements

Water- and air-drag forces were measured on the bulk canopy using a force transducer composed of an electrical-resistance foil strain gauge bonded on one side of a 13 × 60 × 0.075 mm force beam made of stainless steel shimstock. The force transducer was mounted 2 cm above the water surfaces by a fixed metal rod spanning the width of the flume and wind tunnel. Vegetation rafts were attached to the beam directly by spectra line; force was measured using a strain indicator (P-3500, Vishay Measurements Group, Raleigh, NC, USA) using a half-bridge configuration. Output voltages were recorded for 5 min at each approach velocity using a data acquisition system (miniLAB 1008, Measurement Computing Corporation, Norton, MA, USA) and the Data Acquisition Toolbox in Matlab at an acquisition rate of 100 Hz. To calibrate the force transducer, the force beam was loaded in the same direction as during experiments; weights ranging from 0.01 to 1.3 N ($n = 9$) were applied two times for two minutes each. The mean voltage recorded for each weight was linearly regressed ($R^2 = 0.99$); the standard error of repeated measurement of any force was less than 5%. Schematics of the experimental setup are shown in Figure 2.6A for water and Figure 2.6B for air.

2.2.5 Data Analysis

From each canopy experiment, force-velocity data were used to calculate water and air drag coefficients (C_D^w, C_D^a) using the quadratic drag law:

$$C_D^i = \frac{2F_i}{\rho_i A_i U_i^2}, \tag{2.7}$$

where i denotes water (w) or air (a) values, F is the measured drag force (time-averaged), U is the measured approach velocity (time-averaged), ρ is density of the ambient flow at experimental conditions, and A is the maximum frontal area of canopy facing the flow (measured at zero velocity). In the flume, a ruler was used to measure maximum root canopy width; canopy depth was measured at 10 points along the width at a location midway along the length of each raft. Frontal area was calculated as the area of the polygon created by the above measurements. In the wind tunnel, A was estimated using still-frame digital images taken with a digital camera placed $\sim$ 2.5 m upwind of the plant along the centerline of the wind tunnel. A floating block of known dimensions was placed beside the plants to provide a reference scale for leaf canopy dimensions in the images. Images were analyzed using ImageJ software (Version 1.43) by outlining the leaf canopy in each image, forming a polygon shape from which frontal area was calculated.

Studies of vegetation canopies typically find deviations from the quadratic drag law such that the drag coefficient decreases as velocity increases; this is caused by flexibility and reconfiguration of canopy elements in faster flows and results in decreasing relative drag force for increasing flow velocity (*Vogel* 1984; *Ennos* 1999; *Sand-Jensen* 2003). To establish the empirical relationship between drag and flow velocity, the power law relation was used:

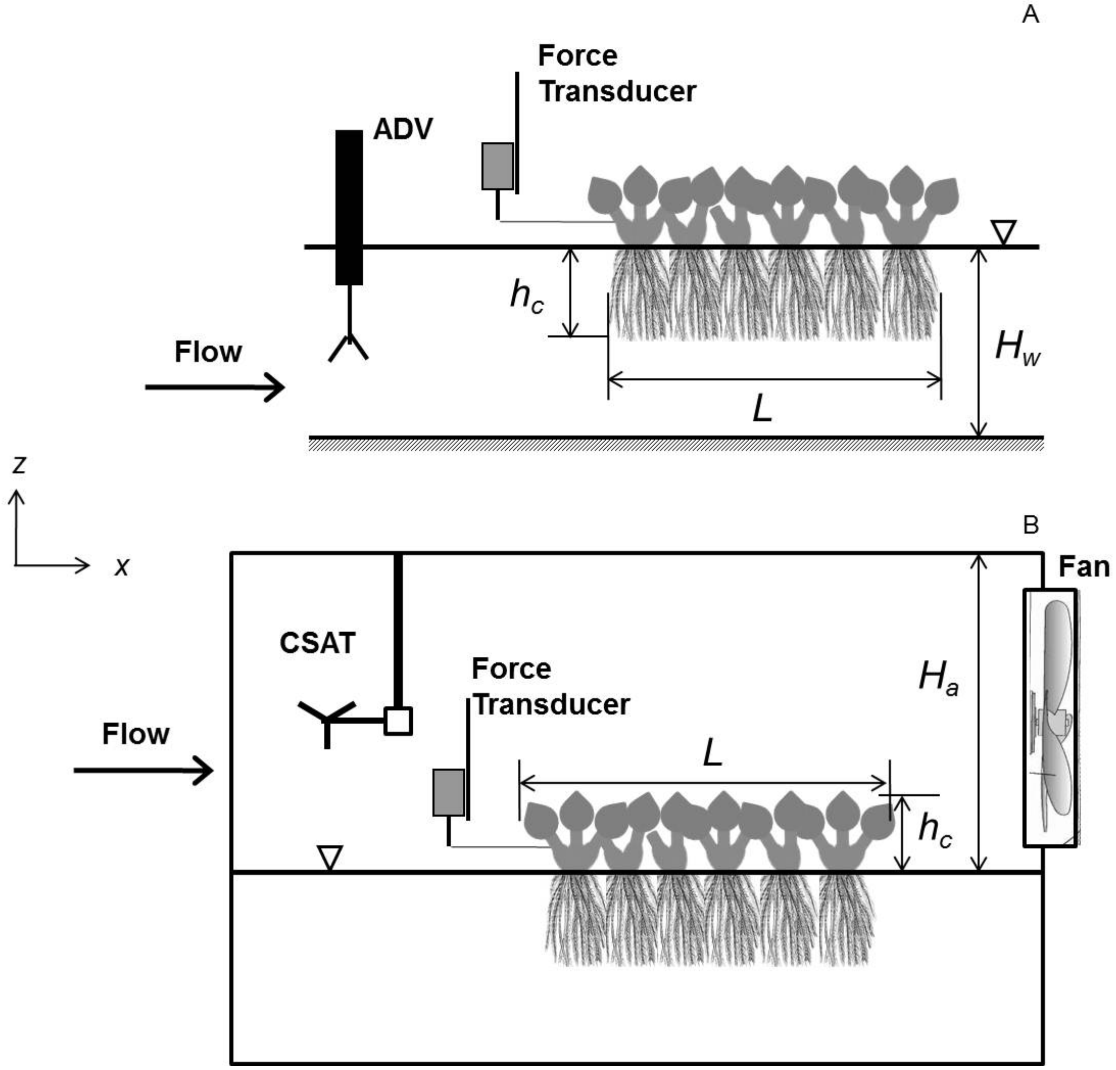

Figure 2.6: Schematics of experimental setup for drag measurements on vegetation rafts. (A) Water drag experiments were conducted in a recirculating flume of water depth H_w. (B) Air drag experiments were conducted in a semi-enclosed wind tunnel with attached water basin. Air flow (depth H_a) was induced by an outward-blowing fan mounted at the downstream end. In both fluids, drag on stationary floating vegetation rafts was measured using a force transducer. Raft dimensions (length L and root canopy height h_c) were measured for the canopy immersed in fluid of interest. Upstream flow velocity was measured using an acoustic Doppler velocimeter (ADV) in water and by a sonic anemometer (CSAT) in air. Water surface is denoted by ∇. Not to scale.

$$F_i = kU_i^{\gamma}, \tag{2.8}$$

where i denotes water (w) or air (a) values, F is the time-averaged drag force (N), U is the time-averaged approach velocity (m s^{-1}), and k and γ are parameters estimated from nonlinear least squares regression analysis of the force–velocity relationship.

For each canopy, a raft Reynolds number (Re_b) was defined:

$$Re_b = Ub/\nu, \tag{2.9}$$

where U is the time-averaged approach velocity in water or air (m s^{-1}), b is a characteristic length taken to be width of raft canopy facing the corresponding flow (note that for a given raft, canopy widths for water and air are not necessarily equal) (m), and ν is the kinematic viscosity of the fluid in which drag is measured (m^2 s^{-1}). Reynolds number represents the relative importance of inertia to viscosity for a particular flow situation and allows scaled comparisons of flow conditions between each fluid.

To compare general relationships of force and Reynolds number for water and air, additional power law relations were developed for composite data sets of root canopies (W1–W7, Table 2.1) and leaf canopies (A1–A2):

$$F = mRe_b^{\beta}, \tag{2.10}$$

where m and β are estimated from nonlinear least squares regression of F (in N) vs. Re_b.

To determine if the relation between C_D and Re_b for each experimental raft was significant (i.e., to test whether C_D is a significant function of Re_b), linear regression was performed to fit a relation of the form $C_D = p_1 Re_b + p_2$. If the 95% confidence interval for p_1 contained zero, C_D was not considered a statistically significant function of Re_b.

To compare relative forcing of water- and air-drag for a given raft, drag on one particular raft was measured in both the flume (Canopy W5) and the wind tunnel (Canopy A1). To compare the effect of root canopy depth (h_c) and length (L) on F_w, C_D^w, and γ, four rafts of constant width ($b = 30$ cm) were constructed of two different L and h_c combinations ($L = 35, 55$ cm; $h_c = 10, 30$ cm, W1–W4 in Table 2.1). Canopy depth was varied by trimming roots to uniform height. Values of C_D^w for varying root canopy aspect ratio ($L : h_c$) were compared for three values of Re_b (within 25% of target Re_b) to assess the effect of canopy aspect ratio on water drag coefficients.

2.2.6 Plant Material Characteristics

Modulus of elasticity (E), second moment of area (I), and flexural rigidity (EI) were determined for three vegetative structures of *E. crassipes*: roots, petioles, and stolons (described above). Specimens were taken from six individual plants from the same clonal population. The purpose of this testing was to determine structural properties of leaf and root canopies that further explain observed responses to air and water flows. Modulus of elasticity (E) is a mechanical property that indicates the stiffness (resistance to deformation) of a material. Second moment of area or moment of inertia (I) is a structural property that describes the distribution of material about an axis of a structure. The product of these two terms is the flexural rigidity (EI), which describes a structure's resistance to bending.

Testing was conducted using a materials testing machine (Model 1122, Instron Corp., Norwood, MA, USA). Length and diameter of all specimens was measured to the nearest 0.01 mm using calipers. For roots, E was determined by conducting tensile stress-extension tests on root segments ($n = 8$). During testing, each specimen was loaded in axial tension at a constant rate (0.1 mm s^{-1}) until failure; force (to nearest 0.01 mN) and extension (to nearest 1 μm) were recorded at 100 Hz. Stress (σ) was computed by dividing the measured force by the cross-sectional area of the specimen at the site of fracture. Root specimens were roughly circular in cross-section; area was defined as for a circle. Strain (ϵ) was determined by dividing the total extension by the original length of the root segment subjected to loading. For each specimen, E was determined from the slope of the linear region of σ–ϵ curves (*Hibbeler* 2000). The moment of inertia (I) was defined as for a circular cross-section:

$$I = \frac{1}{4}\pi\left(\frac{d}{2}\right)^4, \tag{2.11}$$

where d is the diameter of the specimen as described above.

For petioles and stolons, cantilever beam deflection tests were conducted on whole petioles (leaf removed, $n = 22$) and stolon segments ($n = 21$). Specimens were mounted horizontally by clamping the larger diameter end to a fixture attached to the testing machine base. Within 1 cm of the free end, the specimen was loaded by moving the force transducer head downward at a constant rate (0.5 mm s^{-1}) through a fixed distance (10 mm); force (to nearest 0.01 mN) and deflection (to nearest 1 μm) experienced by the specimen were recorded at 10 Hz. The EI for each specimen was computed using the relationship between force (F), deflection (w), and beam length (L) for cantilever beam loading:

$$EI = \frac{F}{w}\frac{L^3}{3}, \tag{2.12}$$

where the bending stiffness (F/w) was determined from the gradient of the linear range of the force–deflection curve (*Hibbeler* 2000). The cross-sections of petiole and stolon specimens were elliptical in shape, therefore moment of inertia was calculated as for a solid ellipse:

$$I = \frac{1}{4}\pi a b^3, \tag{2.13}$$

where a and b are the long and short radii of the specimen, respectively. One-way ANOVA and Tukey post-hoc tests were used to compare material properties of the vegetative structures. All analyses were conducted using Matlab software.

2.3 Results

2.3.1 Drag Forces and Coefficients

The root and leaf canopies exhibited very different responses to corresponding water and air forcing. While both water and air drag forces increased as Re_b increases, water drag on the root canopies was much higher than air drag on the leaf canopies over the same decade of Re_b (Figure 2.7). The same force data are plotted against approach velocity (U_i) for water and air separately in Figure 2.8; here the differences between air and water drag are also evident, as water drag forces were one order of magnitude higher than air drag forces although U_w were an order of magnitude *lower* than U_a. For the same raft (W5 & A1, Figure 2.7), water drag on the root canopy was much greater than air drag on the leaf canopy, over the same Re_b regime (range 1–9×10^4).

The water drag coefficients (C_D^w) were statistically significant functions of Re_b, with higher values of C_D^w at lower Re_b decreasing to smaller values at higher Re_b (Figure 2.9). This indicates the root canopy reconfigured as water velocity increased. For the leaf canopies, C_D^a was not a statistically significant function of Re_b, i.e., the best-fit slopes from linear regression had 95% confidence intervals that contained zero. For the same raft (W5 & A1) and same decade of Re_b, C_D^w was greater than C_D^a. The value of C_D^w decreased as Re_b increases; the ratio of C_D^w (W5) to C_D^a (A1) decreased from 2 at $Re_b \sim 2.5 \times 10^4$ to nearly 1 at $Re_b \sim 7.5 \times 10^4$ (Figure 2.9).

The near-surface water velocity induced by air flow over the water in the wind tunnel had a magnitude of 0.6 ± 0.1 cm s^{-1}; this was determined to be an insignificant contribution to the measured air drag force.

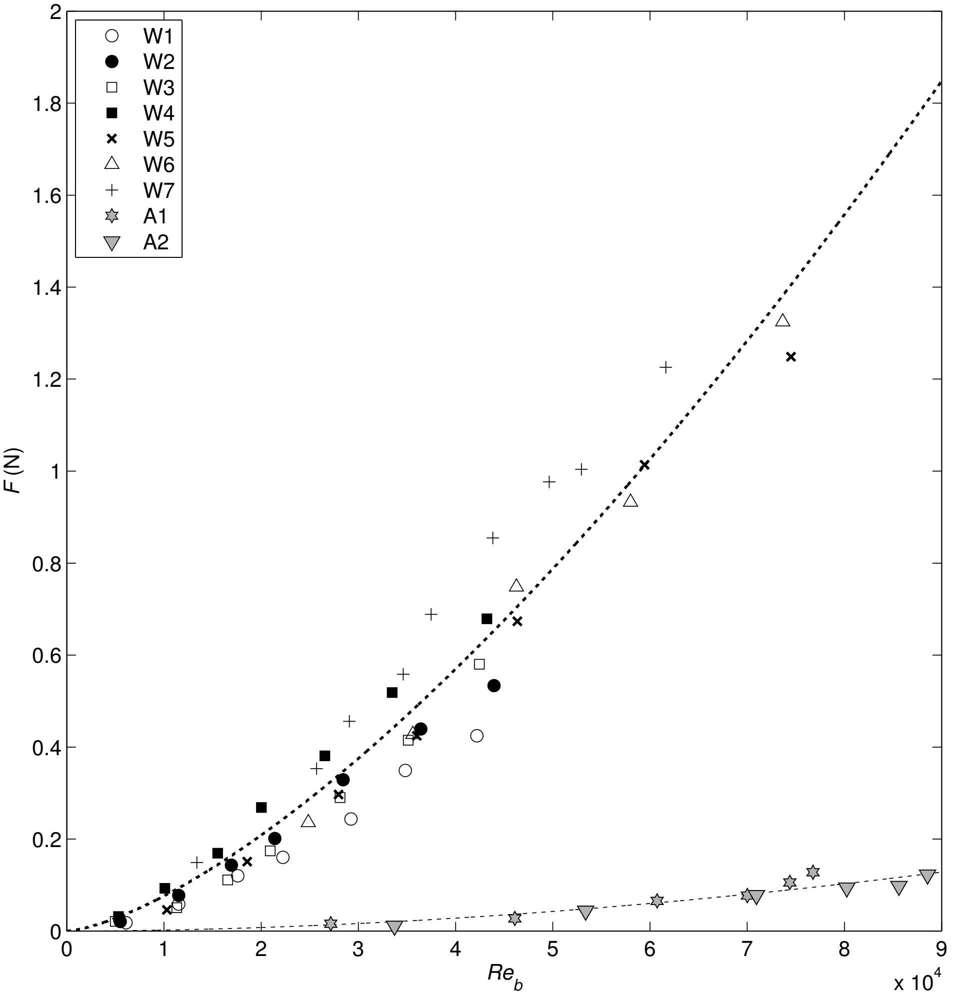

Figure 2.7: Measured drag force (F) vs Reynolds number (Re_b) for root and leaf canopies (denoted by W and A, respectively). Dashed lines represent power law fitting of the form $F = mRe_b^\beta$ for all root canopies (heavy dashed line; $m = 1.20 \times 10^{-7}$; $\beta = 1.45$; $R^2 = 0.942$), and both leaf canopies (light dashed line; $m = 7.57 \times 10^{-13}$; $\beta = 2.28$; $R^2 = 0.905$).

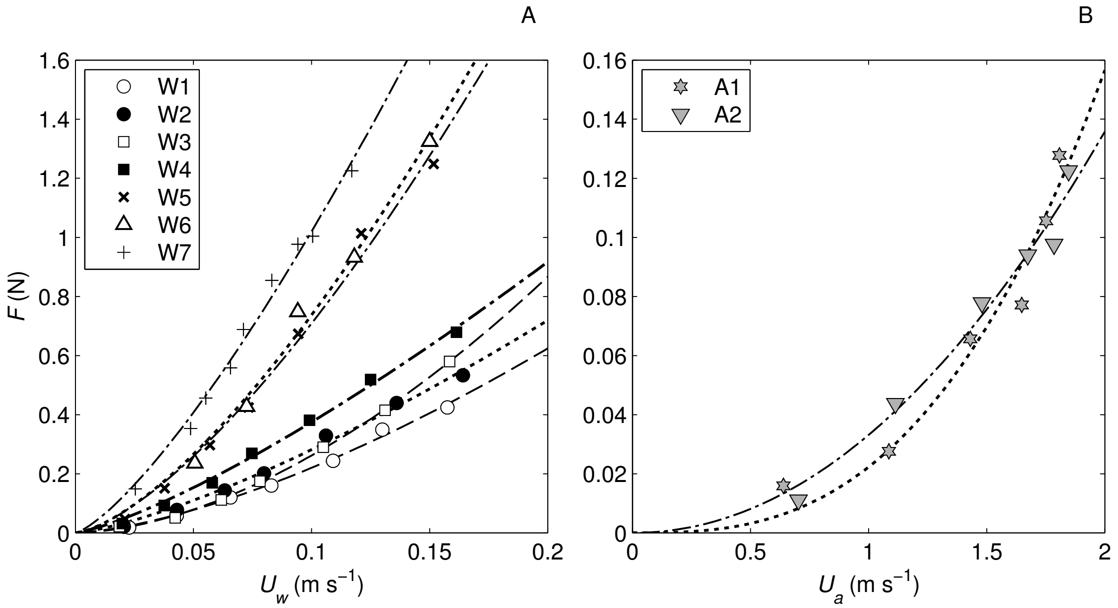

Figure 2.8: Drag force as a function of approach velocity for (A) water (U_w) and (B) air (U_a). Lines shown are results of nonlinear least squares regression analysis (Table 2.2). Note the axes have different scales.

2.3.2 Power Law Relations

Laboratory measurements indicated strong relationships between drag forces (N) and approach velocities (m s^{-1}) on root and leaf canopies; these relationships were well-explained by the power law relation of Equation (2.8). In the experimental data, the velocity exponent γ in (2.8) varied from 1.3–1.7 for the root canopy ($n = 7$) and from 2.0–2.8 for the leaf canopy ($n = 2$) (Table 2.2). These power law fits are plotted with corresponding experimental data in Figure 2.8 for water and air separately. The 95% confidence intervals on γ in root canopies ranged from 1.1–1.8 whereas in leaf canopies they ranged from 1.3–4.3 (Table 2.2).

In the aggregated root and leaf canopy data sets, water and air drag forces were well-described by the power function of Re_b in Equation (2.10); β=1.45 for root canopies and 2.28 for air canopies (Figure 2.7). Comparing each value of β to the corresponding range of γ values, β falls within the range of γ values for both water and air.

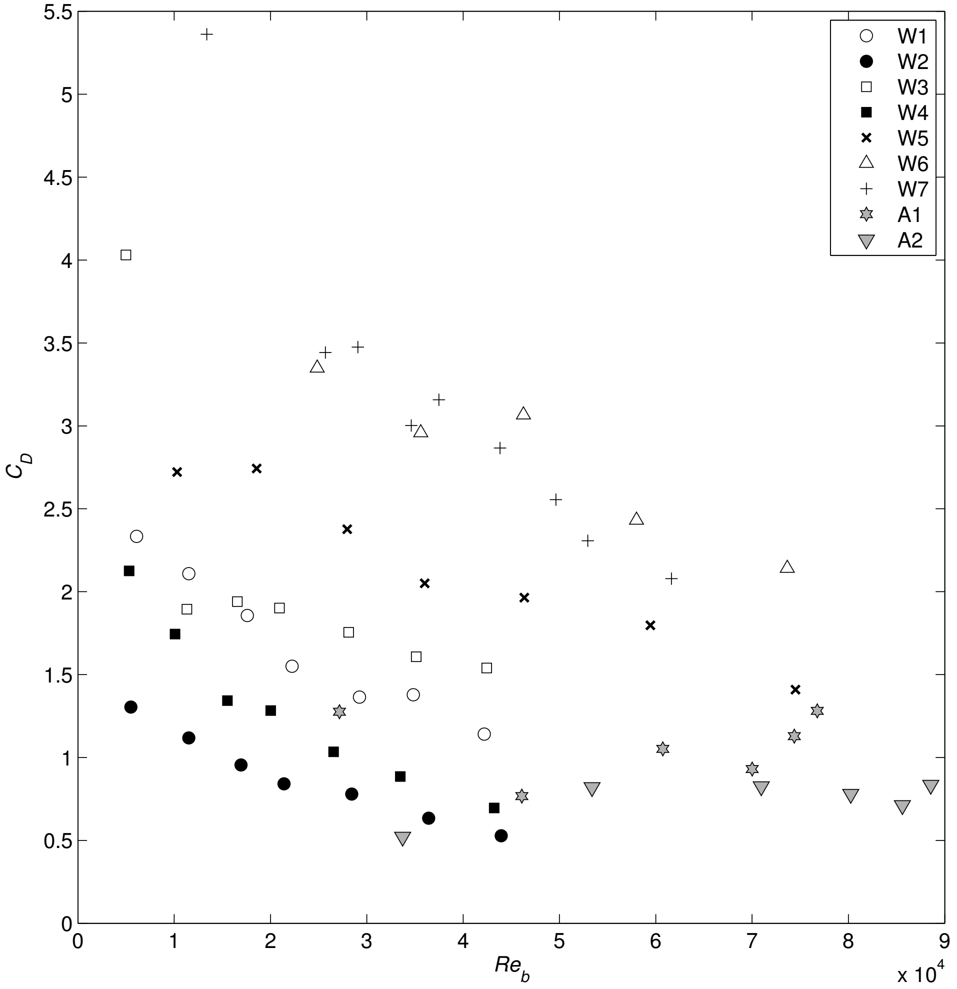

Figure 2.9: Drag coefficients (C_D) vs Reynolds number (Re_b) for root and leaf canopies (denoted by W and A, respectively).

Table 2.2: Best-fit parameters (k, γ) and goodness-of-fit (R^2) for power law fitting of force (F, in N) vs. velocity (U, in m s^{-1}), $F = kU^\gamma$, in root (W) and leaf (A) canopies. Values in parentheses are 95% confidence intervals for γ.

Canopy	k	γ	R^2
W1	7.037	1.505 (1.31, 1.70)	0.994
W2	6.371	1.355 (1.17, 1.54)	0.994
W3	13.990	1.728 (1.65, 1.81)	0.999
W4	7.324	1.291 (1.15, 1.43)	0.995
W5	20.040	1.451 (1.22, 1.68)	0.991
W6	21.710	1.469 (1.12, 1.82)	0.989
W7	21.520	1.324 (1.17, 1.48)	0.990
A1	0.0223	2.812 (1.37, 4.25)	0.957
A2	0.0331	2.035 (1.30, 2.77)	0.975

2.3.3 Effect of Canopy Dimensions

Water

Comparing canopies W1 ($b \times h_c \times L$: $30 \times 10 \times 35$ cm) to W3 ($30 \times 10 \times 55$ cm) and W2 ($30 \times 30 \times 35$ cm) to W4 ($30 \times 30 \times 55$ cm), water drag increased as L increased for constant b and h_c at constant plant density (Figure 2.8A); C_D^w also increased as L increased (Figure 2.9). However, these results were not statistically significant at the 0.05-level using a paired t-test.

As h_c increased for constant b and L (i.e. decreasing $L : h_c$ ratio), as in canopy pairs W1–W2 and W3–W4, drag force increased (Figure 2.8A) and C_D^w decreased (Figures 2.9 & 2.10); both of these effects were statistically significant (paired t-tests; F_w: W1–W2, $t = -3.38$, $df = 6$, $p = 0.015$; W3–W4, $t = -5.35$, $df = 6$, $p = 0.002$; C_D^w: W1–W2, $t = 11.7$, $df = 6$, $p = 2.2 \times 10^{-5}$; W3–W4, $t = 3.91$, $df = 6$, $p = 0.008$). Additionally, increasing h_c was correlated with decreases in the exponent on velocity in the power law relation, γ (Table 2.2).

Comparing canopies W3 to W5 ($55 \times 10 \times 50$ cm), as b increased for constant h_c and similar L, both drag force and C_D^w increased (Figures 2.8A & 2.9). These results were not statistically significant at the 0.05-level.

Finally, in the root canopy, C_D^w generally increased as canopy aspect ratio ($L : h_c$) increased for three (approximately) constant values of Re_b (Figure 2.10). As Re_b increased, C_D^w decreased for the same $L : h_c$ ratio.

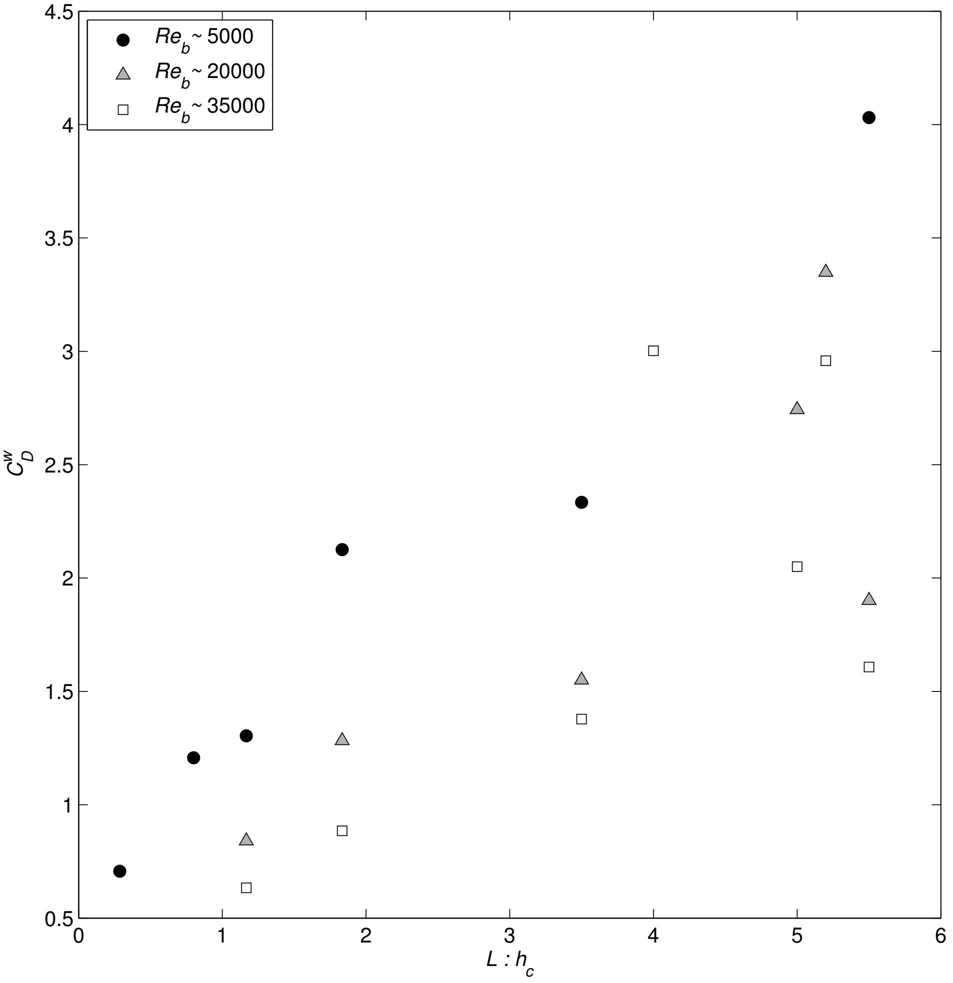

Figure 2.10: Water drag coefficients (C_D^w) for varying root canopy aspect ratios of length (L) to height (h_c). Values of C_D^w were extracted at target Re_b values of $5.0 \times 10^3 \pm 1.3 \times 10^3$ (circles); $2 \times 10^4 \pm 0.5 \times 10^4$ (triangles); and $3.5 \times 10^4 \pm 0.88 \times 10^4$ (squares). Actual values of Re_b ranged from 4600–6100 (5300 ± 500, mean±s.d.) 18,600–24,800 ($21,300 \pm 2100$) and 33,500–36,400 ($35,200 \pm 1000$), respectively.

Table 2.3: Elastic modulus (E), second moment of area (I), and flexural rigidity (EI) for vegetative structures of *E. crassipes*. For each structure, first row reports mean ± s.d. from n samples; second row reports 95% confidence interval for the mean.

Structure	E (MN m^{-2})	I (m^4)	EI (N m^2)	n
Root	43.7 ± 20.4	$5.57 \times 10^{-14} \pm 4.10 \times 10^{-14}$	$2.39 \times 10^{-6} \pm 1.60 \times 10^{-6}$	8
	$(26.7, 60.7)$	$(2.14 \times 10^{-14}, 9.00 \times 10^{-14})$	$(1.05 \times 10^{-6}, 3.72 \times 10^{-6})$	
Petiole	14.5 ± 7.6	$1.71 \times 10^{-11} \pm 1.13 \times 10^{-11}$	$2.30 \times 10^{-4} \pm 1.45 \times 10^{-4}$	22
	$(11.1, 17.9)$	$(1.21 \times 10^{-11}, 2.21 \times 10^{-11})$	$(1.66 \times 10^{-4}, 2.95 \times 10^{-4})$	
Stolon	14.8 ± 5.4	$1.66 \times 10^{-11} \pm 0.76 \times 10^{-11}$	$2.49 \times 10^{-4} \pm 1.44 \times 10^{-4}$	21
	$(12.4, 17.3)$	$(1.32 \times 10^{-11}, 2.01 \times 10^{-11})$	$(1.83 \times 10^{-4}, 3.15 \times 10^{-4})$	

Air

In air, no increase in force was observed as canopy dimensions changed (Figure 2.8B). Additional leaf canopies of smaller dimensions were tested in this study, but recorded forces were below the detection limit of the force transducer (0.01 N). This observation further illustrates the lower magnitude of air drag compared to water drag.

2.3.4 Plant Material Characteristics

The elastic moduli (E) of three structures (roots, petioles, and stolons) were of similar magnitude (Table 2.3), but petioles and stolons had significantly lower E than roots (ANOVA: $f = 29.1$; $df = 2, 48$; $p = 5.3 \times 10^{-9}$). The second moment of area (I) for root specimens was significantly smaller than that of petiole and stolon specimens (ANOVA: $f = 12.0$; $df = 2, 48$; $p = 6.0 \times 10^{-5}$). Values of flexural rigidity (EI) were similar for petioles and stolons but significantly lower for roots (ANOVA: $f = 10.7$; $df = 2, 48$; $p = 1.4 \times 10^{-4}$). Tukey post-hoc tests indicate none of E, I, and EI for petioles and stolons were different from one another. Complete results of materials testing are presented in Appendix A.

2.4 Discussion

2.4.1 Drag Forces and Coefficients

The results demonstrate the relative influence of air and water flows on free-floating *E. crassipes* rafts. The forces induced on test rafts in the laboratory increased as flow velocity increased for both air and water, as expected. Over the same decade of Re_b, water-induced drag was greater than air-induced drag (Figure 2.7). Water drag coefficients showed a strong, inverse dependence on Re_b, while air drag coefficients were invariant of Re_b (Figure 2.9). For a given raft subjected to a range of air and water velocities, water drag was greater than air drag over the same decade of Re_b; water drag coefficients were greater than air drag coefficients at low Re_b. At higher Re_b, however, C_D^w values approach that of C_D^a, suggesting that, for sufficiently high Re_b, the use of single drag coefficient for a raft may suffice. The greater water drag forces and coefficients highlight the large momentum exchange between water and *E. crassipes* roots, which has implications for ecological dispersal (described in Section 2.4.4).

Drag coefficients were defined using an estimate of maximal frontal area in Equation (2.7); area was assumed constant over the range of flow velocities encountered. Thus, variations in frontal area accompanying canopy reconfiguration at higher velocities appeared as changes in C_D. The choice of constant frontal area is useful for comparing the relationship between drag coefficients and Re_b for leaf and root canopies in this study. Varying definitions of characteristic area make comparisons of drag coefficient values across studies difficult; researchers typically choose one of the following characteristic areas: frontal area (area projected onto a plane perpendicular to the flow, as in this study), planform area (area projected onto a plane parallel to the flow), or total wetted surface area of canopy elements. Despite this hindrance, the form of the relationship between C_D and Re_b is similar to other studies of drag in vegetation (*Gillies et al.* 2002; *Sand-Jensen* 2003; *Molina-Aiz et al.* 2006; *Fonseca et al.* 2007). For three species of terrestrial plants, *Gillies et al.* (2002) found a weak dependence of C_D^a on Re, similar to the leaf canopy results in this study. Other studies found higher C_D values for vegetation canopies as compared to solid elements due to the higher porosity of vegetation causing increased momentum exchange (*Gaylord et al.* 1994; *Gillies et al.* 2000).

The general shapes of the drag coefficient curves for water and air in Figure 2.9 are further explained by comparing velocity exponents (γ) in the power law relation of Equation (2.8) for water and air. For all root canopies, γ was less than 2 (Table 2.2), indicating reconfiguration of individual root elements. Root reconfiguration plays a role in the relative reduction of drag at higher velocities and Reynolds numbers, leading to drag coefficients that are strong functions of velocity (and Re_b). Similar power law relations ($\gamma < 2$) have been shown for flexible leaf canopies in submerged macrophytes (e.g., *Vogel* 1984; *Usherwood et al.* 1997; *Sand-Jensen* 2003) and for individual blades of algae (*Gaylord et al.* 1994). In contrast, for leaf canopies, γ was not less than 2, meaning the leaf canopy does not reconfigure. Although γ from the nonlinear fitting of leaf canopy A1 was higher than 2 (Table 2.2), the goodness-of-fit was not appreciably greater than when γ is fixed at 2 ($R^2 = 0.96$ compared to

$R^2 = 0.94$ for $\gamma = 2$). Thus I expect the leaf canopies behave similar to a bluff body, for which frontal area does not change as flow velocity increases. In general, aquatic species have greater capacity for reconfiguration compared to terrestrial species; terrestrial species must support their own weight in air, while aquatic species benefit from greater buoyancy (*Ennos* 1999). Further explanation for this dissimilarity in the behavior of the root and leaf canopies using biomechanical properties follows in Section 2.4.2.

Considering the range of water velocities evaluated in this work, the results have broad applications because the relative water velocity ($U_{rel} = U_w - U_v$) experienced by a floating raft determines the water-induced drag force. Because the root canopy is efficient at extracting momentum from the water, minimal water velocities induce substantial drag and subsequent raft motion. The resulting equilibrium raft velocity will approach that of the ambient water (in the absence of strong winds), hence the relative water velocity is expected to be low.

This study included a limited amount of replication in drag measurements for each canopy geometry. However, I assume the raft response is constant for a particular canopy geometry and leaf density based on two observations. First, during preliminary experiment design and testing of canopies W1, W2, and A1, I did three replicates of the drag force measurements for different assemblages of plants. The mean force values of replicates showed limited variation; thus I determined the force was affected by canopy geometry rather than plant arrangement. Second, the standard deviation of each force measurement time series was low. Thus I expect the overall trends seen in these data will hold, including the primary result that water drag exceeds air drag for a given raft. Further research is needed to verify the drag force magnitudes and to obtain air drag force measurements for more leaf canopies.

2.4.2 Plant Biomechanics

In *E. crassipes,* root elements have significantly lower flexural rigidity (EI) than petioles and stolons (Table 2.3). The root canopy, composed of numerous root elements, is flexible and reconfigures as water velocity increases by deflecting into a streamlined shape. This allows for decreasing water drag coefficients as flow velocity increases (Figure 2.9). In contrast, the leaf canopy, made of less flexible petioles and stolons, does not reconfigure under increasing air velocity; thus the air drag coefficients vary little as flow velocity increases.

Further examination of properties of the three vegetative structures of *E. crassipes* shows that elastic moduli (E) are the same order of magnitude (10^7 N m^{-2}); this is similar in magnitude to species of submerged vegetation, including stipes of the macroalgae *Turbinaria ornata* (*Stewart* 2004) and stems of the seagrass *Zostera* *marina* (*Fonseca et al.* 2007). This suggests that *E. crassipes* roots, stolons, and petioles are made of similar material, and it is the shape of the structure, resulting in different values of I, that causes the variation in EI. *Bouma et al.* (2005) found similar relationships between E and I in two species of submerged vegetation. In a comparative study of aquatic and terrestrial species of buttercup (genus *Ranunculus*), *Usherwood et al.* (1997) found larger values of stem EI in terrestrial species than in aquatic species. The primary difference between previous studies and the current one is the presence of a single species at the interface of two different fluids; here I compare the rigidity of the stems in air to that of roots in water.

Studies of other forms of macrophytes (submerged and emergent) (e.g., *Alben et al.* 2002; *Bouma et al.* 2005; *Stewart* 2006) have shown that organisms having higher EI generally experience higher forces in unidirectional flow (for same fluid) because more flexible organisms (lower EI) deflect in higher flows to a streamlined shape. Here, although leaf canopy elements have higher EI than root canopy elements, forces exerted on the root canopy by water drag exceed those induced by air drag on the leaf canopy over similar Re_b.

Because stolons and petioles of *E. crassipes* have similar structural properties (Table 2.3), it does not appear that stolons are the primary weakness of a mat responsible for the formation of free-floating rafts, as has been suggested previously (*Bock* 1969).

2.4.3 Effect of Canopy Dimensions

For rafts of constant plant density (expressed as # leaves/planform area), water drag increased as root canopy dimensions (i.e. canopy volume) increased. Increasing canopy aspect ratio ($L : h_c$) was correlated with increasing C_D^w at constant Re_b (Figure 2.10). Physically, larger $L : h_c$ ratios represent longer canopy extent in streamwise direction at constant canopy height, or decreasing canopy height for a constant canopy length. The positive correlation between C_D^w and $L : h_c$ is indicative of increasing viscous drag, as demonstrated for solid objects by *Hoerner* (1965). Increasing viscous drag is expected because as raft size increases (at constant plant density), the root canopy increases in size, presenting more friction elements that extract momentum from the flow. For leaf canopies, the relationship between C_D^a and $L : h_c$ is unclear because of the limited range of canopy geometries. The $L : h_c$ values for both leaf canopies were nearly equal (A1: 7.7; A2: 8.3), and air drag was measured at only one common value of Re_b (7×10^4, Figure 2.10). The values of C_D^a for A1 and A2 are approximately equal at this Re_b, as expected given the equal $L : h_c$ ratio. Despite the lack of leaf canopy data, I expect a similar, positive relationship between C_D^a and $L : h_c$ caused by increasing viscous drag as canopy size increases.

In root canopies, as $L : h_c$ increased, γ increased, meaning less streamlining occurs. For the case of constant raft length L and decreasing root height h_c (e.g., comparing canopy pairs W2–W1 & W4–W3), each root element was shorter, resulting in less deflection and consequently less streamlining (higher γ). If instead h_c is held constant for increasing L, one would again expect less streamlining (higher γ) because of reduced drag on downstream root elements caused by the sheltering effect (*Raupach* 1992). Downstream root elements will experience lower velocities due to velocity reduction in the wake of upstream root elements and deflection of flow around the canopy, leading to a net decrease in root canopy streamlining.

To provide more insight into effects of canopy dimensions on C_D, a relation was developed from substitution of Equations (2.9) and (2.10) into (2.7):

$$C_D = \frac{2mU^{(\beta-2)}b^{(\beta-1)}}{\rho h_c \nu^{\beta}} \tag{2.14}$$

From Equation (2.14), one would expect that C_D is proportional to b for β greater than 1 and inversely proportional to h_c for both root and leaf canopies. This relation helps explain the increasing C_D^w for increasing b seen in comparison of root canopies W3 and W5. For root canopies, β was less than 2; after substitution into (2.14) one would expect C_D^w to be inversely proportional to U_w. In air, β is slightly greater than 2 and one would expect from (2.14) C_D^a to be invariant of U_a. These expectations are seen in the results; C_D^w decreased as Re_b increased, but C_D^a was relatively constant (Figure 2.9).

Comparison of Single Plant to Raft Assemblage

I observed a different flow interaction for individual plants than for raft assemblages. As part of the flume study, water drag on a single plant at two root lengths ($h_c = 10, 30$ cm) was measured. For the single plant having short roots, the exponent on velocity was highest of all root canopies ($\gamma = 2.054$, $R^2 = 0.992$), meaning streamlining was minimal and form drag was substantial. In contrast, the longer-root single plant had the lowest γ of all root canopies ($\gamma = 1.270$, $R^2 = 0.912$), indicating the greatest streamlining of all canopies in this study. The relationship between these values of γ is consistent with one of the above findings, that γ decreases for increasing h_c at constant L. However, the large value of γ for the short-root, single plant does not fit the general trend of decreasing γ for decreasing $L : h_c$ seen in the raft assemblages. This suggests the flow interaction for individual plants is different than for assemblages of plants. Individual plants consisting of few flexible structures may experience greater deflection and streamlining when the structures are sufficiently long; and when the structures are shorter, there is less streamlining and larger form drag. Based on the results of this experiment, I conclude that extrapolation from observations of individual plants to predict interactions for plant assemblages may not be appropriate. Further studies should be conducted on other macrophytes to compare the flow interaction of single plants to that of plant assemblages.

2.4.4 Implications for Ecological Dispersal and Management

Results of this study highlight the strong importance of water-induced forcing on *E. crassipes* and suggest water currents will be the primary driver of ecological dispersal. Minimal water velocities induce larger drag forces than those from considerable air velocities. As an example, for the same raft in water and air, water drag at $U_w \sim 0.025$ m s^{-1} exceeds air drag at $U_a \sim 2.0$ m s^{-1} (Figure 2.8). This value of U_a corresponds to a U_{10} (wind velocity at 10 m height) of 3.5 m s^{-1}, calculated assuming a logarithmic wind velocity profile having ordinary but arbitrary values of friction velocity u_* and roughness length z_0 of 0.15 m s^{-1} and 1 mm, respectively (for details, see *Stull* (1994)). Previous, qualitative descriptions of *E. crassipes* transport in the environment state wind as the primary forcing mechanism (*Penfound and Earle* 1948; *Gay* 1960; *Bock* 1969). The findings presented here contradict this hypothesis; I suggest instead that water currents are the primary transport agent, and wind forcing can only dominate when water velocity is minimal. This latter situation can occur in lake environments where water velocities are small, often less than 0.1 m s^{-1}, and water surface currents are generated by ambient winds. In contrast, for riverine and tidal systems, water velocities can exceed 1 m s^{-1}, inducing large drag forces on free-floating macrophytes. For tidal systems, air and water forcing are expected to alternately dominate depending on the tidal phase; at slack tides, water velocities are low and air drag can dominate transport given sufficient air velocity. Since such high forces are induced by water currents, I expect free-floating macrophytes like *E. crassipes* will tend to accumulate at a greater rate in hydrodynamically less-active environments such as embayments or coves.

I have not measured flow-induced forces for the higher flow velocities expected during storms or floods. As explained earlier, I believe the range of water velocities evaluated in the work are applicable to a broad range of environmental conditions, including flood events. To predict the drag forces induced during either a storm with high winds or a flood with strong water currents, one could extrapolate these experimental results. Extrapolating the wind tunnel data to a U_{10} of 20 m s^{-1}, I expect a raft with dimensions similar to Canopy A2 (Table 2.1) to experience an air drag force of 13 N. For the same raft, the relative water velocity required to induce a water drag force of the same magnitude is 0.4 m s^{-1} (based on extrapolation of flume data). However, at higher flow velocities, the leaf or root canopies may reconfigure such that the drag coefficients are lower than those used in this extrapolation. Thus these extrapolated force values should be taken as an upper bound. Observations of flow-induced forces at higher flow velocities are needed to validate these predictions.

The new knowledge presented in this work is valuable to ecosystem managers that control *E. crassipes* invasions. I expect that consideration of the ambient environmental conditions, particularly the water currents, would improve the effectiveness of existing control strategies. Using this new information, managers would have greater understanding of dispersal pathways and thus be able to take a proactive approach to managing an invasion. For invasions of other species of aquatic weeds, management can be similarly improved by adapting the model presented here.

2.5 Summary

Direct force measurements of water and air drag on free-floating *E. crassipes* rafts were obtained from experiments conducted in a flume and a wind tunnel. The force versus flow velocity data were used to estimate drag coefficients in water and air for rafts of varying geometry. Water drag exceeded air drag for similarly-sized rafts over the same Reynolds number regime. Water drag coefficients were stronger functions of Reynolds number than air drag coefficients; this difference is expected to be caused by greater flexibility in root elements compared to leaf canopy elements allowing for root canopy streamlining in higher water velocities. Evaluation of plant biomechanics indicated the roots, stolons, and petioles consist of similar material and the element shape determines flexural rigidity. As root canopy dimensions increased, water drag increased due to increased viscous drag. The flow interacted differently with the root structure of an individual plant compared to that of a raft assemblage.

Transport of free-floating macrophytes like *E. crassipes* is controlled by wind and water currents. Laboratory results demonstrate the importance of water-driven forcing; I conclude water currents will dominate ecological dispersal in systems with net water outflow (e.g., rivers, tidal systems), and free-floating macrophyte populations will tend to accumulate in quiescent areas of an ecosystem. This research serves as a foundation for the development of a physically-based predictive model of free-floating macrophyte dispersal that will improve efficiency of weed control efforts. Future work is needed to validate the transport model using field-scale observations.

Chapter 3

Structure of Flow Around Free-Floating Macrophytes, Part I: Water

In this chapter and the next, I explored the effects of free-floating macrophyte rafts on the surrounding water and air flows. Here, the objective of this experiment was to characterize the hydrodynamics of flow through and around root canopies of finite patches of live, free-floating macrophytes. In this laboratory study, I observed spatial development of mean and turbulent flow structure using high-frequency velocity measurements.

3.1 Background

3.1.1 Vegetated Flow Dynamics

Macrophytes modify the hydrodynamics of their environment by extracting fluid momentum (*Madsen and Warncke* 1983; *Gambi et al.* 1990). Macrophyte assemblages form canopies comprising the structural elements extending into the flow (i.e., leaves, stems, and/or roots). These outer-most regions are essential to the exchange processes of momentum, heat, and mass with the surrounding fluid (*Yi* 2008). Drag is fundamental to these processes, creating velocity gradients and eddies that lead to momentum loss of the fluid. The effectiveness of canopy elements in extracting momentum from the surrounding flow depends on canopy characteristics such as geometry, spacing, flexibility, and arrangement (*Yi* 2008).

Early studies of terrestrial vegetation canopies found the active turbulence to be dominated by large scale motions produced from velocity gradients above the canopy (*Raupach and Thom* 1981). Following *Raupach et al.* (1996), flow structure above terrestrial canopies is now understood to be similar to a mixing layer rather than a rough boundary layer, as was previously thought. A mixing layer is characterized by two coflowing streams of different velocities separated by a finite region of shear; the mean velocity profile of a mixing layer is represented mathematically by a hyperbolic tangent function (*Ho and Huerre* 1984),

$$U(z) = \overline{U}\left(1 + \frac{\triangle U}{2\overline{U}} \tanh\left(\frac{z - \overline{z}}{2\theta}\right)\right), \tag{3.1}$$

where $\overline{U} = 0.5\,(U_1 + U_2)$, $\Delta U = U_1 - U_2$, U_1 is the average velocity in the constant region outside the canopy, U_2 is the average velocity in the constant region inside the canopy, $\overline{z}$ is the height of $\overline{U}$, and θ is the momentum thickness of the mixing layer:

$$\theta = \int\limits_{-\infty}^{\infty} \left[\frac{1}{4} - \left(\frac{U - \overline{U}}{\Delta U}\right)^2\right] dz \tag{3.2}$$

This velocity profile contains an inflection point, which is a necessary criterion for hydrodynamic instability (*Drazin and Reid* 1981). A key property of this velocity profile is that it is inherently unstable, giving rise to Kelvin-Helmholtz vortices that define characteristics of the turbulence, including length scales, eddy structure, and rates of momentum transfer (*Ho and Huerre* 1984; *Raupach et al.* 1996).

Turning from terrestrial to aquatic environments, studies of both submerged and emergent macrophyte canopies have found similar results: a region of high velocity shear develops at the canopy-water interface (*Gambi et al.* 1990; *Ackerman and Okubo* 1993), forming a mixing layer (*Ghisalberti and Nepf* 2004; *White and Nepf* 2007). This type of flow strongly impacts mixing processes; the coherent eddies generated in mixing layer flow result in greater momentum transfer in the vertical direction than for boundary layer flows.

Unlike submerged and emergent macrophyte canopies, the hydrodynamics of root canopies in free-floating macrophytes are less studied. However, since the root canopy structure of free-floating macrophytes is fundamentally similar to that of submerged macrophytes, one can infer that the hydrodynamics are likewise analogous, and a mixing layer should develop. Several species of free-floating macrophytes reduce water quality by lowering dissolved oxygen content, pH, and bicarbonate alkalinity; on the other hand these species can also improve water quality by removing nutrients (e.g., nitrogen and phosphorus) and heavy metals in wastewater treatment applications (*Gopal* 1987; *Mishra and Tripathi* 2008). Despite these varied water quality impacts, little is known of the hydrodynamic interactions that control them. Therefore, this experiment was designed to characterize the hydrodynamics in root canopies of the free-floating macrophyte *E. crassipes.*

3.2 Materials and Methods

In a recirculating flume under steady flow conditions, I observed velocity fields around stationary assemblages of free-floating macrophytes ("rafts") over a range of flow velocities and raft lengths.

3.2.1 Vegetation

This research was conducted using the same *E. crassipes* individuals described in Chapter 2.2.1. To study flow development around *E. crassipes* root canopies, I constructed small rafts of vegetation in the laboratory. Braided spectra fiber line (PowerPro, $< 3\%$ elongation) was tied around the perimeter of the raft to simulate stationary patches with constant plant orientation and density. I observed flow around five rafts of similar geometry and plant density (Table 3.1). Plant densities used in this experiment were within the natural range for *E. crassipes* ($400-750$ leaves m^{-2}, corresponding to $7-40$ kg m^{-2} biomass density) (*Boyd and Scarsbrook* 1975; *Center and Spencer* 1981). To characterize root canopy density, I estimated the void fraction (porosity),

$$\begin{aligned} \phi &= \frac{V_{voids}}{V_{total}}, \\ \text{where } V_{voids} &= V_{total} - V_{solid} \end{aligned} \tag{3.3}$$

The total volume (V_{total}) was determined by measuring the dimensions of the root canopy as occurred during flow (i.e., in the deflected state). Side-looking photographs of the root canopy were used to measure the area along the longitudinal axis of the root canopy; canopy width was measured at 10 locations along the primary flow direction and multiplied by area estimates to calculate volume. The solid volume of the root canopy (V_{solid}) was measured as the total volume of water displaced by the raft while floating in still water.

3.2.2 Experimental Apparatus

Water velocity measurements were obtained in the recirculating laboratory flume described in Chapter 2.2.2. The working section of the flume was $10-13$ m from

Table 3.1: Root canopy dimensions, leaf density, and depth-averaged upstream water velocity (U_∞) for rafts used in water flow field experiments.

Root Canopy	Length, L (cm)	Width, b (cm)	Height, h_c (cm)	Leaf Density (total m^{-2})	U_∞ (cm s^{-1})
1	55	55	12	505	7.5
2	50	55	11	550	8.0
3	52	50	11	520	9.5
4	58	57	14	500	10.7
5	62	58	12.5	600	8.2

the upstream end. Water depth (H_w) for all experiments was 0.3 m and depth-averaged water velocity upstream of each canopy (U_∞) ranged from $7.5 - 10.7$ cm s^{-1} (Table 3.1).

3.2.3 Velocity Measurements

Velocity was measured using an acoustic Doppler velocimeter (ADV) (Vectrino, NortekUSA, Annapolis, MD, USA) mounted to a wheeled cart above the flume. The ADV was deployed in downward-looking mode and the sampling volume was aligned with the centerline of both flume and raft. The coordinate system is as follows: primary flow direction, x, with $x = 0$ and $x = L$ at the upstream and downstream edges of canopy, respectively; cross-stream direction, y, with $y = 0$ at the right side of the flume (looking downstream); and vertical direction, z, with $z = 0$ at the water surface and $z = -H_w$ at the bed (Figure 3.1). The corresponding velocity vector components are $\mathbf{u}(x, y, z) = u, v, w$.

Flow field structure was constructed from point measurements of velocity using two-dimensional linear interpolation, under the assumption of steady flow. For Root Canopy 1, vertical velocity profiles consisting of $5 - 7$ measurements were taken at eight positions along the length of the raft, plus three upstream and four downstream locations, for a total of 15 profiles and 81 point measurement locations (denoted by + in Figures 3.2-3.5). Velocity records were collected for five minutes at a sampling frequency of 25 Hz. Due to the configuration of the ADV probes, the uppermost 6 cm of the flow could not be sampled. Velocity measurements were taken outside the sidewall and bottom boundary layers, based on preliminary flume characterization. Because velocity was measured at one location in y, this experiment did not assess lateral variability in velocity field. To measure the velocity within the root canopy, roots from adjacent plants were moved out of the path between the ADV head and the sampling volume (located 5 cm below instrument) by either cutting root filaments or

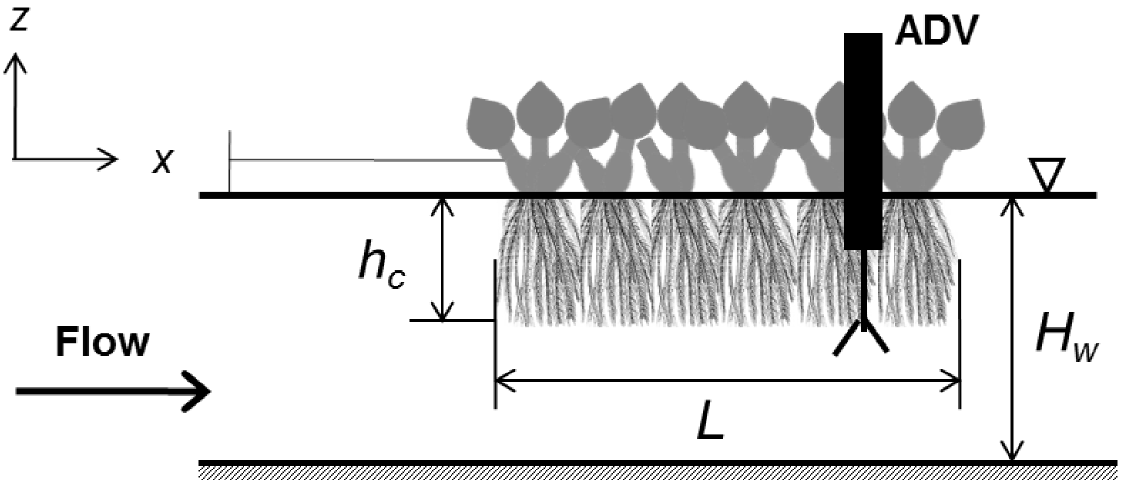

Figure 3.1: Schematic of experimental setup for water velocity measurements in recirculating flume with flow depth H_w. Velocity was measured using an acoustic Doppler velocimeter (ADV) within and around stationary floating root canopies of length L and height h_c. Water surface is denoted by ∇. Not to scale.

shifting plants laterally within the raft. A similar procedure has been used in studies of submerged vegetation canopies (*Ikeda and Kanazawa* 1996), and I expect the flow statistics were not appreciably changed by this procedure. Data were evaluated to ensure velocity records were not contaminated by root interference; contaminated records were evidenced by the presence of both non-physical velocity values (spikes) and low beam correlations. For Root Canopies $2-4$, this procedure was repeated but at lower spatial resolution in x and z; these results were used primarily to verify the presence of dominant flow features.

In addition to these flow fields, a high-resolution vertical profile of velocity was measured for Root Canopy 5 near the downstream end at $x = 43$ cm ($x/L = 0.7$), centered laterally. Records were collected using the ADV as for the flow fields; velocity was measured at 42 vertical locations between $z = -5.3$ and $z = -25.4$ cm, separated by $0.3 - 1$ cm. These results were used to examine the turbulent structure across the canopy-water interface in detail.

To ensure high-quality ADV data, I practiced common post-processing techniques (e.g., *Naden et al.* 2006). I used the following criteria for data quality: any individual beam correlation must be greater than 0.5; signal-to-noise ratio (SNR) must be greater than 15; and individual velocity components must be within three standard deviations of the mean value for each record. Data not meeting all of these criteria were removed and replaced by data interpolated from near neighbors. Because replacement of data in this way can lead to bias, only records for which fewer than 10% of points were replaced are included in the results. These data quality criteria resulted in elimination of the following number of records from the flow fields of Root Canopies $1-4$, respectively: four out of 81; two out of 35; two out of 84; and three out of 72. Additionally, two out of 42 records were eliminated for the Root Canopy 5 vertical profile.

The velocity statistics were computed as follows: for each velocity record, mean velocity components (U, V, W) were determined using a running mean filter with a window length of 10 seconds. The fluctuating velocity components (u', v', w') were calculated by subtracting each mean velocity component from that of instantaneous velocity (u, v, w),

$$\begin{aligned} u' &= u - U \\ v' &= v - V \\ w' &= w - W \end{aligned} \tag{3.4}$$

Reynolds stress for each record was computed as the average of the product of the x- and z-fluctuating velocities, $\overline{u'w'}$. Turbulent kinetic energy (q^2) was computed for each record as

$$q^2 = 0.5\left(\overline{u'^2} + \overline{v'^2} + \overline{w'^2}\right) \tag{3.5}$$

3.2.4 Analysis of Vertical Velocity Profile

Through further analysis of the vertical velocity profile obtained for Root Canopy 5, I explored details of the mean and turbulent flow structure for an *E. crassipes* root canopy. In particular, I explored whether the flow dynamics in root canopies were analogous to that in other vegetation canopies. For Root Canopy 5, the mean velocity profile in the root canopy was compared to the theoretical velocity profile for a mixing layer was calculated according to Equation (3.1).

To examine the turbulent structure, several turbulent parameters were computed for Root Canopy 5, including Reynolds stress, eddy viscosity, mixing length, skewness, quadrant analysis, co spectra, and mixing efficiency. Eddy viscosity (ν_t) was computed as the ratio of Reynolds stress to velocity shear at each height,

$$\nu_t(z) = \frac{\overline{u'w'}(z)}{S(z)}, \tag{3.6}$$

where $S(z)$ is velocity shear in the vertical direction $(\frac{\partial U}{\partial z})$, computed using central differencing at each height z_i,

$$S(z) = \left.\frac{\partial U}{\partial z}\right|_i = \frac{U_{i+1} - U_{i-1}}{z_{i+1} - z_{i-1}} \tag{3.7}$$

Mixing length (L_z), which describes the length scale of the turbulent motions, was computed at each height within the shear layer from the relation

$$L_z(z) = \sqrt{\frac{\nu_t(z)}{S(z)}} \tag{3.8}$$

As mixing length increases, a fluid parcel maintains its characteristics for a greater distance before mixing with the surrounding fluid, implying increased length scales of the turbulence.

To determine the structure of Reynolds stress in an *E. crassipes* root canopy, I calculated fluctuation velocity skewnesses and performed a quadrant analysis. Skewness (Sk) is computed as the third moment of the fluctuating velocity distribution at each height, shown here for the fluctuating velocity in x (u'),

$$Sk_u = \frac{\frac{1}{n}\sum_{i=0}^{n}\left(u'_i - \overline{u'}\right)^3}{\left(\sqrt{\frac{1}{n}\sum_{i=0}^{n}\left(u'_i - \overline{u'}\right)^2}\right)^3} \tag{3.9}$$

Substituting w in place of u in (3.9) yields the skewness of the fluctuating velocity in z (Sk_w). Skewness is a measure of the asymmetry of a distribution and describes its shape.

Quadrant analysis was performed to better understand the nature of turbulent events contributing to the Reynolds stress. Consider the plane created by plotting u' against w'. Here, classification of the quadrants of this plane is based on the sign of the fluctuating velocities as follows:

- Quadrant 1: Sweep ($u' > 0, w' > 0$);
- Quadrant 2: Inward interaction ($u' < 0, w' > 0$);
- Quadrant 3: Ejection ($u' < 0, w' < 0$);
- Quadrant 4: Outward interaction ($u' > 0, w' < 0$).

This classification, which deviates from that typically applied to vegetation canopies and traditional boundary layer flows (e.g., *Lu and Willmarth* 1973; *Raupach and Thom* 1981), results from the location of the canopy at the water surface. The fractional contribution to the Reynolds stress from each quadrant (F_Q) was computed as (*Lu and Willmarth* 1973)

$$F_Q = \frac{1}{T\overline{u'w'}\mid_{max}} \int_0^T C_Q(t)u'w'(t)dt, \tag{3.10}$$

where T is the record duration, $\overline{u'w'}\mid_{max}$ is the maximum value of Reynolds stress in the entire profile, and $C_Q(t)$ is the averaging condition,

$$C_Q(t) = \begin{cases} 1, & \text{if } [u'(t), w'(t)] \text{ is in the } Q\text{th quadrant} \\ 0, & \text{otherwise.} \end{cases} \tag{3.11}$$

Co spectra of u' and w' (S_{uw}) were calculated for three regions of the flow by taking the real part of the one-sided cross-spectral density function of u' and w' (*Bendat and Peirsol* 1986),

$$S_{uw}(f) = \Re\left(2\int_{-\infty}^{\infty} R_{uw}(\tau)e^{-j2\pi f\tau}d\tau\right), \tag{3.12}$$

where frequency f varies over $(0, \infty)$ and $R_{uw}(\tau)$ is the cross-correlation function between $u'(t)$ and $w'(t)$ at lag τ,

$$R_{uw}(\tau) = E\left[u'(t)w'(t+\tau)\right], \tag{3.13}$$

where E is the expected value operator. Cross-spectral density is the two-signal analog of autospectral density, applied via the Fourier transform of the cross-correlation function.

Finally, the mixing efficiency was computed as the ratio of Reynolds stress to the product of $x-$ and $z-$velocity standard deviations,

$$r_{uw} = \frac{|\overline{u'w'}|}{\sigma_u \sigma_w} \tag{3.14}$$

Higher values of r_{uw} indicate stronger correlation between u' and w', suggesting increased coherent motions.

3.3 Results

Porosity estimates for all canopies were greater than 95%.

3.3.1 Mean Flow Structure

The presence of the root canopy in the channel altered the mean flow structure. In all experimental canopies, flow was diverted around the root canopy, causing decreased velocities within the canopy and increased velocities in the open water below (Figures 3.2-3.5). For all root canopies, the streamwise velocity (U) continuously accelerated beginning at the upstream end of the canopy ($x/L = 0$), until a distance downstream between 50% and 70% of root canopy length (i.e., $0.5 \leq x/L \leq 0.7$) (Figures 3.2A-3.5A). It appears the distance to fully-developed flow conditions $\left(\frac{\partial U}{\partial x} \approx 0\right)$ depends inversely on the upstream channel velocity (U_∞). As channel velocity increased from $7.5 - 10.7$ cm s^{-1} for similar canopy dimensions and leaf densities (Table 3.1), the distance to fully-developed flow conditions decreased (Table 3.2). The cross-stream velocity (V) field was small for all canopies, with a magnitude less than 1 cm s^{-1} (Figures 3.2B-3.5B). The flow diversion began slightly upstream of the root canopy, where the vertical velocity sharply increased in magnitude in the downward direction. The mean vertical velocity (W) at the upstream end of the canopies was directed downward with a magnitude that increased as upstream channel velocity (U_∞) increased (Figures 3.2C-3.5C).

For Root Canopy 1 the mean velocity profile development is further visualized by inspection of mean velocity profiles (Figure 3.6). Here, we see that the streamwise velocity was reduced to less than 25% of the approach velocity within and downstream of the root canopy for normalized distances $0.5 \leq x/L \leq 1.9$ and heights $0.4 \leq z/h_c \leq 0.7$ (Figures 3.2A & 3.6). Despite the relatively short length of the rafts studied here, there was evidence for mixing layer development. Vertical profiles of $U(z)$ in Root Canopy 1 contained inflection points beyond 50% of canopy length ($x/L > 0.5$) (Figure 3.6). Velocity profiles downstream of the raft ($x/L > 1$) deviated from uniform upstream conditions, signaling a loss of fluid momentum (Figure 3.6).

3.3.2 Turbulent Flow Structure

The root canopy also altered the turbulent flow structure by generating turbulence at the canopy-water interface. This was observed for all canopies as increased Reynolds stress $\left(\overline{u'w'}\right)$ and turbulent kinetic energy (q^2) beginning around halfway along the canopy length (Figures 3.7-3.10). Using elevated Reynolds stress as a surrogate for the presence of a boundary layer at the canopy-water interface, it appears the boundary layer developed closer to the upstream end of the raft as flow velocity increased. This was evidenced as increased $\overline{u'w'}$ at lower values of normalized distance (x/L) for Root Canopies 1-4 (Figures 3.7A-3.10A), assuming that canopy geometry and densities are approximately equal for these canopies (Table 3.1).

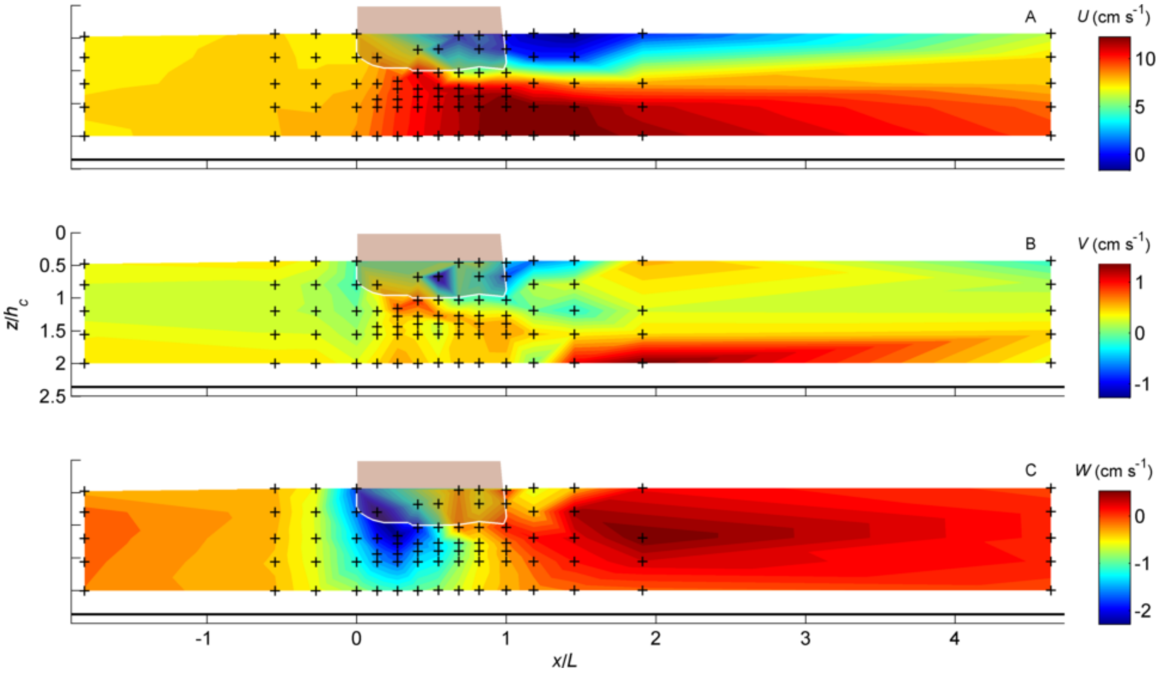

Figure 3.2: Contour plots of mean flow structure around Root Canopy 1 (shaded region outlined in white), based on discrete velocity measurements (denoted by +) along raft centerline. (A) mean streamwise (x) velocity, U; (B) mean cross-stream (y) velocity, V; and (C) mean vertical (z) velocity, W. Horizontal and vertical axes are scaled by root canopy length (L) and depth (h_c), respectively; flume bed is denoted by thick dark line near $z/h_c = 2.5$.

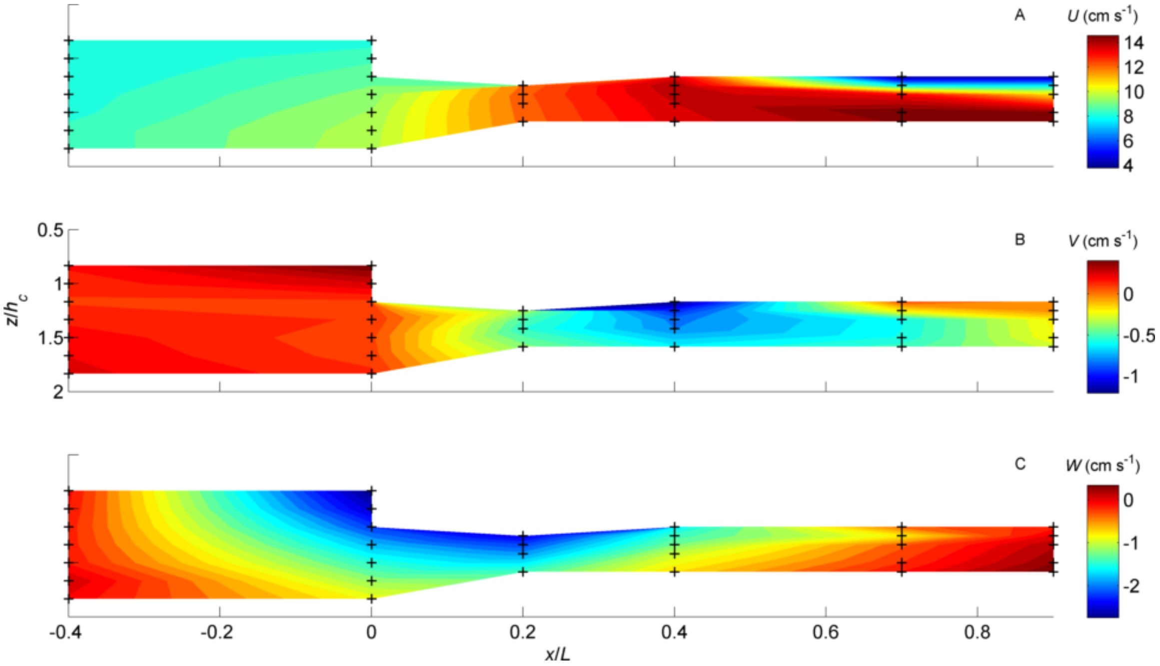

Figure 3.3: Contour plots of mean flow structure around Root Canopy 2, based on discrete velocity measurements (denoted by +) along raft centerline. (A) mean streamwise (x) velocity, U; (B) mean cross-stream (y) velocity, V; and (C) mean vertical (z) velocity, W. Root canopy extends vertically downward from water surface to $z/h_c = 1$ and horizontally from $x/L = 0$ to $x/L = 1$. Flume bed is located at $z/h_c = 2.7$ (not shown).

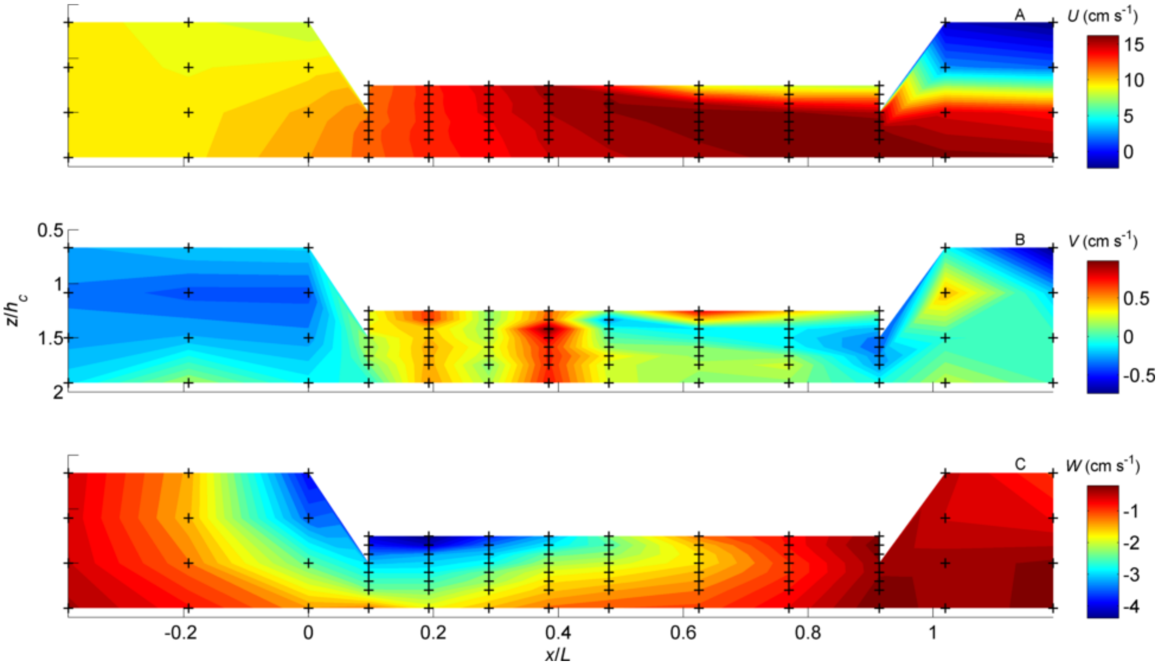

Figure 3.4: Contour plots of mean flow structure around Root Canopy 3 (white region), based on discrete velocity measurements (denoted by +) along raft centerline. (A) mean streamwise (x) velocity, U; (B) mean cross-stream (y) velocity, V; and (C) mean vertical (z) velocity, W. Root canopy extends vertically downward from water surface to $z/h_c = 1$ and horizontally from $x/L = 0$ to $x/L = 1$. Flume bed is located at $z/h_c = 2.7$ (not shown).

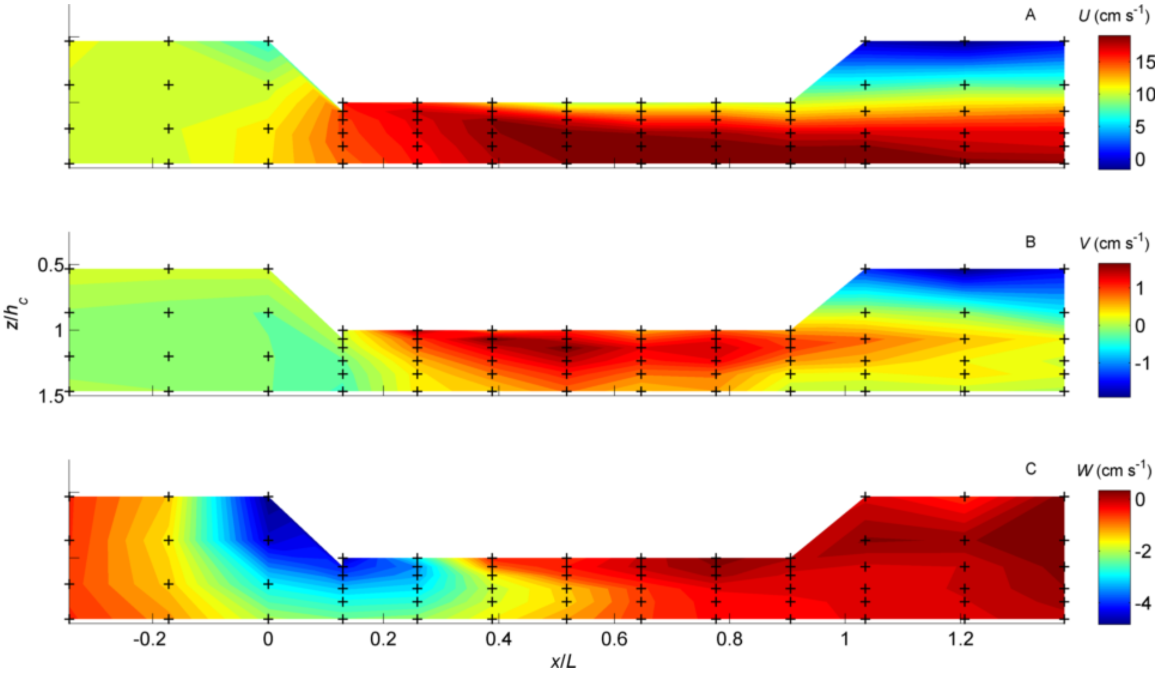

Figure 3.5: Contour plots of mean flow structure around Root Canopy 4, based on discrete velocity measurements (denoted by +) along raft centerline. (A) mean streamwise (x) velocity, U; (B) mean cross-stream (y) velocity, V; and (C) mean vertical (z) velocity, W. Root canopy extends vertically downward from water surface to $z/h_c = 1$ and horizontally from $x/L = 0$ to $x/L = 1$. Flume bed is located at $z/h_c = 2.1$ (not shown).

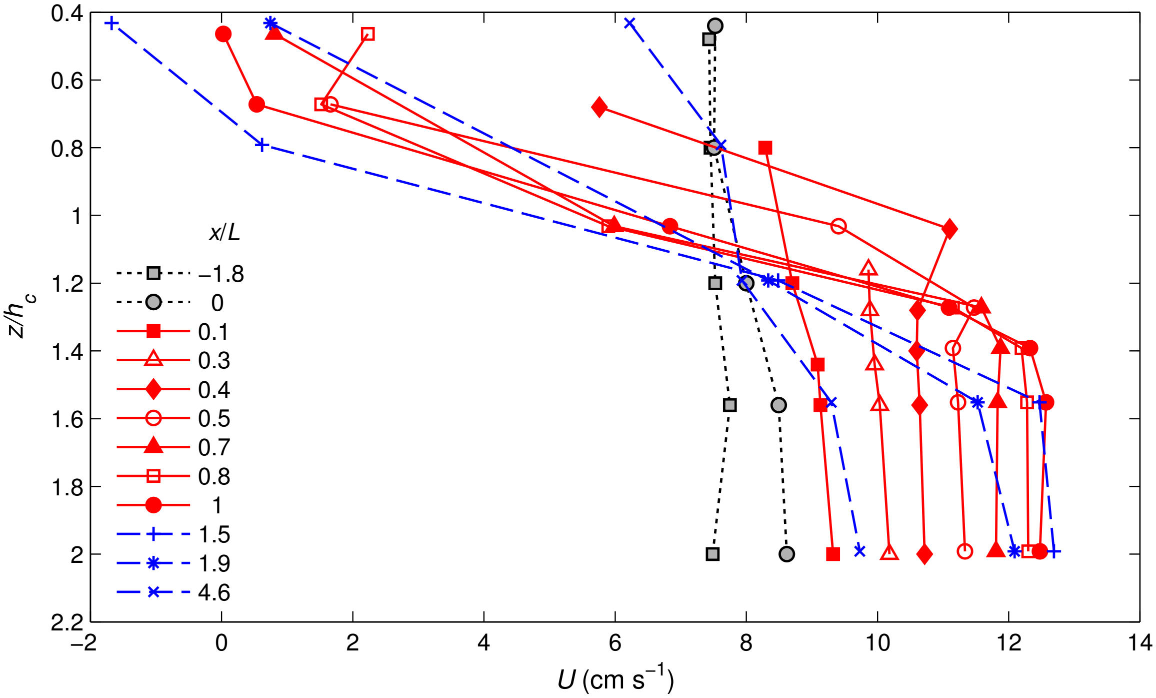

Figure 3.6: Flow development along the channel shown by vertical profiles of streamwise velocity ($U(z)$) for different $x-$locations, extracted from the Root Canopy 1 flow field of Figure 3.2A. Locations in x are normalized by raft length (L); vertical heights are normalized by root canopy depth (h_c). Root canopy extends vertically downward from water surface ($z/h_c = 0$, not shown) to $z/h_c = 1$. Gray symbols with short-dashed lines denote upstream locations ($x/L < 0$), red symbols denote under-canopy locations ($0 \leq x/L \leq 1$), and blue symbols with long-dashed lines denote downstream locations ($x/L > 1$). Velocity profile approaches fully-developed near $x/L \approx 0.7$.

Table 3.2: Comparison of normalized distance to fully-developed flow conditions (i.e., x/L where $\frac{\partial U}{\partial z} \approx 0$), normalized Reynolds stress ($\overline{u'w'}/U_\infty^2$), and normalized turbulent kinetic energy (q^2/U_∞^2) for varying depth-averaged upstream water velocities (U_∞). To facilitate comparison of normalized Reynolds stress and turbulent kinetic energy, the maximum values of $\overline{u'w'}$ and q^2 at $x/L = 1.2$ were used; Root Canopy 2 is omitted because velocity was not measured at this location. For similar canopy dimensions and leaf densities (Table 3.1), normalized distance to fully-developed flow decreases as U_∞ increases. Although both $\overline{u'w'}$ and q^2 increase as U_∞ increases, normalized values do not follow this pattern.

Root Canopy	U_∞ (cm s^{-1})	x/L where $\frac{\partial U}{\partial z} \approx 0$ [$-$]	$\overline{u'w'}/U_\infty^2$ [$-$]	q^2/U_∞^2 [$-$]
1	7.5	0.7	0.0192	0.0724
2	8.0	0.65	—	—
3	9.5	0.6	0.0440	0.1602
4	10.7	0.5	0.0263	0.1141

Although turbulent kinetic energy was elevated outside and downstream of the root canopy, it remained low within the root canopy (Figure 3.7B), suggesting the root canopy elements were too dense to allow appreciable turbulence production through vortex shedding. Downstream of the canopies, elevated levels of both Reynolds stress and turbulent kinetic energy signal the development of a wake region of recirculating flow (Figures 3.7, 3.9, and 3.10). This wake region suggests flow separation at the downstream end and the dominance of form drag. The positive Reynolds stresses (Figures 3.7A-3.10A) resulting from the canopy-flow interaction are opposite in sign of typical vegetation canopy studies. This difference in sign is caused by the choice of a conventional coordinate system with z increasing upwards. In traditional bottom boundary layer flows, the velocity decreases as z decreases; in contrast, for floating root canopies, velocity decreases as z increases towards the canopy.

The magnitudes of Reynolds stress and turbulent kinetic energy increased as flow velocity increased (Figures 3.7-3.10). However, when these quantities were normalized by the square of the upstream flow velocity (i.e., $\overline{u'w'}/U_\infty^2$ and q^2/U_∞^2), this pattern was not present; Root Canopy 3 had the highest values of normalized Reynolds stress and normalized turbulent kinetic energy (Table 3.2). Perhaps the slightly greater plant density of Root Canopy 3 (expressed as leaf density, Table 3.1) increased the relative turbulence in this case. Root Canopy 2 is omitted from this comparison because velocity was not measured at the common location of $x/L = 1.2$.

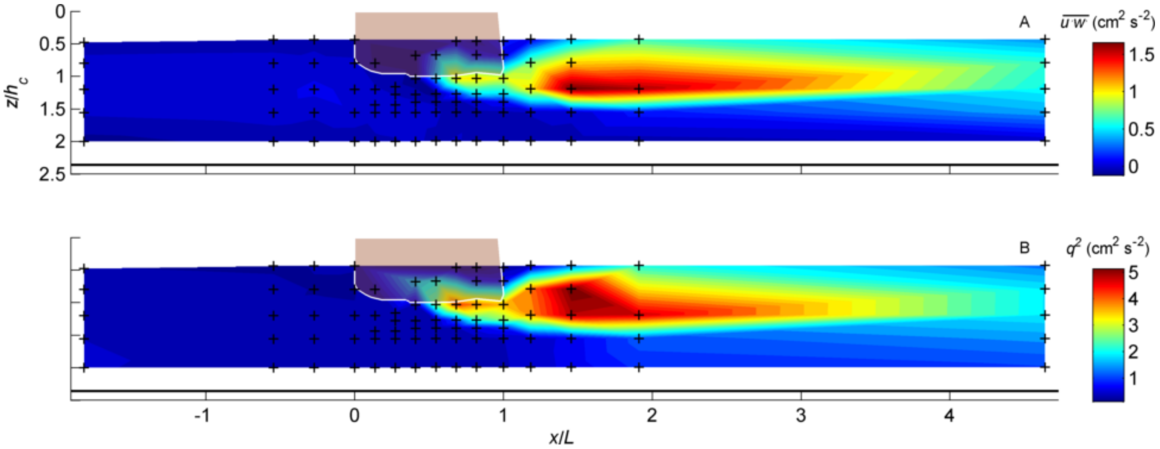

Figure 3.7: Contour plots of turbulent flow structure around Root Canopy 1 (shaded region outlined in white). (A) Reynolds stress $\left(\overline{u'w'}\right)$, and (B) turbulent kinetic energy (q^2). Axis scaling and symbols as for Figure 3.2.

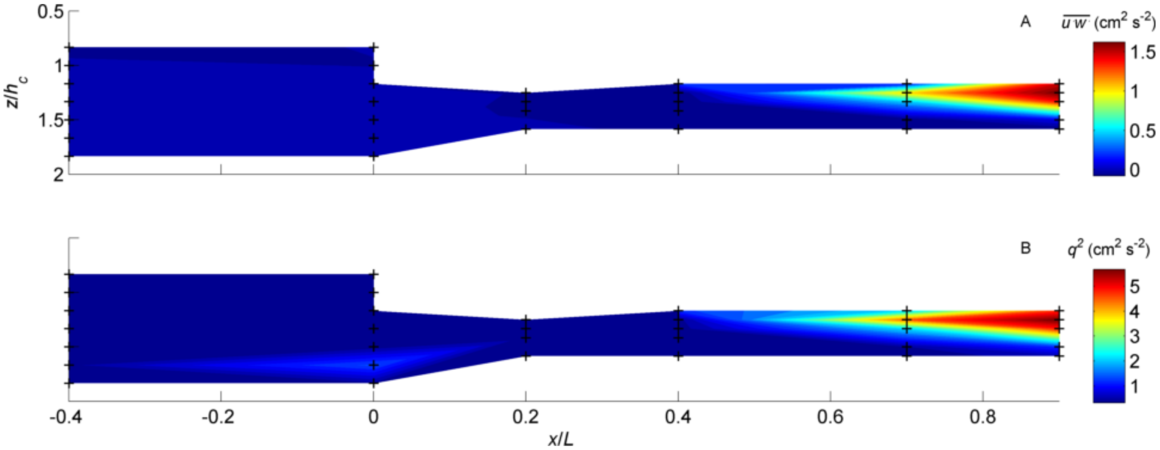

Figure 3.8: Contour plots of turbulent flow structure around Root Canopy 2. (A) Reynolds stress $\left(\overline{u'w'}\right)$, and (B) turbulent kinetic energy (q^2). Axis scaling and symbols as for Figure 3.3.

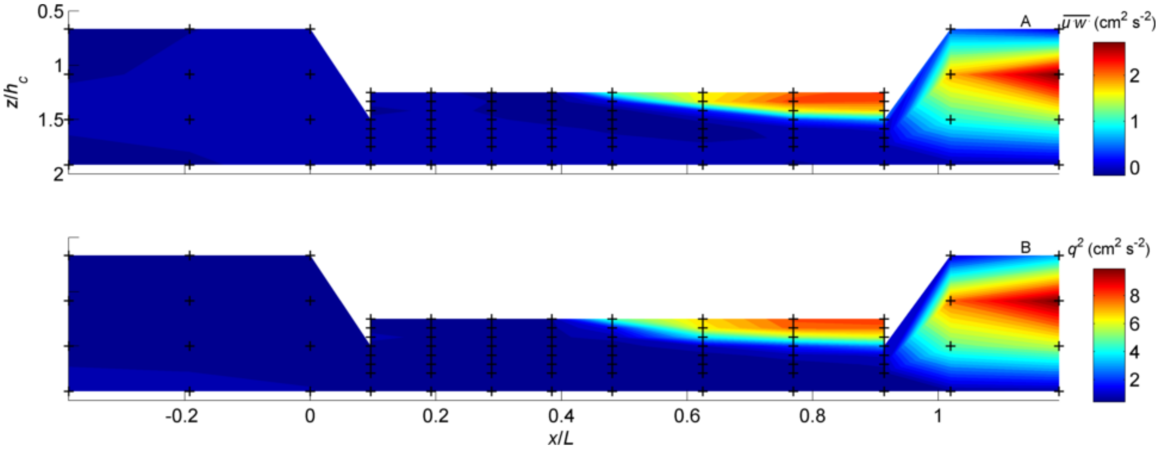

Figure 3.9: Contour plots of turbulent flow structure around Root Canopy 3 (white region). (A) Reynolds stress $\left(\overline{u'w'}\right)$, and (B) turbulent kinetic energy (q^2). Axis scaling and symbols as for Figure 3.4.

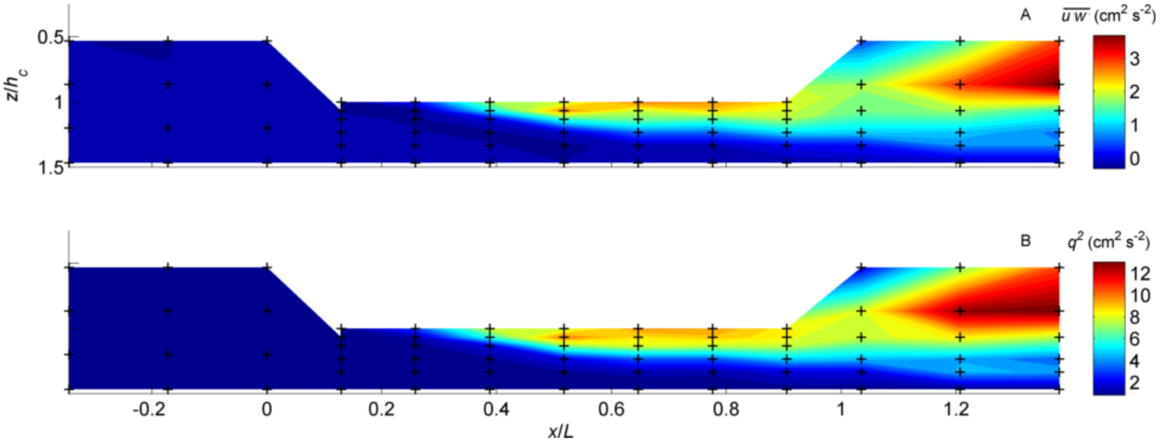

Figure 3.10: Contour plots of turbulent flow structure around Root Canopy 4 (white region). (A) Reynolds stress $\left(\overline{u'w'}\right)$, and (B) turbulent kinetic energy (q^2). Axis scaling and symbols as for Figure 3.5.

3.3.3 Detailed Vertical Structure of Velocity

In the high-resolution vertical profile (Root Canopy 5), the streamwise velocity profile had multiple inflection points in the region below the root canopy ($z/h_c > 1$) and was reasonably described by the theoretical shape of a mixing layer given by Equation (3.1) (Figure 3.11A). Vertical profiles of velocity shear ($\partial U/\partial z$) and Reynolds stress $\left(\overline{u'w'}\right)$ demonstrate double, coincident peaks located at the canopy edge ($z/h_c = 1.03$) and further beneath ($z/h_c = 1.3$) (Figure 3.11B). The peaks in velocity shear were of similar magnitude while those of Reynolds stress were not; the upper peak in Reynolds stress was less than half the value of the peak beneath. Peaks in Reynolds stress suggest the presence of coherent vortices, as expected in a mixing layer (*Raupach et al.* 1996). The Reynolds stress within the root canopy ($z/h_c < 1$) was uniformly low, increasing only within the last 2 cm of the canopy (Figure 3.11B). This suggests a small region of rapid exchange with the outside flow.

The eddy viscosity profile (Figure 3.12A) had a similar shape to that of Reynolds stress (Figure 3.11B), with a smaller peak at the canopy edge and a larger peak several centimeters below. Mixing length slightly increased with depth outside the canopy (Figure 3.12B); for a true mixing layer, we expect the mixing length to remain constant with depth outside the canopy (*Poggi et al.* 2004). Profiles of turbulence intensities (represented by the standard deviations of the velocities, σ_u and σ_w) had shapes similar to eddy viscosity—low values were present inside the root canopy, increasing through the outer shear zone (Figure 3.12). Outside the shear layer, mixing length became ill-defined due to low values of shear and was not calculated in these regions.

In this study, sweep motions were found predominantly at the outer edge of the canopy, while ejections were present outside the canopy in the lower region of high shear (Figure 3.13A). The combination of $Sk_u > 0$ and $Sk_w > 0$ implies sweep motions (high momentum fluid moving upward into the canopy) while $Sk_u < 0$ and $Sk_w < 0$ implies ejections (low momentum fluid moving downward out of the canopy). This was confirmed from the quadrant analysis, which demonstrates that sweeps (Q1) dominated from the outer edge of the canopy to a location 2 cm below the canopy edge and ejections (Q3) dominated for the next 5 cm of depth, through the lower region of high shear (Figure 3.13B). These results agree with those of velocity skewnesses.

The regions of elevated Reynolds stress (Figure 3.11B) correspond to regions of coherent velocity structures. Within the mixing layer region, co spectra demonstrate elevated turbulent energy at specific frequencies: along the canopy edge, the peak frequency was 0.4 Hz; outside the canopy in the highest-stress region, the peak frequency reduced to 0.2 Hz and increased in co spectral density density by 50% (Figure 3.14A). This transition to lower frequencies with higher co spectral density outside the canopy

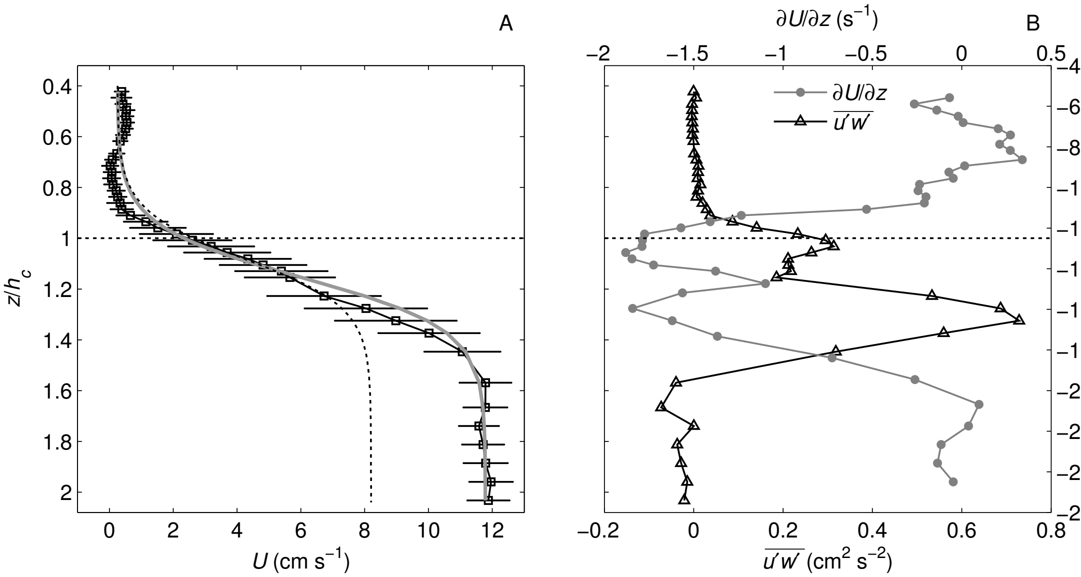

Figure 3.11: (A) Vertical profile of streamwise velocity (U) for Root Canopy 5 (approach velocity, $U_\infty = 8.2$ cm s^{-1}) at $x/L = 0.7$. Error bars represent one standard deviation. Gray line denotes hyperbolic tangent velocity profile of a mixing layer given by Equation (3.1) for $U_1 = 11.75$ cm s^{-1} and $U_2 = 0.25$ cm s^{-1} ($\theta = 1.28$ cm, calculated from Equation (3.2)). Dashed dark line denotes hyperbolic tangent velocity profile with $U_1 = 8.2$ cm s^{-1}, $U_2 = 0.25$ cm s^{-1}, and $\theta = 1.2$ cm. (B) Vertical profiles of velocity shear ($\partial U/\partial z$) and Reynolds stress $\left(\overline{u'w'}\right)$ for Root Canopy 5 at $x/L = 0.7$. Root canopy extends from water surface ($z = 0$) to canopy depth, h_c, denoted by dashed horizontal lines at depth $z = -12.5$ cm and at normalized depth $z/h_c = 1$.

suggests the development of larger-sized coherent velocity structures. Strong correlations between u' and w' were further evidenced by the peaks in mixing efficiency. The main peaks in r_{uw} (at $z = -12.5$ and -17.2 cm, Figure 3.14B) correspond to the locations of the co spectral peaks (Figure 3.14A) and to the locations of sweeps and ejections (Figure 3.13).

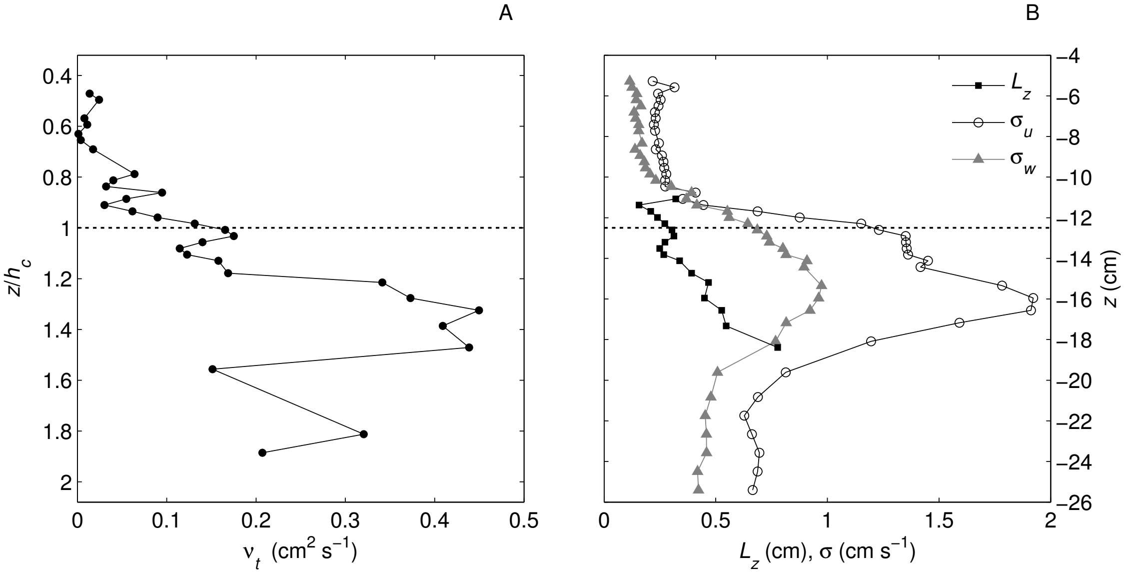

Figure 3.12: Vertical profiles of (A) eddy viscosity (ν_t), (B) mixing length (L_z), and turbulence intensities of u and w (σ_u, σ_w) for Root Canopy 5. Low values of eddy viscosity and turbulence intensity are evident within the root canopy. Root canopy extends from water surface ($z = 0$) to canopy depth, h_c, denoted by dashed horizontal lines at depth $z = -12.5$ cm and at normalized depth $z/h_c = 1$.

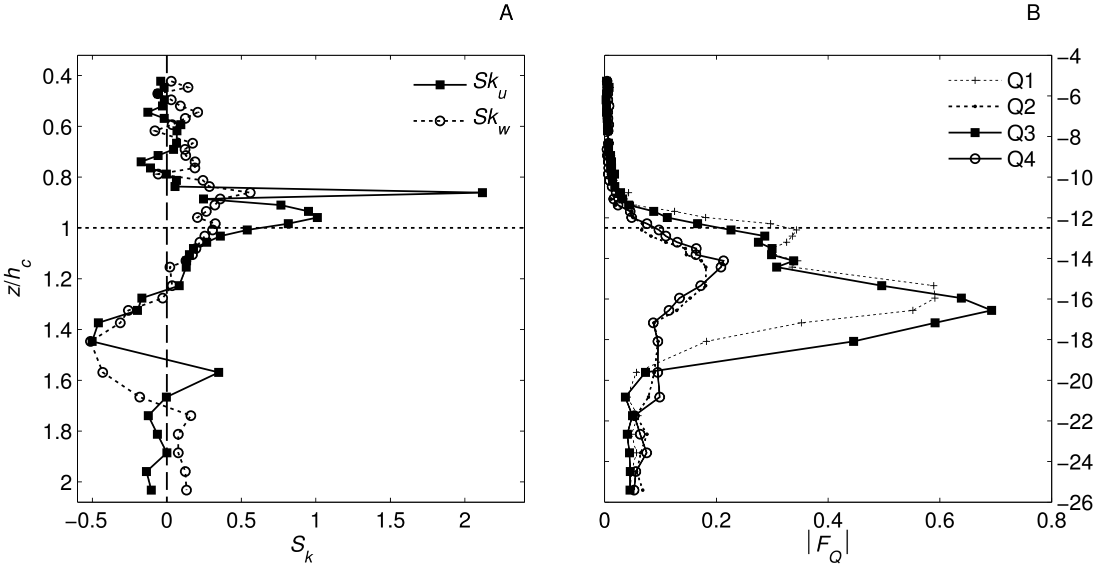

Figure 3.13: Vertical profiles of (A) velocity component skewness (S_k) and (B) fractional contribution to shear stress from the Qth quadrant ($\mid F_Q \mid$) for Root Canopy 5. The predominance of sweeps ($u' > 0$ and $w' > 0$) along the outer edge of the root canopy ($-11.9 > z > -13.2$) is seen in (A) as $Sk_u > 0$ and $Sk_w > 0$ and in (B) as $\mid F_1 \mid > \mid F_3 \mid$. Similarly, the predominance of ejections ($u' < 0$ and $w' < 0$) in the open water beyond the root canopy ($-15.9 > z > -18.1$) is seen in (A) as $Sk_u < 0$ and $Sk_w < 0$ and in (B) as $\mid F_1 \mid < \mid F_3 \mid$. Root canopy extends from water surface ($z = 0$) to canopy depth, h_c, denoted by dashed horizontal lines at depth $z = -12.5$ cm and at normalized depth $z/h_c = 1$.

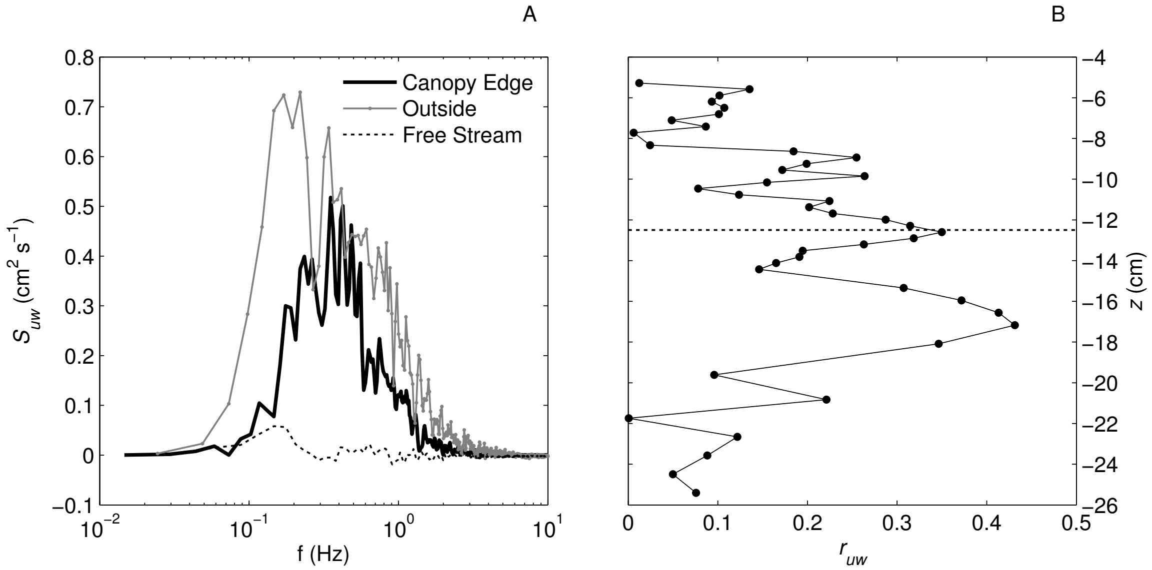

Figure 3.14: (A) Co spectra of u' and v' (S_{uw}) averaged over three regions of the velocity profile for Root Canopy 5: *1*) root canopy edge (heavy line, $-11.9 > z > -13.2$); *2*) outside the root canopy, in the lower region of high stress and shear (thin line, $-15.9 > z > -18.1$); and *3*) free stream (dashed line, $-21.7 > z > -25.4$). Co spectral densities elevated above free stream levels demonstrate the presence of coherent velocity structures produced from the canopy-flow interaction. Higher co spectral densities at lower frequencies outside the canopy suggest a transition to larger-sized coherent velocity structures. (B) Vertical profile of mixing efficiency (r_{uw}) for Root Canopy 5, demonstrating that locations of highest mixing efficiency coincide with those of the coherent structures shown in (A). Root canopy extends from water surface ($z = 0$) to canopy depth, h_c, denoted by dashed horizontal line at depth $z = -12.5$ cm.

3.4 Discussion

These results indicate that free-floating *E. crassipes* rafts strongly impacted the hydrodynamics by deflecting flow around the root canopy and inducing a mixing layer. Flow deflection and mean velocity reduction have also been observed in leaf canopies of submerged aquatic vegetation, including flexible seagrasses (*Gambi et al.* 1990), kelp forests (*Gaylord et al.* 2007), and individual plants of less-flexible, branching macrophytes (*Green* 2005). For channels invaded by *E. crassipes*, this large reduction in mean velocity through the root canopy reduces flow conveyance (*Gopal* 1987). The root canopy of *E. crassipes* rafts exerts high flow resistance and therefore results in a sharp gradient between internal and external velocities, as has been shown for leaf canopies of submerged macrophytes (*Sand-Jensen and Mebus* 1996). This sharp velocity gradient induces an inflectional streamwise velocity profile (Figure 3.11A), creating the requisite instability for mixing layer development (*Drazin and Reid* 1981). Mixing layers have been observed in other vegetation canopies, both terrestrial and aquatic; however these other canopies comprised stems and leaves, rather than roots as in this study (*Raupach and Thom* 1981; *Ghisalberti and Nepf* 2002).

There were several similarities observed in the vertical structure of turbulence between the root canopy of *E. crassipes* and leaf canopies of other plant species. As in other studies of canopy flow dynamics, sweeps were observed at the outermost region of the canopy, and ejections were observed beyond the canopy in the open water (*Ghisalberti and Nepf* 2006). Increased mixing efficiency outside the canopy, as observed in this study (Figure 3.14B) suggests more-organized turbulence and is a typical feature of vegetation canopies (*Raupach et al.* 1996). The small values of Reynolds stress and eddy viscosity within the root canopy suggest that limited exchange occurs between the root canopy and open water, which has been shown for submerged macrophytes (e.g., *Ackerman and Okubo* 1993; *Ghisalberti and Nepf* 2006). In this study, the exchange zone (region of non-zero Reynolds stress within the canopy) was particularly small, only reaching 20% of the canopy height; in contrast, the exchange zone of model submerged vegetation studied by *Ghisalberti and Nepf* (2006) extended 65% of the canopy height. I attribute this small exchange zone to the high flow resistance of the root canopy.

In this experimental setup, the flow depth was slightly more than two times the root canopy height. This flow depth to canopy height ratio is considered to be at the transition between "confined" and "unconfined" flow conditions in submerged macrophyte canopies (*Nepf and Vivoni* 2000). Assuming this value of the ratio applies to the inverted canopy studied here, this experimental setup led to confined flow conditions. If so, the velocities measured within the canopy were higher than expected for unconfined conditions. For unconfined conditions, the shear stress at the outer edge of the canopy is the dominant force driving flow inside the canopy, opposed by form drag from canopy elements (*Raupach et al.* 1991). For confined conditions, the contribution of shear is negligible because the primary momentum balance is between the external pressure gradient and form drag, thereby forcing more flow inside the canopy (*Nepf and Vivoni* 2000). Given that there was a large wake region downstream of the raft and low stresses within the canopy (Figure 3.7), I suspect that confined conditions were present in this study. However, since confined conditions occur in natural settings, these results have real-world applications.

Two unique results of this study are the double, coincident peaks in both velocity shear and Reynolds stress profiles (Figure 3.11B). Other studies of terrestrial and aquatic leaf canopies demonstrate a single peak in Reynolds stress near the canopy edge and subsequent decrease outside the canopy; here I found a peak in Reynolds stress near the canopy edge followed by a short region of decreased magnitude and then a second peak of higher magnitude. I expect that the upper, smaller peak in Reynolds stress is the one typical of mixing layers, caused by the discontinuity of drag from the root canopy. As described previously, there was a region of accelerating flow beneath the first half of the canopy, suggesting an elevated pressure gradient, indicative of confined flow conditions (Figure 3.2A). Inspecting the velocity profile in the region between the two peaks in Reynolds stress, there was a shift toward higher velocity coincident with the local maximum in velocity shear at $z/h_c = 1.2$ (Figure 3.11). Given potentially confined flow conditions, I attribute this shift in velocity to the external pressure gradient forcing flow underneath the root canopy, leading to the additional inflection points present in the velocity shear profile (Figure 3.11B). This scenario may cause a second hydrodynamic instability, which may explain the second peaks in both Reynolds stress and velocity shear located outside the root canopy. For unconfined conditions, I expect the free stream velocity outside the root canopy to approach that of the upstream water velocity (U_∞); this hypothetical velocity profile qualitatively fits the experimental data through the root canopy down to the location of the previously-described shift in velocity, $0.4 \leq z/h_c \leq 1.2$, (dashed dark line in Figure 3.11A). These results suggest that thresholds for confined flow conditions in vegetation canopies depend not only on the ratio of canopy height to water depth, but also on the flow resistance of the canopy.

One limitation of this study is the lack of multiple sampling locations in the cross-stream (y) direction, meaning secondary circulation was not readily identified in this experimental setup. However, the measured mean y-velocity was quite small ($O(1 \text{ cm s}^{-1})$, Figures 3.2B-3.5B), and Root Canopies 1-4 had qualitatively similar mean and turbulent flow fields, suggesting secondary circulation (if any) does not significantly impact the flow structure. Another limitation was the difficulty in assessing root canopy density using definitions commonly used in canopy studies (e.g., leaf area index, frontal area per unit volume, etc.). The high porosities obtained in this study were unexpected considering the high density of root elements, which prevented light from passing through the width of the canopy.

3.4.1 Canopy Residence Times

For Root Canopy 5, I compared two estimates of canopy residence time: horizontal advection through the canopy and vertical diffusion across the canopy-water interface. The former was estimated as $T_A \approx L/U$, where L is the canopy length (60 cm) and U is the average velocity within the canopy (0.25 cm s^{-1}). The latter was estimated as $T_D \approx H^2/K$, where H is the canopy height (12.5 cm) and K is the diffusion coefficient. In this case, I assumed $K \approx \nu_t$, taking ν_t as the average value within the canopy (0.05 cm^2 s^{-1}, Figure 3.12). From these estimates, I found T_A (240 s) was one order of magnitude lower than T_D (3100 s) for this particular combination of root canopy geometry and flow conditions, suggesting that horizontal advection controls residence time for small patches of *E. crassipes.* Extrapolating to larger patches, I estimated (using these same values of U and H) that the timescale of vertical diffusion would equal that of horizontal advection (i.e., $T_D \approx T_A$) for a raft length of $L \approx$800 cm, or 13 times longer than the raft studied here. This implies that for *E. crassipes* growing in large patches (common in invaded ecosystems), one would expect vertical diffusion to control canopy residence time given sufficient flow velocity, as in a riverine ecosystem. However, it is important to note that horizontal advection may dominate if flow velocity is sufficiently reduced. As U decreases, one would expect the vertical velocity shear would also decrease. This would further reduce ν_t, and by implication, K, thereby reducing turbulent mixing across the canopy-water interface. Therefore, in low velocity environments, the canopy residence time in large patches is most likely controlled by horizontal advection. The velocity structure in large patches of *E. crassipes* should be studied to further understand mechanisms controlling residence time in the root canopy.

3.4.2 Significance to Aquatic Environments

Root canopies of free-floating macrophytes like *E. crassipes* alter local hydrodynamic conditions; the impact of these free-floating macrophytes on their environment is affected by exchanges of momentum and mass between the root canopy and the open water. Although turbulent mixing is increased outside the root canopy, I observed very limited turbulent exchange between the root canopy and open water. This suggests horizontal advection of the mean flow is the dominant mechanism of exchange. Understanding the interaction between flow and plant canopies is essential to the numerical modeling of ecosystems with large populations of free-floating macrophytes.

These observations suggest an important mechanism by which *E. crassipes* inhibits reaeration of water bodies. It is generally accepted that free-floating macrophytes reduce dissolved oxygen in two manners: first, they have leaves above the water surface that respire oxygen to the atmosphere directly; second, they grow in dense mats at the water surface, which both inhibits the diffusion of oxygen into water through reaeration and reduces photosynthetic activity of submerged vegetation. As we have seen here, when *E. crassipes* covers the entire width of the channel, velocity within the root canopy is greatly reduced from that upstream. Related to the second point, I suggest that this low velocity near the water surface, in addition to the presence of the leaf canopy above water, inhibits reaeration in ecosystems heavily invaded by *E. crassipes*.

Further understanding of root canopy hydrodynamics can increase removal efficiencies in phytoremediation applications of free-floating macrophytes like *E. crassipes*. Water velocity is reduced within the canopy because of vegetative-induced drag, leading to deflection of flow around the canopy. Given this high degree of flow defection, operating conditions in phytoremediation applications should be carefully selected. Flow depth and velocity should be chosen to avoid flow deflection since this leads to partial diversion of the flow and subsequent reduction in removal efficiencies. Biological uptake is the major process for nutrient removal by *E. crassipes*; in turn, nutrient removal is directly related to growth rates (*Reddy and Sutton* 1984). Under favorable conditions, growth rates in *E. crassipes* are high even in low-velocity environments (*Reddy and Tucker* 1983; *Henry-Silva et al.* 2008); *Yi et al.* (2009) found that ammonium removal increased as hydraulic retention time increased (increased retention time implies lower flow velocity). These findings suggest that biological uptake in *E. crassipes* is not limited by mass-transfer processes and instead is limited by reaction kinetics (*Sanford and Crawford* 2000). To improve removal efficiencies of *E. crassipes*, we seek the operating conditions that maximize rates of biological uptake. This requires further study of uptake in *E. crassipes* to determine equilibrium conditions where rate of mass transfer just equals that of kinetic reactions, which will ensure maximum removal efficiency.

3.5 Summary

Laboratory experiments were performed in a recirculating flume to observe the hydrodynamic effects of *E. crassipes* root canopies. Under steady flow, the velocity structure around several root canopies was measured using an ADV. In addition, for one canopy a high-resolution vertical profile of velocity was obtained from the region of fully-developed flow; these data were used to examine the details of the turbulent flow structure across the canopy-water interface.

Results indicate that the presence of the root canopy in the channel altered the mean and turbulent flow structure. Flow was diverted around the root canopy and turbulence was generated at the canopy-water interface. As upstream water velocity increased, the distance to fully-developed conditions decreased and absolute values of both Reynolds stress and turbulent kinetic energy increased. Velocity profiles beneath the root canopy contained inflection points within the fully-developed region. The detailed vertical profile of mean streamwise velocity had the characteristic shape of a mixing layer, as seen in other forms of vegetated flows, which suggests the presence of hydrodynamic instabilities. The turbulent structure across the canopy-water interface demonstrated similarities to other vegetation canopies, along with important differences. As in other canopies, sweeps were observed at the canopy edge and ejections were observed in the open water beyond. The Reynolds stress profile featured two distinct peaks, a divergence from existing studies of vegetated canopies, perhaps caused by confined flow conditions. Regions of elevated Reynolds stress corresponded to regions of coherent velocity structures. Although turbulent mixing was increased outside the root canopy, I observed very limited turbulent exchange between the root canopy and the open water. This implies low momentum flux across the canopy-water interface; therefore in root canopies having similar structure to *E. crassipes*, I expect residence time is dominated by horizontal advection.

Chapter 4

Structure of Flow Around Free-Floating Macrophytes, Part II: Air

Similarly following Chapter 3, the objective of this experiment was to characterize the dynamics of air flow around leaf canopies of finite patches of live, free-floating macrophytes. In this laboratory study, I observed spatial development of mean and turbulent flow structure using high-frequency velocity measurements. Assimilating the results of this and the previous chapter, I compare the fluid-dynamic effects of leaf and root canopies.

4.1 Background

Landscapes are rarely uniform; instead they comprise a mosaic of land patches, each with different characteristics that affect momentum, mass, and energy transfer. A primary factor in the spatial variability of a landscape is the presence and type of vegetation; in this context, an assemblage of vegetation is called a canopy.

Terrestrial vegetation canopies are classified by the characteristics of their spatial structure: homogeneous (e.g., grasses, agricultural crops) or heterogeneous (e.g., deciduous forests). Additionally, canopies are classified by their size (i.e., land area coverage): uniform (i.e., horizontally extensive) and patchy. In terms of understanding the effects of a canopy on the surrounding atmospheric flow, the simplest case is the uniform homogeneous canopy. Studies of this class of canopies have shown that canopy turbulence and exchange is dominated by large eddies with length scales comparable to the canopy height (*Belcher et al.* 2008). The source of these eddies is the mean velocity profile, which contains an inflection point and is inherently unstable. As described in Chapters 1 and 3, the turbulence structure at the top of terrestrial vegetation canopies resembles that of a mixing layer. When considering the case of patchy vegetation, it is necessary to understand the effects of canopy edges on the surrounding flow.

4.1.1 Flow Across a Canopy Edge

As wind flows over a canopy edge, it adjusts to the change in surface roughness. This adjustment is observed as a spatial development of the mean wind. *Belcher et al.* (2003) identified several regions of adjustment, presented here as if traveling upwind to downwind along a canopy: upwind of the canopy is an *impact region* where the wind is decelerated by a pressure gradient caused by drag of canopy elements; just beyond the upwind canopy edge is an *adjustment region* where canopy drag decelerates wind speed within the canopy; further downwind and above the canopy is a *roughness change region* where the wind has fully adjusted to the change in roughness (i.e., fully-developed flow conditions are attained); within one canopy height of the downwind edge is an *exit region* where the mean wind suddenly increases in response to the removal of canopy drag; finally, beyond is the *wake region*, where the wind profile recovers back to its typical logarithmic profile (assuming the roughness of the subsequent landscape is low). In the adjustment region, there is mass flux out of the top of the canopy because of the reduced horizontal mass flux through the canopy. In the roughness change region, an internal boundary layer develops where the mean wind profile develops a logarithmic form adjusted to the canopy roughness with a displacement height (*Belcher et al.* 2003). *Morse et al.* (2002) observed that Reynolds stress changes very little in the adjustment region of the flow; instead the Reynolds stress adjusts farther downwind, caused by flow distortion at the upwind edge of the canopy.

Although free-floating macrophytes grow at the water surface and not on land, they do grow in patches and therefore have canopy edges. Based on the description of *Belcher et al.* (2003), it is expected that a similar adjustment of the mean wind profile will occur over patchy (i.e., finite) leaf canopies of free-floating macrophytes. In this laboratory experiment, I observed the structure of wind velocity around stationary, finite patches of free-floating macrophytes.

Table 4.1: Leaf canopy dimensions, leaf density, and water temperature for rafts used in air flow field experiments. Upwind air velocity at mid-height (U_∞) was 1.6 m s^{-1} for all canopies.

Leaf Canopy	Length, L (cm)	Width, b (cm)	Height, h_c (cm)	Leaf Density (total m^{-2})	Water Temperature, T_w (°C)
1	65	55	6.5	485	19.5
2	70	62	7.3	505	19.5
3	100	70	7.4	537	21.0

4.2 Materials and Methods

4.2.1 Vegetation

I studied flow development around *E. crassipes* leaf canopies in the laboratory, using the same individuals described in Chapter 2.2.1. Braided spectra fiber line was tied around the perimeter of the vegetation to simulate stationary patches with constant plant orientation and density. I observed air flow around three rafts of similar geometry and plant density (Table 4.1). For Leaf Canopies 1 and 2, velocity profiles were collected along the canopy length; for Leaf Canopy 3, a transect of velocity at one height above the canopy was collected along its length. To compare the effect of leaf and root canopies on the flow dynamics, flow fields were observed for one particular raft in both the wind tunnel (Leaf Canopy 2, Table 4.1) and the flume (Root Canopy 1, Table 3.1). As explained previously, plant densities used in this experiment were within the natural range for *E. crassipes* ($400-750$ leaves m^{-2}, corresponding to $7-40$ kg m^{-2} biomass density) (*Boyd and Scarsbrook* 1975; *Center and Spencer* 1981).

4.2.2 Experimental Apparatus

Air velocity measurements were obtained in a wind tunnel of dimensions of 4 m length, 0.8 m width, and 0.53 m height (H_a). This wind tunnel had an attached water basin filled with freshwater to a depth of 0.47 m. The experimental setup is represented schematically in Figure 4.1 and shown in Figure 4.2. The vegetation rafts were held stationary in the flow by spectra line attached to the upwind end of the wind tunnel. This setup allowed the buoyant plants to both float and interact with the flow naturally (Figure 4.3). Unidirectional flow was created by an outward-facing fan (Reynor, USA) located at the downwind exit controlled by a variable autotransformer (Variac). The working section of the wind tunnel was $2-3$ m from the upwind end.

For all leaf canopies, a constant fan voltage of 70 V was used, which generated an upwind air velocity (U_∞) of 1.6 m s^{-1}, measured at the midpoint of the air space ($z/H_a = 0.5, z = 0.265$ m). The water was allowed to thermally equilibrate with the atmosphere for at least 12 hours. Water temperatures were constant during each flow field experiment, ranging 19 – 21°C, within 5°C of the air temperature (as measured by the anemometer).

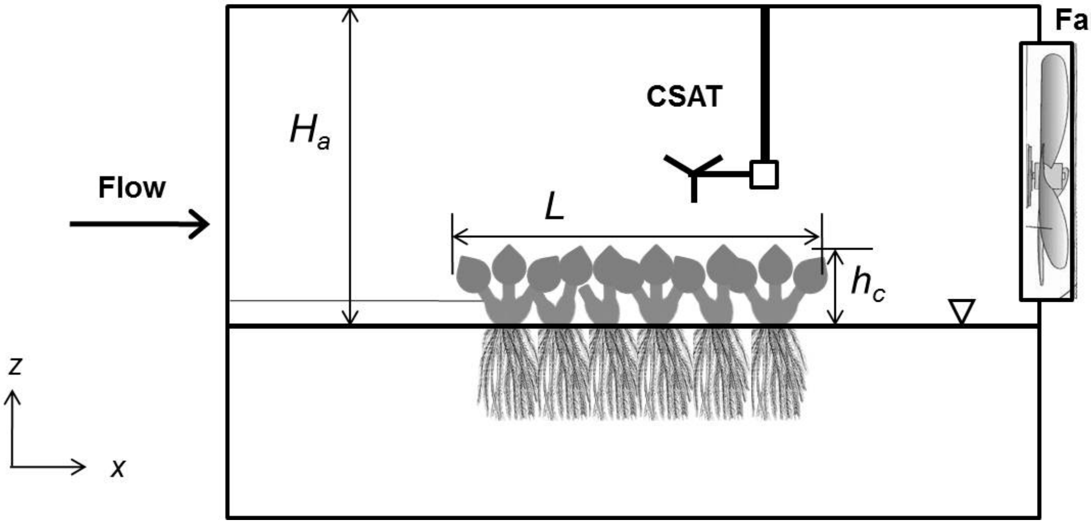

Figure 4.1: Schematic of experimental setup for air velocity measurements in semi-enclosed wind tunnel with attached water basin. Velocity was measured using a sonic anemometer (CSAT) around stationary floating leaf canopies of length L and height h_c. Air flow (depth H_a) was induced by an outward-blowing fan mounted at the downwind end of the wind tunnel. Water surface is denoted by ∇. Not to scale.

4.2.3 Velocity Measurements

Three-dimensional orthogonal wind velocities (u, v, w) and virtual temperature (T) were measured using an ultrasonic anemometer (CSAT, Campbell Scientific, Inc., Logan, UT, USA). The CSAT uses three pairs of non-orthogonally oriented transducers that transmit and receive ultrasonic signals. The travel time of the ultrasonic signal is directly related to the wind velocity along the transducer axis; the speed of sound is directly related to the air density (i.e., temperature and humidity). The pathlength between transducers was 0.10 m. The CSAT was mounted to an aluminum rod projecting from the ceiling of the wind tunnel; the instrument was oriented horizontally to both minimize transducer shadowing effects and measure as close to the leaf canopy as possible (Figure 4.2). The sampling volume of the CSAT was located

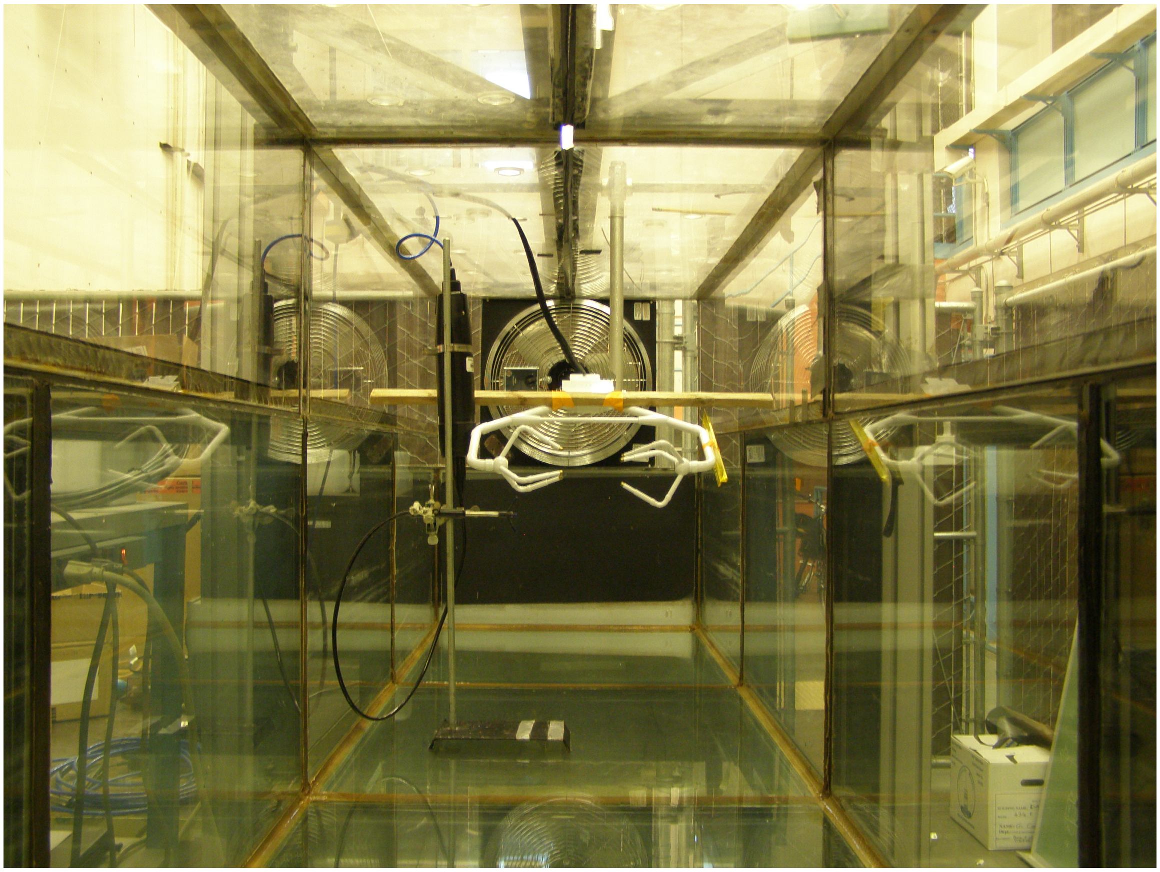

Figure 4.2: Photograph of wind tunnel, taken looking downwind with an empty water basin. Outward-blowing fan is seen at far end of photograph; also seen are the sonic anemometer (CSAT, white instrument in center) and an acoustic Doppler velocimeter (ADV, near left wall mounted on stand). During data collection, ADV position was 4.3 cm below the water surface and was used to determine the magnitude of wind-induced water velocity (described in Chapter 2.2.3).

7.5 cm to the right (looking downwind) of the wind tunnel centerline. The coordinate system is as follows: primary flow direction, x, with $x = 0$ and $x = L$ at the upwind and downwind edges of canopy, respectively; cross-wind direction, y, with $y = 0$ at the left side of the wind tunnel (looking downwind); and vertical direction, z, with $z = 0$ at the water surface and $z = H_a$ at the ceiling (Figure 4.1). The corresponding velocity vector components are $\mathbf{u}(x, y, z) = u, v, w$.

As in water experiments, flow field structure was constructed from point measurements of velocity using two-dimensional linear interpolation, under the assumption of steady flow. For Leaf Canopies 1 and 2, vertical velocity profiles consisting of $5 - 8$

Figure 4.3: Photograph showing vegetation raft floating in wind tunnel, taken looking downwind. Outward-blowing fan is seen at far end of photograph and sonic anemometer is seen near top of photo.

measurements were taken at eight positions along the length of the raft, plus two upwind and three downwind locations, for a total of 13 profiles and 71 point measurement locations (denoted by + in Figures 4.4-4.5). For Leaf Canopy 3, a transect of velocity was taken at a height of z = 14.3 cm above the water surface to compare to that of Leaf Canopies 1 and 2. Because of the relatively small size of the wind tunnel, and the fixed position of the anemometer, velocity measurements were collected at one point in space within the wind tunnel. To measure the flow field around the leaf canopies, the raft was moved relative to the anemometer by changing the attachment point of the spectra line extending from the raft to the upwind end of the wind tunnel. Upon completion of velocity measurements at each horizontal position, the canopy was repositioned and the flow field was allowed to equilibrate for five minutes prior to subsequent measurements. Velocity records were collected for four minutes at a sampling frequency of 30 Hz. Due to the configuration of the CSAT probes, velocity could only be measured within 1 cm of the top of the leaf canopy. Velocity measurements were taken outside the ceiling boundary layer, based on preliminary wind tunnel characterization.

4.2.4 Data Analysis

Data were evaluated to ensure velocity records were not contaminated by leaf interference or otherwise compromised; compromised records were evidenced by the presence of both non-physical velocity values (spikes) and missed data blocks. To ensure high-quality velocity data, I checked that individual velocity components were within three standard deviations of the mean value for each record. Data not meeting this criteria were removed and replaced by data linearly interpolated from near neighbors. Because replacement of data in this way can lead to bias, only records for which fewer than 10% of points were replaced are included in the results. This resulted in elimination of one record (out of 71) for the Leaf Canopy 1 flow field and two (out of 71) for the Leaf Canopy 2 flow field.

The velocity statistics were computed as follows: for each velocity record, mean velocity components (U, V, W) were determined using a running mean filter with a window length of 10 seconds. The fluctuating velocity components (u', v', w') were calculated by subtracting each mean velocity component from that of instantaneous velocity (u, v, w),

$$\begin{aligned} u' &= u - U \\ v' &= v - V \\ w' &= w - W \end{aligned} \tag{4.1}$$

Similarly for temperature (T), mean temperature $\left(\overline{T}\right)$ was computed as the average of the record, and fluctuating temperature (T') was calculated by subtracting the mean temperature from the instantaneous temperature, $T' = T - \overline{T}$. Vertical gradients of mean temperature $(d\overline{T}/dz)$ were approximated using finite differencing with a first-order upwind scheme.

Reynolds stress for each record was computed as the average of the product of the x- and z-fluctuating velocities, $\overline{u'w'}$. The mixing efficiency, r_{uw}, was computed according to Equation (3.13). Turbulent kinetic energy (q^2) was computed for each record as

$$q^2 = 0.5\left(\overline{u'^2} + \overline{v'^2} + \overline{w'^2}\right) \tag{4.2}$$

Turbulence intensity (TI) was computed as the ratio of standard deviation to mean value of streamwise velocity at each height,

$$TI = \frac{\sigma_u(z)}{U(z)} * 100 \tag{4.3}$$

The presence of density stratification affects the turbulent flow structure. To check whether stratification effects were present, I computed the Monin-Obukhov length (L_M),

$$L_M = -\frac{u_*^3}{\kappa \alpha g \overline{w'T'}}, \tag{4.4}$$

where u_* is the friction velocity, κ is the von Karman constant, α is the coefficient of thermal expansion, g is gravitational acceleration, and $\overline{w'T'}$ is the heat flux (*Kundu and Cohen* 2004). Friction velocity was defined as $u_* = (\overline{u'w'})^{0.5}$ at $z = 3.6$ cm above the water surface, 15 cm upwind of the raft; this location was selected because $\overline{u'w'}$ varied little with height upwind of the raft. Physically, L_M represents the height at which the buoyant destruction of turbulence is balanced by shear production of turbulence. Comparing the height z to L_M becomes a form of the flux Richardson number, which is the ratio of buoyant destruction of turbulent kinetic energy to the shear production,

$$Rf = \frac{z}{L_M} \tag{4.5}$$

For $Rf > 1$, buoyant forces destroy turbulence faster than it is generated by shear production. For stable or neutral conditions (as expected in this experiment), the effects of stratification on the turbulence are considered small for small values of Rf (i.e., $z \ll L_M$) (*Kundu and Cohen* 2004).

For comparison of flow fields between leaf and root canopies, velocity magnitude ($||U||$) was computed as the sum of the squared instantaneous velocity components, averaged over the record,

$$||U|| = \frac{1}{n} \sum_{i=0}^{n} \sqrt{u_i^2 + v_i^2 + w_i^2}, \tag{4.6}$$

where n is the number of measurements in each record.

4.3 Results and Discussion

4.3.1 Mean Flow Structure

The presence of the leaf canopy in the flow altered the mean flow structure. In all experiments, flow was diverted around the leaf canopy, causing increased velocities in the flow above (Figures 4.4-4.6). The streamwise velocity (U) continuously accelerated beginning at the upwind end of the canopy ($x/L = 0$), until a distance around $x/L = 0.5$ (Figures 4.4A-4.6A & 4.7). The cross-wind velocity (V) was small for all experiments, with a magnitude less than 10% of the mean streamwise velocity; however the direction of V was not consistent among the canopies, suggesting secondary circulation (Figures 4.4B-4.6B). The flow diversion began slightly upwind of the leaf canopy, where the mean vertical velocity (W) increased in magnitude with an upward direction (Figures 4.4C-4.6C).

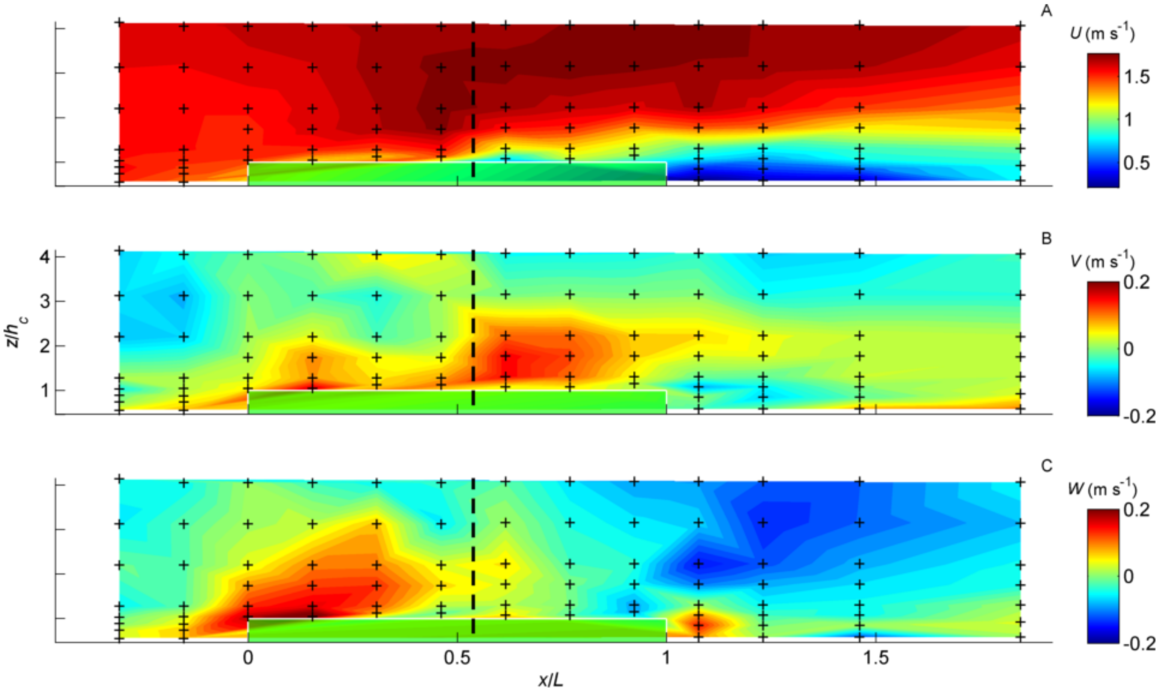

Figure 4.4: Contour plots of mean flow structure around Leaf Canopy 1 (green shaded region outlined in white), based on discrete velocity measurements (denoted by +) near raft centerline. (A) mean streamwise (x) velocity, U; (B) mean cross-wind (y) velocity, V; and (C) mean vertical (z) velocity, W. Leaf canopy extends vertically upward from water surface to $z/h_c = 1$ and horizontally from $x/L = 0$ to $x/L = 1$. Wind tunnel ceiling is located at $z/h_c = 8.2$ (not shown). Dark dashed line near $x/L = 0.5$ denotes break in measurements of 19 hours.

For Leaf Canopy 1, a break in measurements of 19 hours occurred at the mid-length of the canopy. During this break, a cold front passed, causing a decrease in the ambient air temperature in the laboratory. It is expected that the effects of this temperature change did not strongly impact the mean velocity structure; however, the turbulent velocity structure may be contaminated. These results are included here for completeness, but must be interpreted with caution. Data for Leaf Canopies 2 and 3 were collected without interruption. However, given the large number of samples collected for Leaf Canopy 2, data collection spanned 10 hours. In contrast, data collection for Leaf Canopy 3 spanned only one hour.

For Leaf Canopy 2 the spatial development of the velocity structure is further visualized by inspection of mean streamwise velocity profiles (Figure 4.7). Here, five

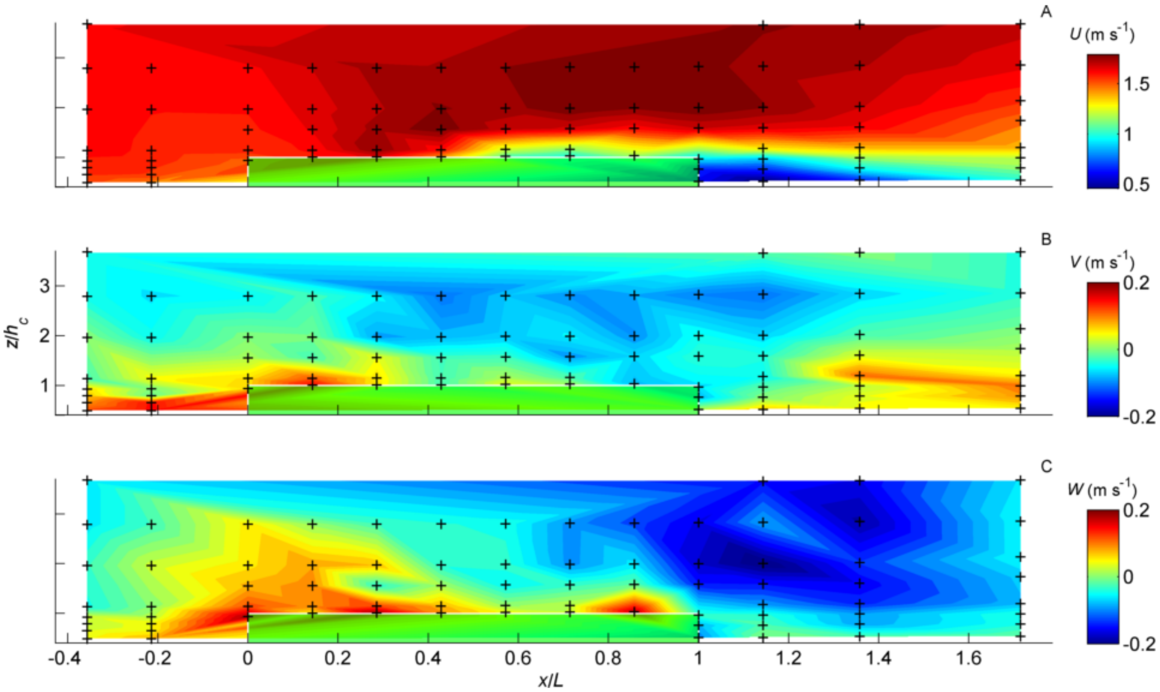

Figure 4.5: Contour plots of mean flow structure around Leaf Canopy 2 (green shaded region outlined in white), based on discrete velocity measurements (denoted by +) near raft centerline. (A) mean streamwise (x) velocity, U; (B) mean cross-wind (y) velocity, V; and (C) mean vertical (z) velocity, W. Leaf canopy extends vertically upward from water surface to $z/h_c = 1$ and horizontally from $x/L = 0$ to $x/L = 1$. Wind tunnel ceiling is located at $z/h_c = 7.3$ (not shown).

distinct regions of the flow, as described by *Belcher et al.* (2003), are evident: upwind conditions at $x/L = -0.4$, characterized by a logarithmic velocity profile; an impact region just upwind of the canopy $x/L = 0$, where U is reduced from upwind conditions for heights $z/h_c < 3$; an adjustment region between $0 < x/L < 0.6$, where U decreases near the leaf canopy surface and increases above; a roughness change region between $0.6 \leq x/L \leq 1.1$, where the velocity profile is fully developed $\left(\frac{\partial U}{\partial x} \approx 0\right)$ and has adjusted to the roughness change induced by the leaf canopy; and a wake region for $x/L > 1.1$, where the velocity profile transitions back to its logarithmic form (though a complete transition is not observed here). The exit region as described by *Belcher et al.* (2003) was not clearly evident in these data; it is expected to occur between the downwind edge of the canopy and one canopy height downwind (i.e., $1 < x/L \leq 1.1$ for Leaf Canopy 2). In this experiment, the velocity profile at $x/L = 1.1$ strongly resembles that of the fully-developed region (Figure 4.7).

Although velocity was not measured within the canopy, there was evidence of

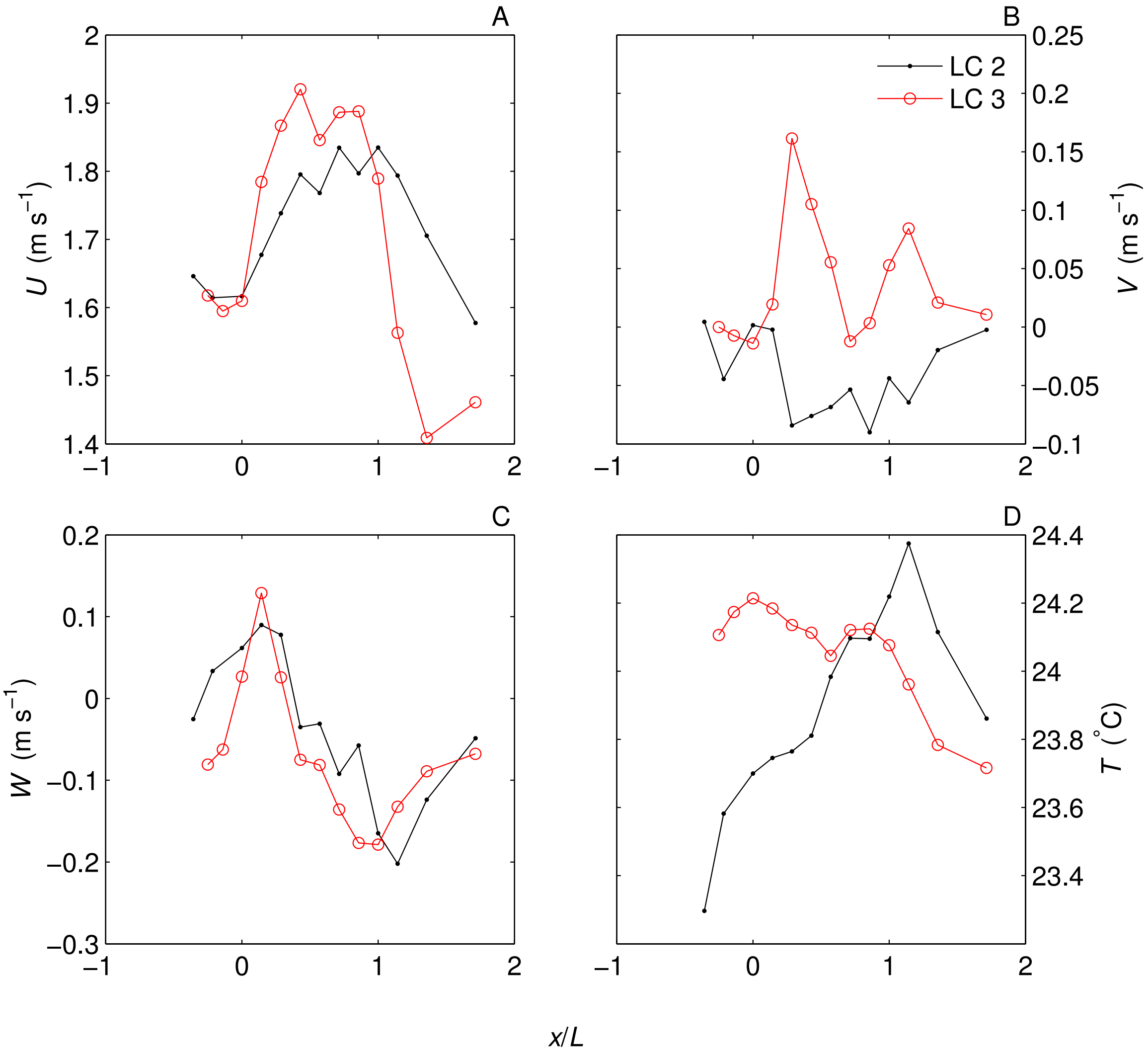

Figure 4.6: Horizontal transects of mean values of (A) streamwise velocity (U), (B) cross-wind velocity (V), (C) vertical velocity (W), and (D) temperature $\left(\overline{T}\right)$ for Leaf Canopies 2 & 3 (LC 2 and LC 3, respectively). Leaf canopy extends from $x/L = 0$ at the upwind edge to $x/L = 1$ at the downwind edge.

inflectional mean velocity profiles in Leaf Canopy 2 beyond 60% of canopy length, suggesting mixing layer development (Figure 4.7). Velocity profiles downwind of the canopy ($x/L > 1$) deviated from logarithmic upwind conditions, signaling a loss of fluid momentum (Figure 4.7).

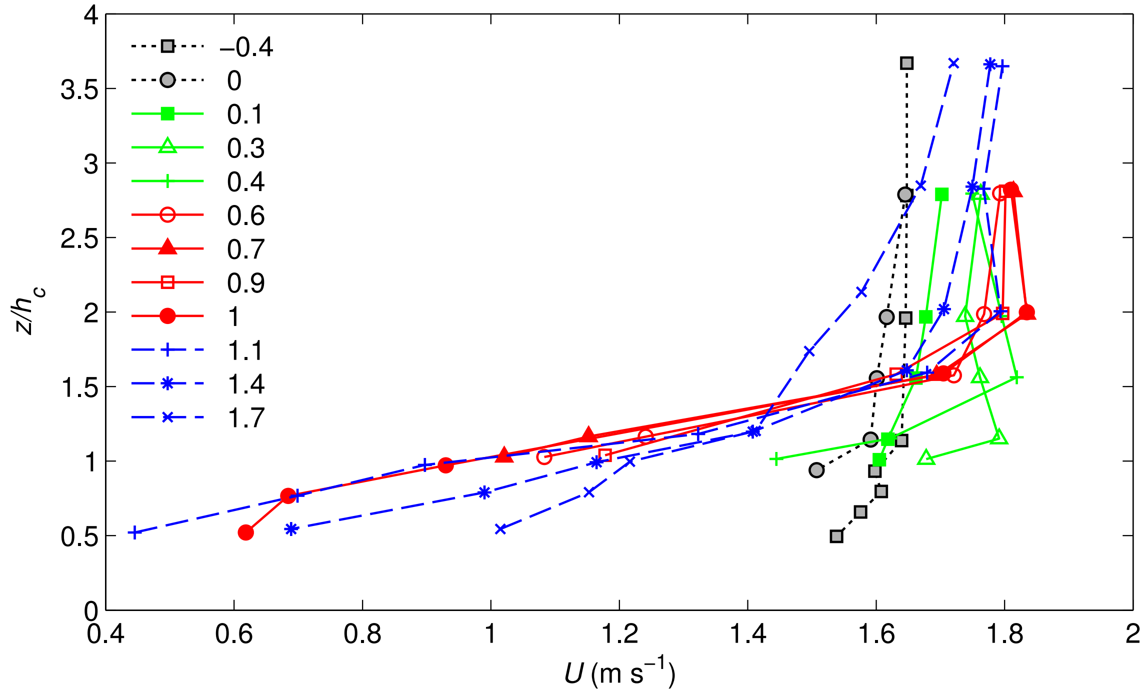

Figure 4.7: Flow development along the channel shown by vertical profiles of streamwise velocity ($U(z)$) for different $x-$locations, extracted from the Leaf Canopy 2 flow field of Figure 4.5A. Locations in x are normalized by raft length (L); vertical heights are normalized by leaf canopy height (h_c). Gray symbols with short-dashed lines denote upwind locations ($x/L < 0$), green symbols denote developing-flow region above canopy ($0 \leq x/L < 0.6$), red symbols denote fully-developed flow region above canopy ($0.6 \leq x/L \leq 1$), and blue symbols with long-dashed lines denote downwind locations ($x/L > 1$). Velocity profile approaches fully-developed near $x/L \approx 0.6$.

4.3.2 Turbulent Flow Structure

The leaf canopy also altered the turbulent flow structure by generating turbulence via two mechanisms: turbulent shear generation along the canopy-air interface and wake generation downwind of the canopy. Turbulent shear generation was observed at the canopy-air interface for Leaf Canopies 1 and 2 as increased Reynolds stress $\left(\overline{u'w'}\right)$ and turbulent kinetic energy (q^2) beginning near 50% of the canopy length (Figures 4.8-4.9). Both Reynolds stress and turbulent kinetic energy were elevated outside and downwind of the leaf canopies (Figures 4.8B-4.9B). Downwind of the canopies, these elevated turbulence levels signal the development of a wake region of recirculating flow (Figures 4.8, 4.9, & 4.10A,B). This wake region suggests flow separation at the downwind end and the presence of form drag.

Using elevated Reynolds stress as a surrogate for the presence of a boundary layer at the canopy-air interface, it appears the boundary layer was larger for Leaf Canopy 1 than Leaf Canopy 2 despite its smaller canopy height (Table 4.1). In addition, the size of the high-turbulence region downwind of the canopy was larger for Leaf Canopy 1 than for Leaf Canopy 2; peak values of Reynolds stress and turbulent kinetic energy were approximately equal between the canopies (Figures 4.8-4.9). As mentioned above, the break in sampling for Leaf Canopy 1 and subsequent change in atmospheric conditions may have played a role in these observations. Increased turbulence levels above Leaf Canopy 3 were not observed at the transect height ($z =$ 14.3 cm; $z/h_c = 1.9$), suggesting the boundary layer did not extend to this height (Figure 4.10A). However, larger values of Reynolds stress and turbulent kinetic energy were observed downwind of Leaf Canopy 3 than for Leaf Canopy 2, likely caused by the longer length of Leaf Canopy 3, as explained in Section 4.3.4 (Figure 4.10A).

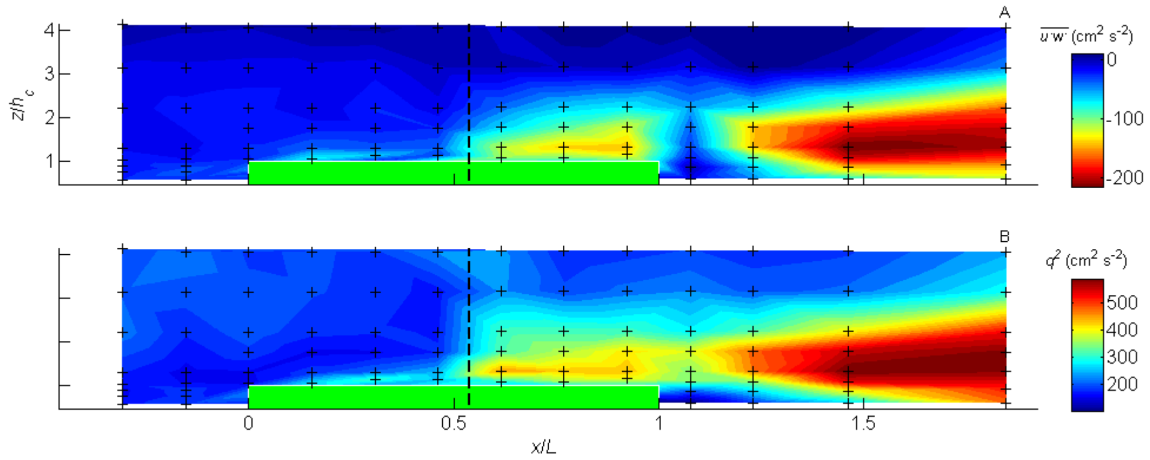

Figure 4.8: Contour plots of turbulent flow structure around Leaf Canopy 1 (green shaded region). (A) Reynolds stress $\left(\overline{u'w'}\right)$, and (B) turbulent kinetic energy (q^2). Dark dashed line near $x/L = 0.5$ denotes break in measurements of 19 hours. Other axis scaling and symbols as for Figure 4.4.

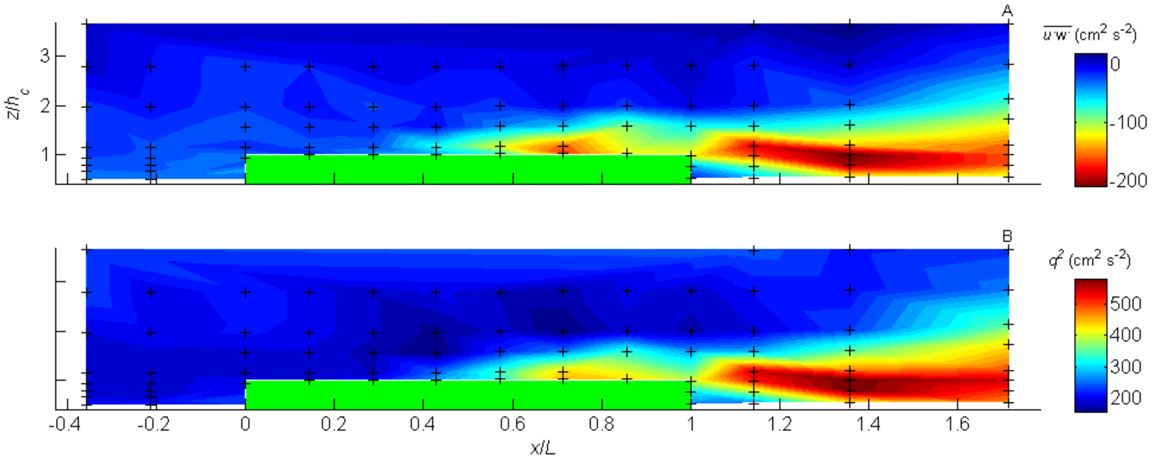

Figure 4.9: Contour plots of turbulent flow structure around Leaf Canopy 2 (green shaded region). (A) Reynolds stress $\left(\overline{u'w'}\right)$, and (B) turbulent kinetic energy (q^2). Axis scaling and symbols as for Figure 4.5.

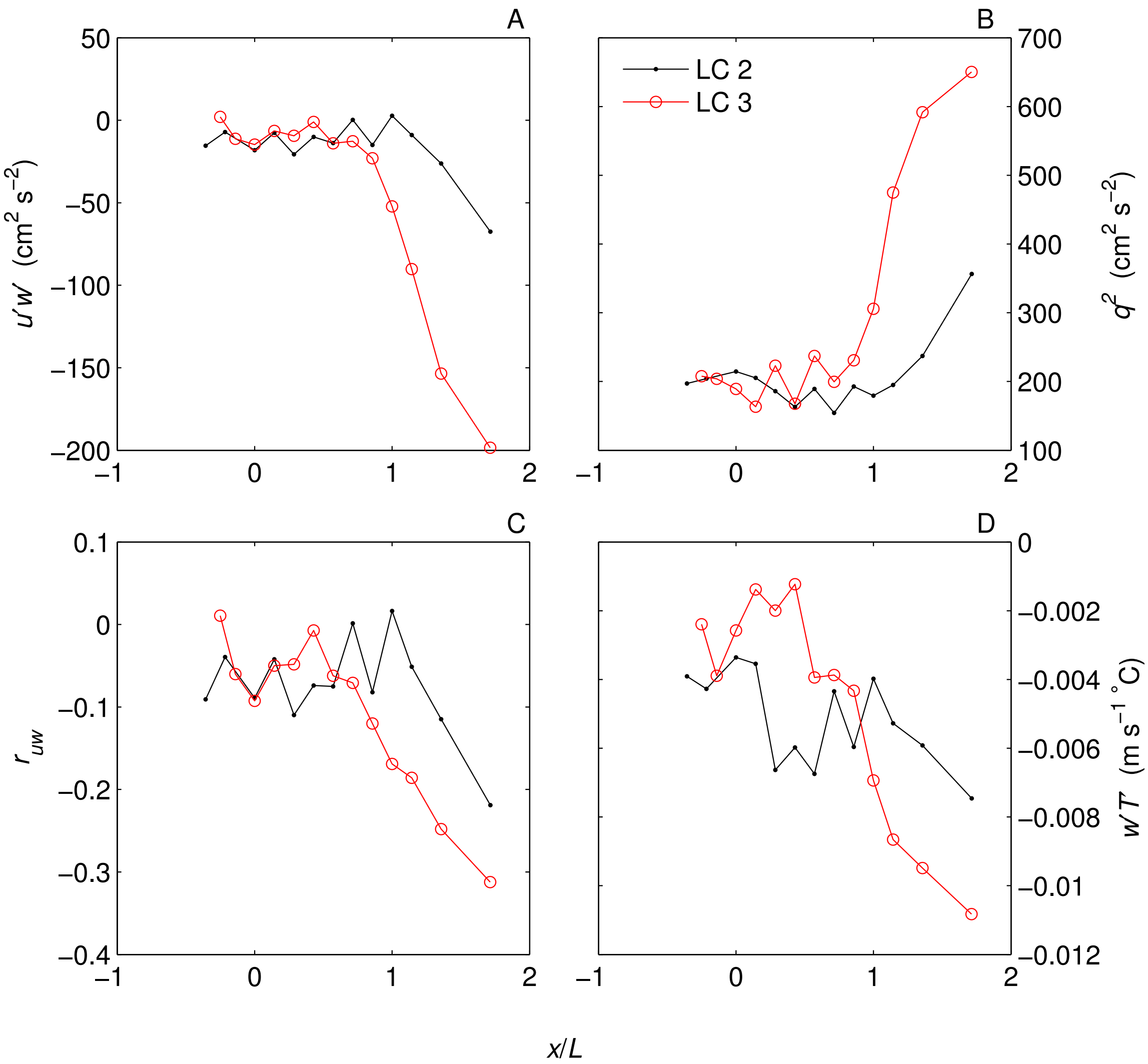

Figure 4.10: Horizontal transects of (A) Reynolds stress $\left(\overline{u'w'}\right)$, (B) turbulent kinetic energy (q^2), (C) mixing efficiency (r_{uw}), and (D) turbulent heat flux $\left(\overline{w'T'}\right)$ for Leaf Canopies 2 & 3 (LC 2 and LC 3, respectively). Leaf canopy extends from $x/L = 0$ at the upwind edge to $x/L = 1$ at the downwind edge.

4.3.3 Temperature and Stratification

As explained above, the decrease in air temperature that occurred during a break in measurements affected the mean temperature field for Leaf Canopy 1, with higher temperatures for the first half of the canopy than for the last half. Despite this change, the vertical gradient of mean temperature was generally positive (i.e., temperature increases with height) and low in magnitude (Figure 4.11A). For Leaf Canopy 1, the highest vertical gradient of mean temperature occurred in the lee of the leaf canopy, coincident with low magnitudes of both Reynolds stress (Figure 4.8A) and turbulent heat flux (Figure 4.11B).

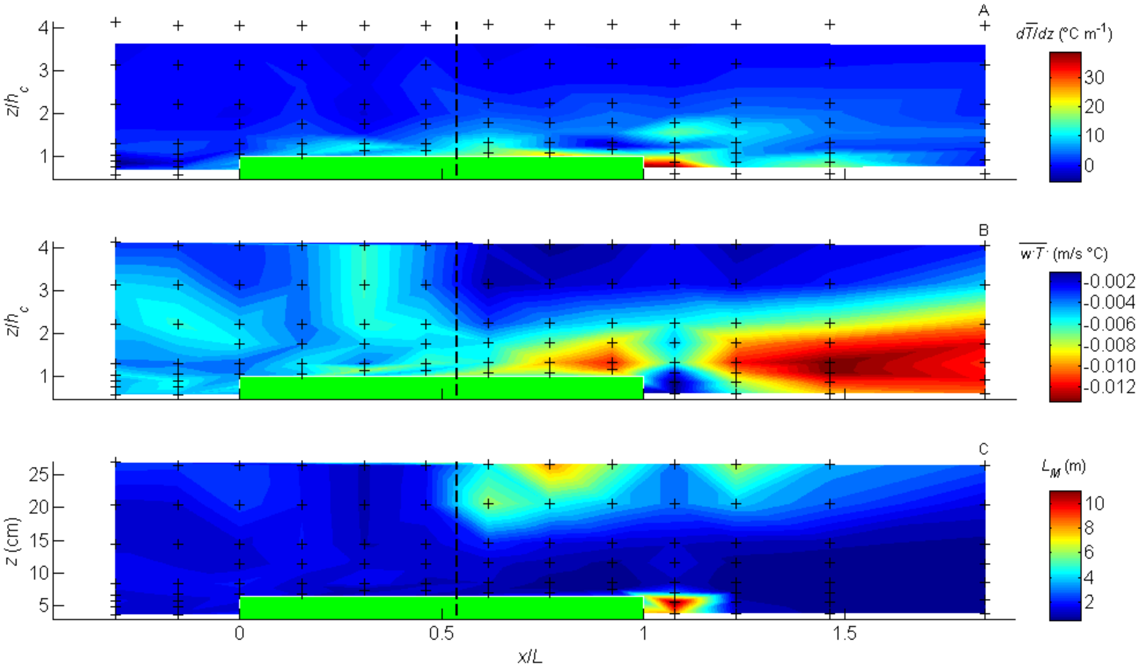

Figure 4.11: Contour plots of (A) mean air temperature gradient ($d\overline{T}/dz$), (B) turbulent heat flux $\left(\overline{w'T'}\right)$, and (C) Monin-Obukhov length (L_M) for Leaf Canopy 1 (green shaded region). Variables in (A) and (B) are plotted against height normalized by leaf canopy height; variable in (C) is plotted against absolute height. Dark dashed line near $x/L = 0.5$ denotes break in measurements of 19 hours. Other axis scaling and symbols as for Figure 4.4.

For Leaf Canopy 2, the vertical temperature gradient was of similar magnitude to Leaf Canopy 1 (Figure 4.12A). In contrast to Leaf Canopy 1, the highest vertical gradient of mean temperature occurred above the leaf canopy at 75% of canopy length, coincident with high magnitudes of both Reynolds stress (Figure 4.9A) and turbulent heat flux (Figure 4.12B). This disparity suggests the region downwind of Leaf Canopy 1 was colder than that of Leaf Canopy 2, and the region near 75% of canopy length of Leaf Canopy 2 was colder than that of Leaf Canopy 1. For the transect of Leaf Canopy 3, vertical temperature gradients were not recorded. However, comparing values of mean temperature near $z = 14.3$ cm for Leaf Canopies 2 and 3 demonstrates spatial variations (Figure 4.6D). Despite the short duration of data collection for Leaf Canopy 3, temperature varied 0.5°C along the transect, which was about half of that observed for Leaf Canopy 2 (Figure 4.6D). This suggests that spatial variations in temperature were intrinsic to the flow structure.

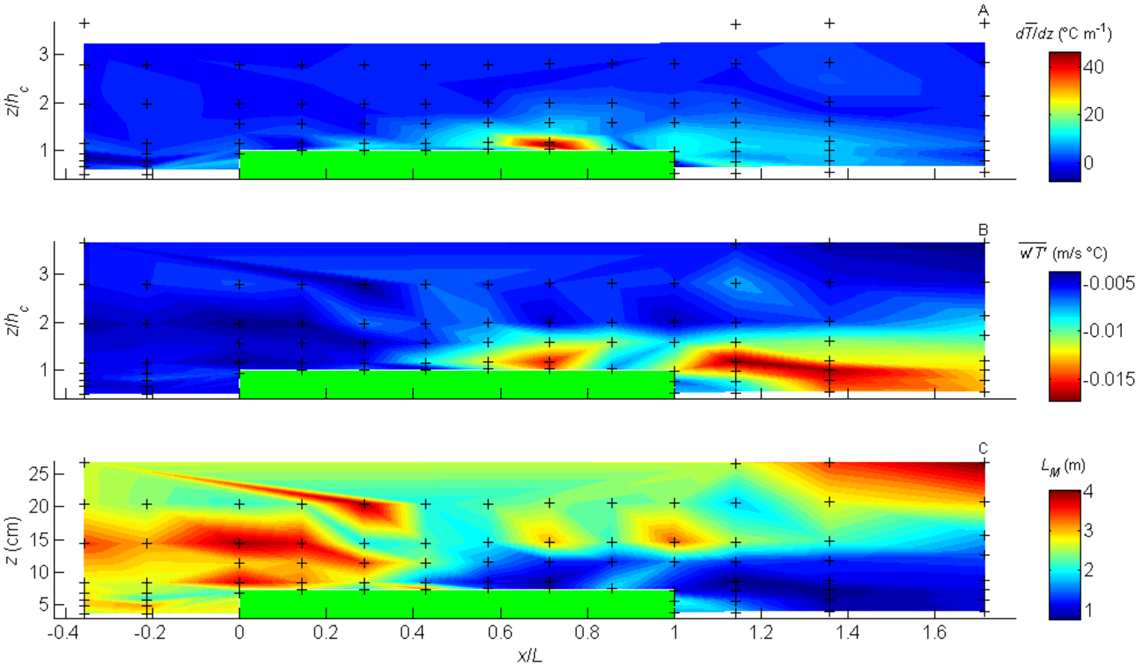

Figure 4.12: Contour plots of (A) mean air temperature gradient ($d\overline{T}/dz$), (B) turbulent heat flux $\left(\overline{w'T'}\right)$, and (C) Monin-Obukhov length (L_M) for Leaf Canopy 2 (green shaded region). Variables in (A) and (B) are plotted against height normalized by leaf canopy height; variable in (C) is plotted against absolute height. Other axis scaling and symbols as for Figure 4.5.

The turbulent heat flux for Leaf Canopies 1 and 2 was generally small and negative, increasing with distance along the canopy (Figures 4.11B-4.12B). Heat flux magnitude was greatest beyond the downwind edge for $x/L > 1.2$, suggesting net transport of heat downward (Figures 4.11B-4.12B). For Leaf Canopy 2, the heat flux was elevated above upwind conditions above the canopy only for heights within one canopy height (i.e., $z/h_c < 2$ for $0 \leq x/L \leq 1$, Figure 4.12B).

For Leaf Canopy 3, the heat flux was smaller in magnitude along the first half of the canopy than for Leaf Canopy 2; downwind of the canopy, heat flux magnitude was greater for Leaf Canopy 3 than for Leaf Canopy 2 (Figure 4.10D). The sign on heat flux depends on the stability of the atmosphere; it is positive (upward heat flux) for unstable environments and negative (downward heat flux) for stable environments (*Kundu and Cohen* 2004). Based on these results, I expect the air density profile was stable throughout data collection. As observed for Reynolds stress and turbulent kinetic energy, the size of the region of elevated turbulent heat flux in Leaf Canopy 1 was greater than that for Leaf Canopy 2 (Figures 4.11B-4.12B).

The structure of the Monin-Obukhov length (L_M) varied spatially for Leaf Canopies 1 and 2, but in both cases z was much smaller than L_M, (i.e., the flux Richardson number was small), meaning the effects of stratification are negligible (Figures 4.11C-4.12C). This means the flow above the leaf canopy was a forced convection region and the turbulence was mechanically forced (*Kundu and Cohen* 2004).

4.3.4 Effect of Canopy Length

To assess the effect of leaf canopy length on the flow development, the velocity transect at $z = 14.4$ cm for Leaf Canopy 2 was compared to that at $z = 14.3$ cm for Leaf Canopy 3. Leaf Canopy 1 was not included in this comparison because of the change in atmospheric conditions during the break in sampling.

The structure of U and W was similar for these two canopy lengths, but variations in V were observed (Figure 4.6A-C). For the shorter canopy length, the increase in U beyond the upwind canopy edge required a greater distance to reach fully-developed conditions, the magnitude of the fully-developed U was lower, and the decrease in U beyond the downwind edge occurred over a greater distance (Figure 4.6A). The structure of W was more similar between the two canopy lengths, with a positive peak at the upwind edge and a negative peak at the downwind edge (Figure 4.6C). The structure of V between the two canopy lengths was similar in magnitude but opposite in sign (Figure 4.6B). This may be caused by the different canopies having different surface structures, inducing minor secondary circulation.

The spatial development of velocity standard deviations was different for these two canopy lengths; the longer canopy (Leaf Canopy 3) had generally higher standard deviations for all velocity components, particularly beyond the downwind edge of the canopy (Figure 4.13A-C). This suggests greater effects on the flow for longer canopies, which we would expect to manifest as increased turbulence. This expectation is indeed observed; turbulence intensity, Reynolds stress, and turbulent kinetic energy were all higher for the downwind regions of the longer canopy (Figures 4.10A,B & 4.13D). There was roughly a two-fold increase in these three turbulence parameters downwind of the longer canopy. As expected considering these observations, the mixing efficiency was higher for the longer canopy length in the turbulent wake region downwind (Figure 4.10C).

One limitation of this study is the lack of multiple sampling locations in the crosswind (y) direction, meaning secondary circulation was not readily identified in this experimental setup. Although the measured mean y-velocity was within 10% of the upwind streamwise air velocity, the flow fields and velocity transect for leaf canopies demonstrated different directions of V (Figures 4.4B-4.6B). This suggests the presence of secondary circulation in the wind tunnel. However, the Leaf Canopies 1 and 2 had qualitatively similar mean (U and W) and turbulent flow fields, suggesting secondary circulation did not significantly impact the flow structure. Another limitation was the inability to sample velocity within the leaf canopy, which prohibited observation of any inflection points in mean streamwise velocity profiles. However, the velocity profile at the downwind edge of Leaf Canopy 2 contained an inflection point ($x/L = 1$, Figure 4.7), so it is reasonable to assume the other velocity profiles within the fully-developed region also contained inflection points.

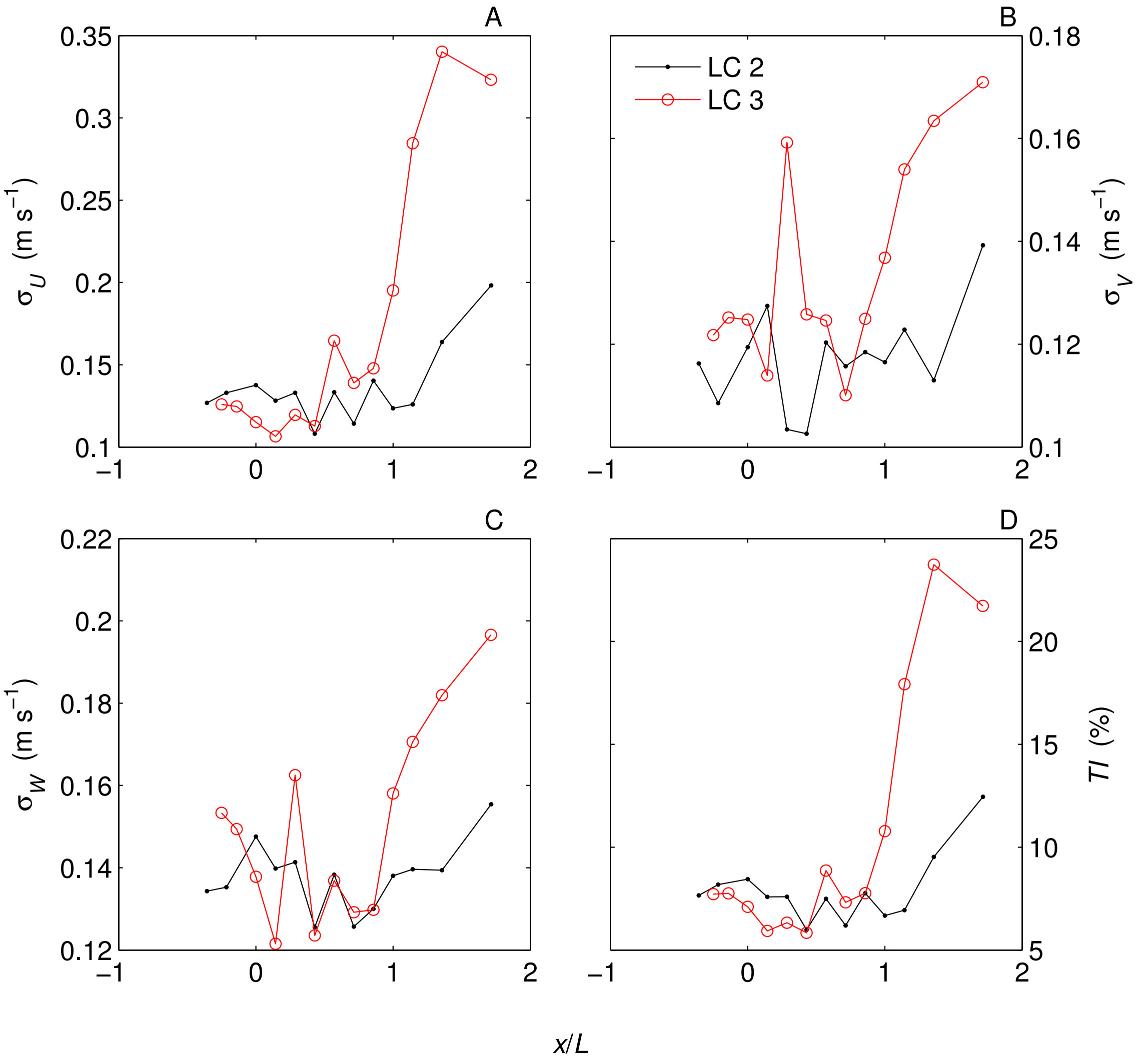

Figure 4.13: Horizontal transects of standard deviations of (A) streamwise velocity (σ_u), (B) cross-wind velocity (σ_v) and (C) vertical velocity (σ_w); horizontal transect of (D) turbulence intensity (TI) for Leaf Canopies 2 & 3 (LC 2 and LC 3, respectively). Leaf canopy extends from $x/L = 0$ at the upwind edge to $x/L = 1$ at the downwind edge.

4.3.5 Comparison of Flow Fields in Air and Water

There were similarities in the mean and turbulent velocity structure between air and water. In the mean velocity structure, a low-velocity wake region of similar normalized magnitude developed at the downstream end of the raft in both fluids (Figure 4.14). In water, this wake region extended further downstream; this may be caused by the greater acceleration of flow underneath the root canopy (Figure 4.14B).

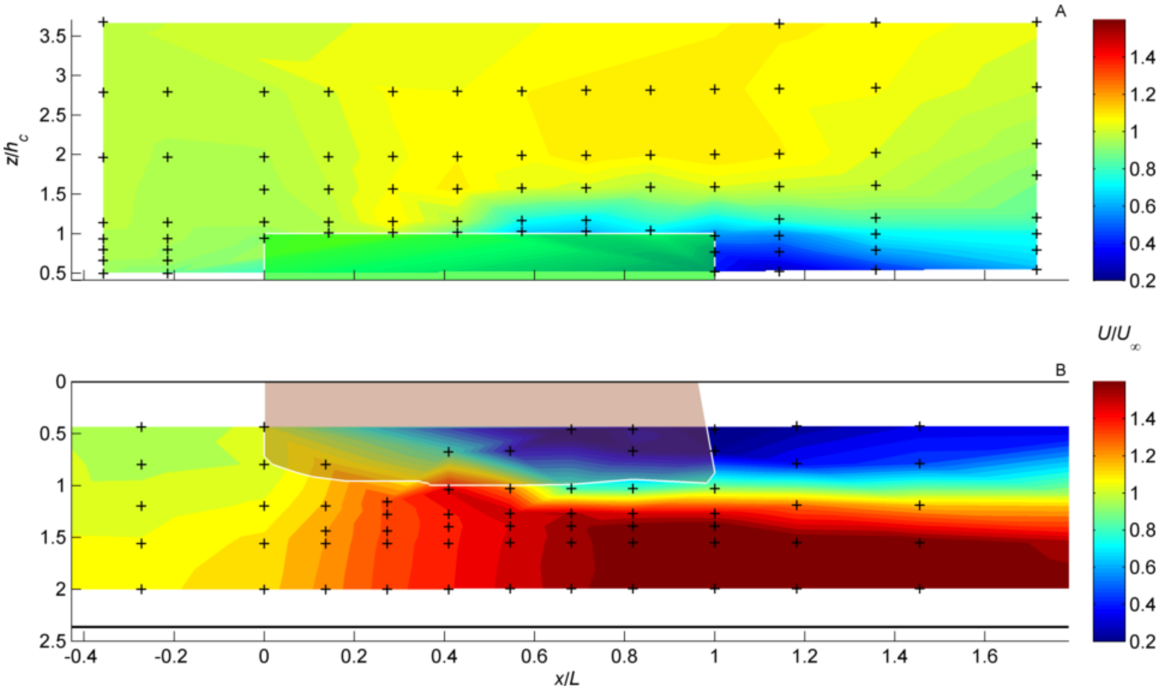

Figure 4.14: Comparison of normalized velocity magnitude ($||U||/U_\infty$) structure for leaf and root canopies: (A) Leaf Canopy 2 (green shaded region outlined in white), and (B) Root Canopy 1 (shaded region outlined in white), based on discrete velocity measurements (denoted by $+$) near raft centerline. Leaf and root canopies extend vertically from water surface ($z/h_c = 0$) to $z/h_c = 1$ and horizontally from $x/L = 0$ to $x/L = 1$. Wind tunnel ceiling is located at $z/h_c = 7.3$ (not shown); flume bed is denoted by thick dark line near $z/h_c = 2.5$. Not to scale.

In the turbulent velocity structure, greater effects were observed for the root canopy than for the leaf canopy. The highest normalized Reynolds stresses were observed downstream of the raft in both fluids (Figure 4.15). In air, the region of elevated Reynolds stress began earlier along the raft than in water ($x/L \approx 0.4$ in air vs. ≈ 0.55 in water) (Figure 4.15). In water, the magnitude of the highest normalized Reynolds stress was about three times that in air, with a location further downstream (Figure 4.15). However, comparing the relative change in normalized Reynolds stresses between water and air reveals a greater difference: in water, the increase over upstream conditions was 10 times that observed in air. The ratio of average upstream to maximum downstream normalized Reynolds stress in water was 145 while in air it was only 15. This suggests a larger-intensity wake region develops in the lee of root canopies. Elevated turbulence intensity (TI) was observed downstream of the raft in both fluids (Figure 4.16). The upstream TI was approximately equal in both flows. The root canopy had a greater effect on TI than the leaf canopy; the region of elevated TI extended further downstream in water than in air with a magnitude nearly 1.5 times greater (Figure 4.16B). It is interesting to compare the fields of normalized Reynolds stress and turbulence intensity: immediately downstream of both canopies was a region of very-low Reynolds stress with similar magnitude to upstream conditions; however the turbulence intensity in this same region was elevated. In water, the TI in this region was close to the maximum value observed.

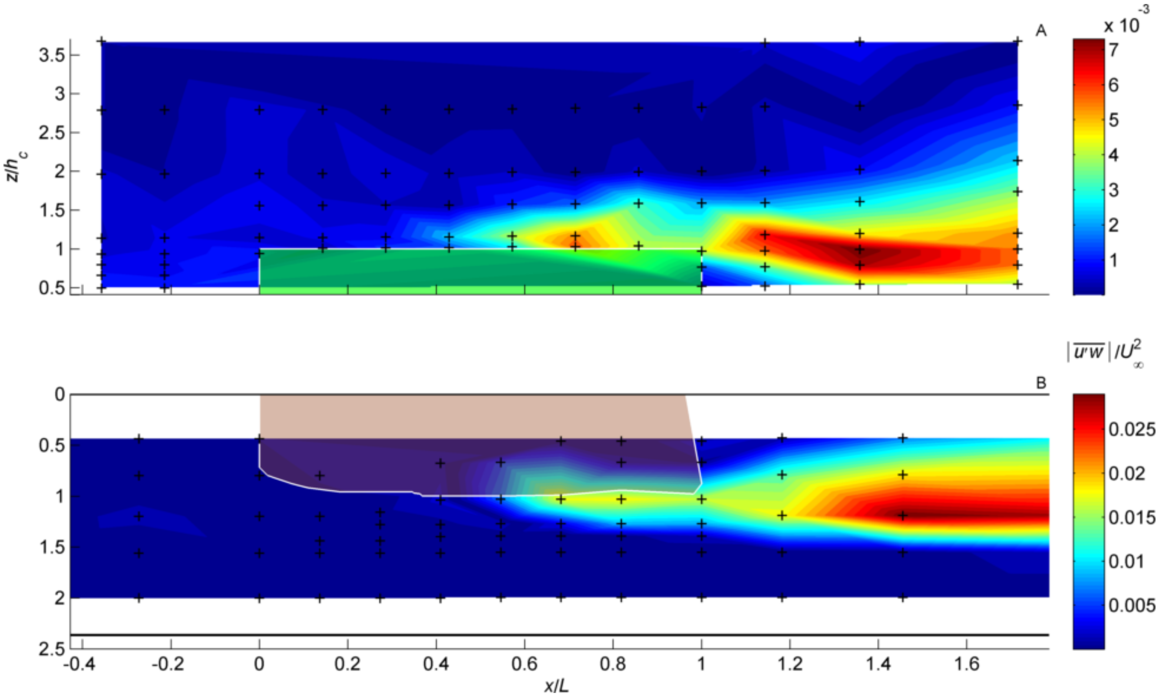

Figure 4.15: Comparison of normalized Reynolds stress ($\left|\overline{u'w'}\right|/U_\infty^2$) structure for leaf and root canopies: (A) Leaf Canopy 2 (green shaded region outlined in white), and (B) Root Canopy 1 (shaded region outlined in white). Absolute value of Reynolds stress is shown; Reynolds stress is negative everywhere for leaf canopies and positive for root canopy-water interactions (see Chapter 3.3.2 for explanation). Axis scaling and symbols as for Figure 4.14. Note the colorbar limits are not equal. Not to scale.

These results suggest the fluid-dynamic effects of the root canopy exceed those of the leaf canopy. This is expected considering the denser structure of the root canopy compared to that of the leaf canopy (Figures 1.1, 1.2, & 2.5), leading to greater drag imparted on the root canopy (as observed in Chapter 2). This greater drag causes the root canopy to behave closer to a bluff body, which is characterized by diversion of flow around the body and generation of a wake region downstream. Additionally, free-floating macrophytes are found in relatively small-scale water environments, with a much smaller scale than the atmospheric flows. Considering these smaller scales of the water environments, the hydrodynamic effects become more important.

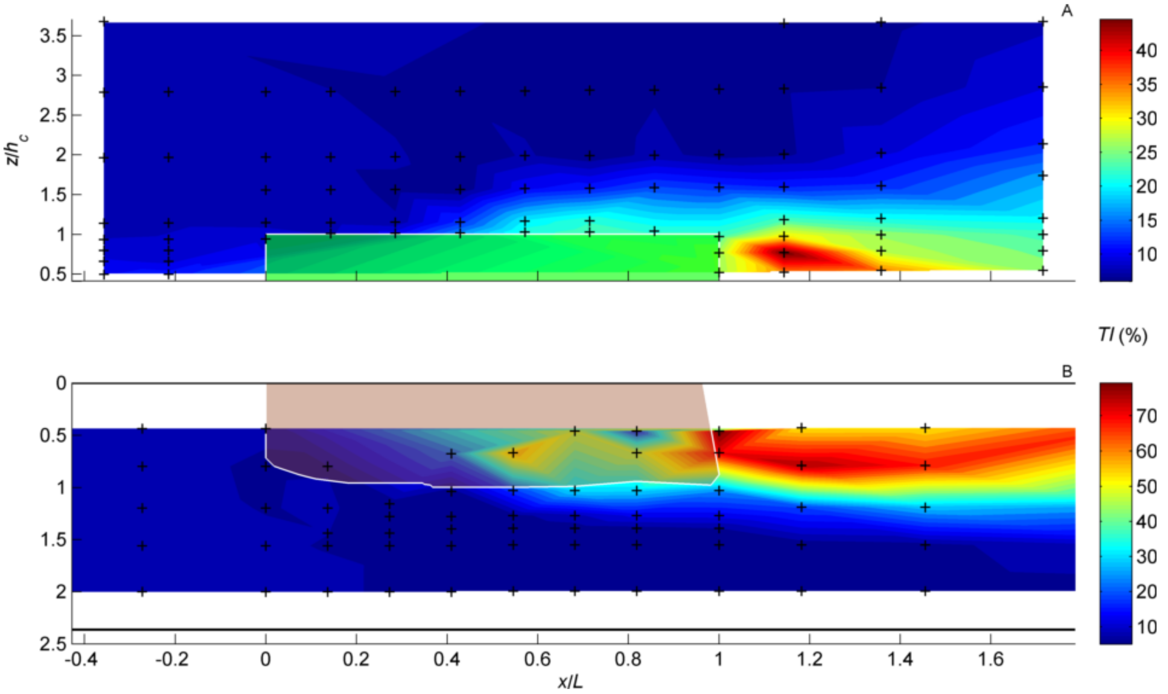

Figure 4.16: Comparison of turbulence intensity $\left(TI = \frac{\sigma_u(z)}{U(z)} * 100\right)$ structure for leaf and root canopies: (A) Leaf Canopy 2 (green shaded region outlined in white), and (B) Root Canopy 1 (shaded region outlined in white). Axis scaling and symbols as for Figure 4.14. Note the colorbar limits are not equal. Not to scale.

4.4 Summary

Laboratory experiments were performed in a wind tunnel to observe the aerodynamic effects of *E. crassipes* leaf canopies. Under steady flow, the velocity structure around two leaf canopies was measured using a sonic anemometer. For a third canopy, a velocity transect was obtained at one height above the canopy; these data were used to compare the effects of canopy length on the flow dynamics.

Results indicate that the presence of the leaf canopy in the flow altered the mean and turbulent velocity structure. Flow was diverted around the leaf canopy and turbulence was generated at the canopy-air interface. The spatial development of the mean streamwise velocity profile generally agreed with a model of flow adjustment developed for terrestrial vegetation canopies; four of the five regions of adjustment were observed. Observations of heat flux and Monin-Obukhov length demonstrated that stable, unstratified conditions were present during data collection. As leaf canopy length increased, turbulence intensity, Reynolds stress, and turbulent kinetic energy increased, particularly in the downwind wake region.

Flow fields in air and water were measured for one particular raft to facilitate comparison of the fluid-dynamic effects between these fluids. A low-velocity wake region of similar normalized magnitude developed at the downstream end of both leaf and root canopies; in water there was greater acceleration of the flow outside the canopy and the wake region extended further downstream. Comparing the turbulent flow structures, the normalized Reynolds stress induced by the root canopy was three times that of the leaf canopy. The change in Reynolds stress between upstream and downstream regions was one order of magnitude greater for the root canopy than for the leaf canopy, signifying the development of a larger-intensity wake region in water. Turbulence intensities in the downstream wake region were 1.5 times greater in water than in air. These results suggest the fluid-dynamic effects of the root canopy exceed those of the leaf canopy.

Chapter 5

Environmental Transport of Free-Floating Macrophytes in a Tidal Channel

In this chapter I present field observations of free-floating macrophyte raft transport in a tidal system, where a raft responds to both wind and water forcing. These observations are compared to the laboratory results of Chapter 2 to test the hypothesis that water currents are the primary transport mechanism for free-floating macrophyte rafts.

5.1 Background

The Sacramento River-San Joaquin River Delta (Delta) is a network of intersecting channels formed by the confluence of the Sacramento and San Joaquin Rivers (Figure 5.1). Water currents in the Delta are forced by the flows of these rivers and by tides propagating upstream from the Pacific Ocean via San Francisco Bay. The Delta is of great importance to California; it provides water for irrigation and human consumption, it provides navigation channels for the shipping industry, it provides facilities for human recreation, and it provides habitat for numerous aquatic and terrestrial species.

The native flora and fauna of the Delta are increasingly threatened by invasive species. These invasive species compromise the native ecosystem and negatively affect commercial, recreational, and agricultural activities. *E. crassipes* is but one example of an invasive species affecting the Delta. In the Delta, *E. crassipes* is found in sloughs, flooded islands, connecting waterways, and tributary rivers. Some of the problems created by *E. crassipes* in the Delta include: blocking canals and waterways, closing marinas, fouling irrigation pumps, displacing native plants, reducing dissolved oxygen in the water, and depositing silt and organic matter more rapidly (*California Department of Boating and Waterways* 2004). *E. crassipes* modifies its environment by changing the functional characteristics of an ecosystem. For example, in a study of the functional roles of *E. crassipes* compared to a native free-floating macrophyte (pennywort, *Hydrocotyle umbellata* L.) in the Delta, *Toft et al.* (2003) found that native invertebrates, an important part of native fish diets, were more likely to establish in the native species of free-floating macrophyte.

The growth of *E. crassipes* in the Delta is difficult to control. This species was first introduced to the Sacramento River in 1904 by ornamental pond enthusiasts (*Toft et al.* 2003). By 1981, almost 25% of Delta waterways were covered by *E. crassipes* (*Greenfield et al.* 2006). The growth of *E. crassipes* in the Delta has been controlled by three primary methods: mechanical harvesting, chemical control through herbicide application, and biological control using host-specific natural enemies (*Pieterse and Murphy* 1990). There are significant costs associated with each method, in terms of both money and ecosystem impacts. Additionally, each method varies in effectiveness; for example, mechanical harvesting is generally considered cost-effective only for small areas and for species that have ineffective regional dispersal mechanisms (*Pimentel et al.* 2000). Currently, *E. crassipes* growth is controlled by a large-scale chemical control program operated by the California Department of Boating and Waterways using the chemical 2,4-D (*Greenfield et al.* 2006). However, recent legal decisions may soon require permitting through the National Pollution Discharge Elimination System (NPDES) under the U. S. Environmental Protection Agency (*Greenfield et al.* 2006). The associated paperwork and monitoring costs of NPDES permitting may make nonchemical control methods more cost-effective.

There is a continuing need to improve the efficiency of control methods for invasive macrophytes, particularly since the annual cost of these invasions exceeds $100 million in the U.S. alone (*Pimentel et al.* 2000). Greater understanding of regional dispersal can significantly improve the efficiency of these methods, as explained previously (Chapter 2.1.1). Toward this end, I observed free-floating macrophyte raft transport in the environment.

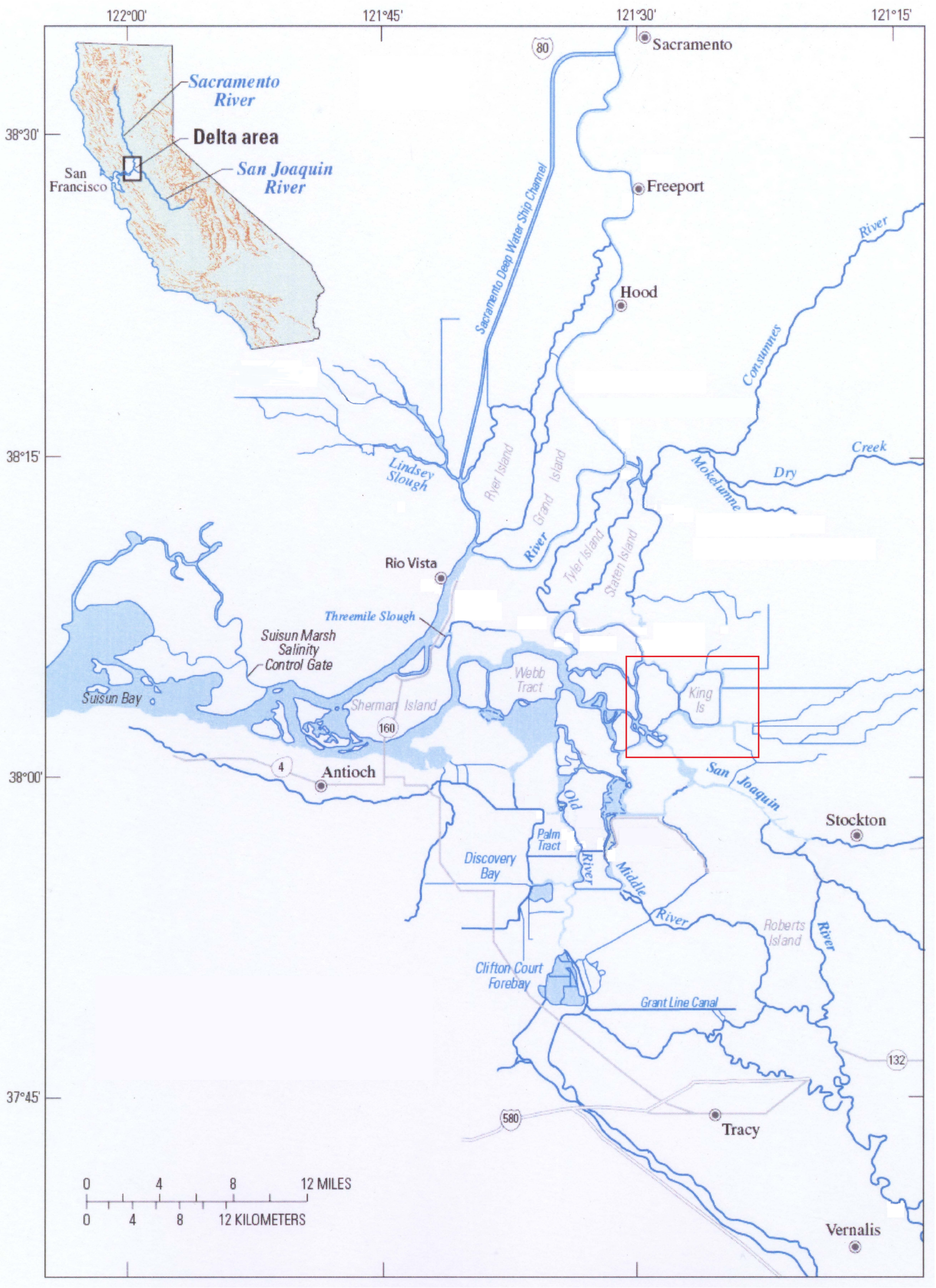

Figure 5.1: Overview map of Sacramento River-San Joaquin River Delta, located in central California. Red box outlines map area shown in Figure 5.2.

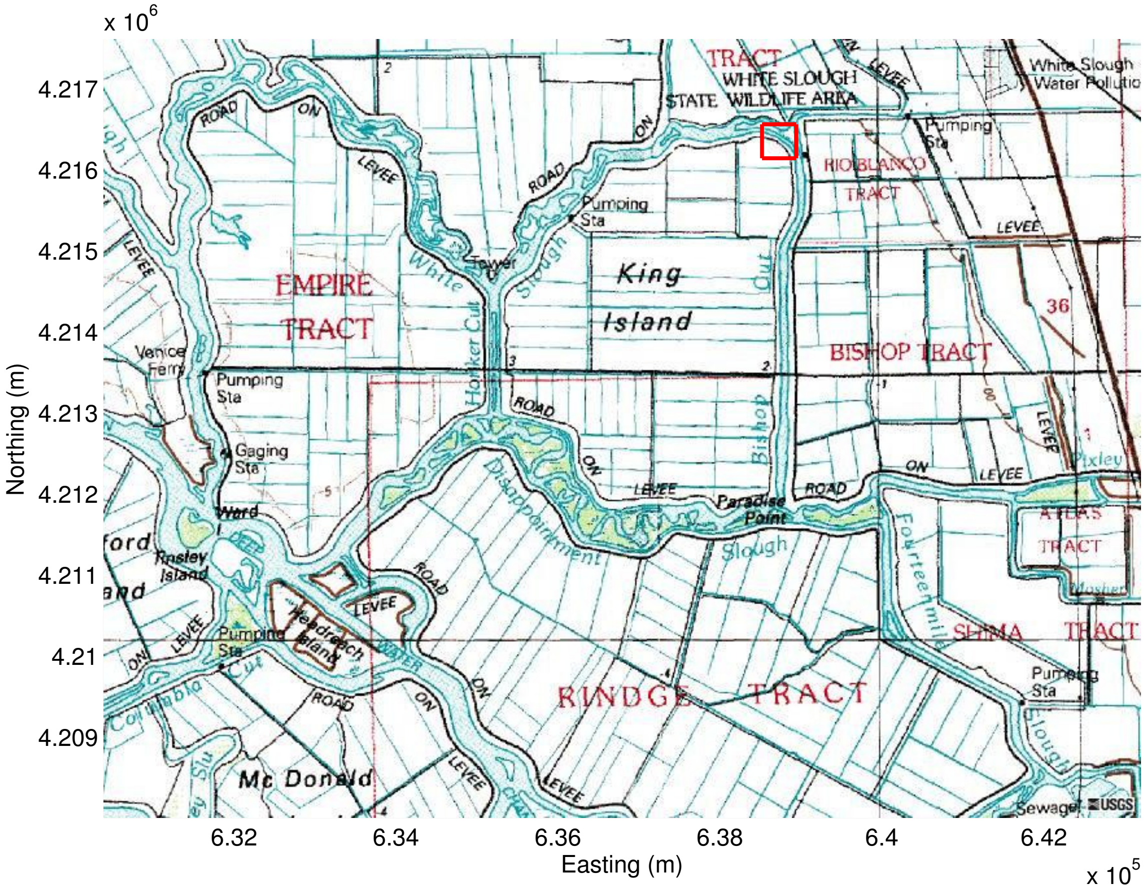

Figure 5.2: Overview map of field site, located at junction of White Slough and Bishop Cut in Delta. Red box in upper right outlines map area shown in Figure 5.11.

5.2 Materials and Methods

5.2.1 Field Site

This experiment was conducted at the intersection of White Slough and Bishop Cut adjacent to King Island and Bishop Tract near Stockton, CA. White Slough is oriented east-west and Bishop Cut is oriented north-south (Figure 5.2). The water currents in this region change direction depending on the tidal phase; on ebb (falling) tides, flow heads north through Bishop Cut and west through White Slough, reversing on flood (rising) tides. This field site allowed for changing water velocity direction which, when observed under steady winds, allowed direct comparison of the relative influence of wind and water forcing for free-floating macrophyte raft transport.

5.2.2 Instrumentation

Vegetation Raft

The instruments used in this experiment were an acoustic Doppler velocimeter (ADV) (Vector, NortekUSA, Annapolis, MD, USA) and a global positioning system (GPS) receiver. The ADV measures velocity magnitude and direction using the Doppler shift of acoustic energy reflected by material suspended in the water column. The ADV produces water velocity magnitude and direction at a single point located 15.7 cm below the transducer head. In this experiment, the ADV sampling volume was located at a depth of 0.43 m below the water surface. The sampling frequency of the ADV was 64 Hz and data were recorded continuously during the experiment. The GPS receiver was part of a drifting sensor developed by the Lagrangian Sensor Systems Laboratory in the Department of Civil and Environmental Engineering at UC-Berkeley. This sensor was originally developed for the purpose of gathering Lagrangian flow data in shallow water environments. The GPS receiver used was a Magellan AC-12 module with a circular error probability of 1.5 m (*Tinka et al.* 2010). The sampling frequency of the GPS receiver was 1 Hz; data were recorded continuously during the experiments.

The instruments were mounted on a polyvinyl chloride (PVC) frame constructed for this experiment. The frame measured 1 m square and was constructed of 1 1/4 in (3.18 cm) PVC pipe joined with PVC cement to create a water-tight seal; this seal trapped air inside, making the frame buoyant. The frame dimensions were selected to provide enough buoyancy to compensate for the weight of the ADV and GPS units. Both the ADV and the GPS were attached to the PVC frame using pipe clamps (Figure 5.3). The ADV transducer head was mounted 27 cm below the water surface.

When equipped with instrumentation, the frame floated with 0.5 inches of exposed tubing.

The PVC frame was embedded within a vegetation raft formed by *H. umbellata*; the root canopy length measured 0.3 m and the leaf canopy height measured 0.2 m. This species was chosen because it is the predominant native free-floating macrophyte in the Delta and because it was present near the field site. Both *H. umbellata* and *E. crassipes* form free-floating canopies and occupy similar habitats (*Toft et al.* 2003). The primary differences between *H. umbellata* and *E. crassipes* lie in their physical structures; *H. umbellata* has greater leaf densities and lower root surface areas than *E. crassipes*. These differences suggest that *H. umbellata* may be more affected by wind forcing than *E. crassipes*. Throughout the experiment, the PVC frame with vegetation remained in the water. When necessary, the frame was pulled to the center of the channel and released for subsequent measurements.

During initial deployment, I performed a qualitative study of the effect of the PVC frame and instrumentation on the movement of the raft. I observed the transport of a natural raft and the instrumented raft in Bishop Cut (north of Telephone Cut) during ebb tide, when water velocity direction was south to north (along primary axis of channel) and wind velocity was west to east (perpendicular to primary axis of channel) (Figure 5.2). Both rafts were one square meter in surface area and were released at the same longitudinal location along the channel, from a location near the center of the channel. Initially, the rafts were separated laterally by two feet. During three 30-minute observation periods, the rafts traveled downstream in water at the same rate, but diverged from their initial lateral spacing (Figure 5.4). When the wind velocity was less than 5 mph (2.2 m s^{-1}), the rafts traveled downwind in air at the same rate. However, when the wind velocity increased to 8 mph (3.6 m s^{-1}), the instrumented raft traveled downwind faster than the natural raft. I determined that the instrumented raft was affected by the wind slightly more than the natural raft, but both were equally affected by the water velocity.

Environmental Conditions

Wind speed was measured by an aerovane anemometer (Model 05106, RM Young) that I installed on a levee located 1 km from the study site at a height 2.5 m above the water (Figure 5.5). An aerovane anemometer is a mechanical velocimeter that combines a propeller and a tail on the same axis to record wind velocity and direction accurately. The anemometer measured wind velocity and direction every minute; data were recorded to a datalogger (CR200, Campbell Scientific). Wind data were smoothed using a 15-minute running mean filter.

Local water velocity was measured on the boat using an acoustic Doppler current

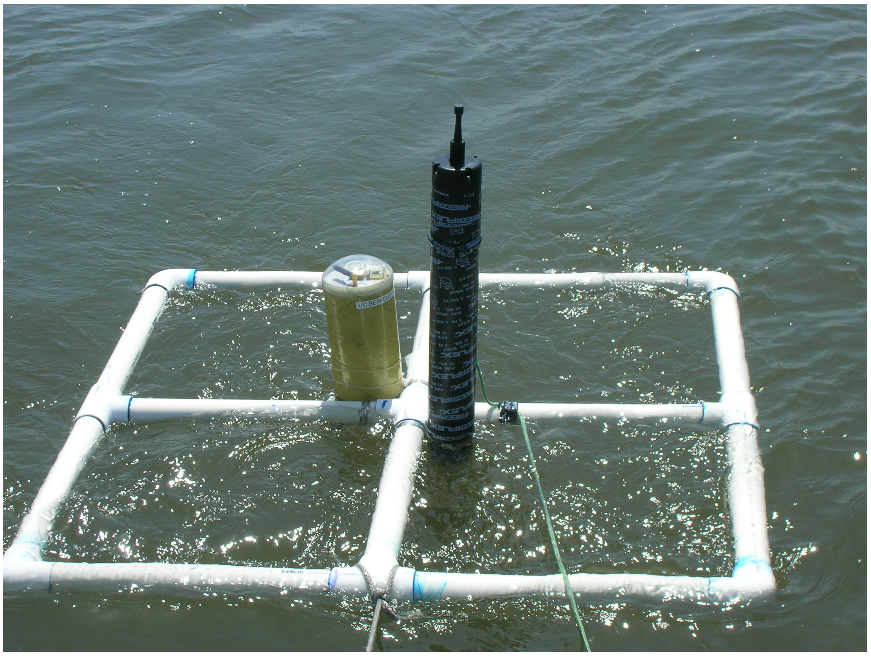

Figure 5.3: Photograph of PVC frame showing GPS (left) and ADV (right) instrumentation.

Figure 5.4: Photograph of instrumented raft (left) and natural raft (right) comparison during field experiment on August 1, 2008. Photograph taken looking north along the Bishop Cut. The western bank of the channel is visible on the left of the photograph.

Figure 5.5: Photograph of anemometer setup for field experiment on August 1, 2008. Aerovane is shown mounted on upper left of frame and datalogger is shown mounted on center post. Photograph taken looking west across Bishop Cut.

profiler (ADCP) (1200 kHz Workhorse Monitor, RD Instruments). Like the ADV, the ADCP also measures velocity magnitude and direction using the Doppler shift of acoustic energy reflected by material suspended in the water column. Unlike the ADV, which measures velocity at a single point, the ADCP produces vertical profiles of velocity magnitude and direction. In this experiment, the ADCP was mounted to a moving boat; the ADCP was deployed in bottom track mode to separate the velocity of the boat from that of the water column. For Cases B and C, the instrument was programmed in high-resolution mode. The ADCP was mounted on a pole just off the starboard side of the boat; the transducer head was positioned 0.1 m below the water surface (Figure 5.6). Velocity measurements were separated by 0.25 m in the vertical direction (bin size), beginning 0.7 m below the transducer head (blanking distance).

5.2.3 Data Analysis

The velocity measured by the ADV was the water velocity relative to the vegetation raft ($\mathbf{U}_{rel}$) at the sampling volume (0.43 m below the water surface). Vector components of relative water velocity in x and y were output in east-north-up (ENU) coordinates. ENU output is corrected for instrument orientation using data from the internal compass and the pitch and roll sensors, thereby providing velocity direction relative to magnetic north. Correcting for magnetic declination (14.517° E, source: NOAA National Geophysical Data Center, 8/1/2008) provides velocity direction relative to true north. ADV data were smoothed using a 10-second running mean filter and downsampled to 1 Hz to match the GPS sampling frequency.

The GPS receiver output raft position in Universal Transverse Mercator (UTM) coordinates at 1 Hz. In UTM coordinates, a position on Earth is referenced by a UTM zone and an easting and northing coordinate pair. UTM coordinates are convenient because position is reported in meters, which greatly simplifies calculations of velocity. Raft velocity ($\mathbf{U}_{raft}$) was computed as $d\mathbf{x}/dt$, where $\mathbf{x}$ is the position vector of the raft, determined from the northing and easting coordinate pair. Raft velocity was computed using finite differencing with a first-order upwind scheme. The GPS data had several gaps of less than 15 seconds; these gaps in the record were filled using linear interpolation. Raft velocity was smoothed using a 10-second running mean filter.

Combining these two data streams, I computed the water velocity vector ($\mathbf{U}_{water}$) at 1 Hz at the sampling volume below the raft as

$$\mathbf{U}_{water} = \mathbf{U}_{raft} + \mathbf{U}_{rel} \tag{5.1}$$

Velocity magnitude ($||\mathbf{U}||$) was computed for the raft and water velocity vectors as

$$||\mathbf{U}|| = \sqrt{U^2 + V^2}, \tag{5.2}$$

Figure 5.6: Photograph of ADCP setup for field experiment on August 1, 2008. The instrument was mounted at mid-length of the boat, off the starboard gunnel; the transducer head was deployed facing downward, toward the channel bed. During data collection, the transducer head was positioned 0.1 m below the water surface.

where U and V are the x- and y-components of velocity, respectively. The coordinate system is defined such that positive x velocity points east and positive y velocity points north.

5.3 Results and Discussion

5.3.1 Environmental Conditions

I observed raft trajectories over three phases of a tidal cycle: ebb tide, slack tide, and flood tide (Table 5.1 and Figure 5.7). Winds were consistent in magnitude (2-3 m s^{-1}) and direction (westerly) during the experiments (Figure 5.8). These conditions allowed for changing water velocity magnitude and direction during a period of steady winds.

Table 5.1: Flow conditions for field experiment on August 1, 2008.

Case	Tidal Phase	Wind Direction
A	Ebb	Due west
B	Slack	Due west
C	Flood	Due west

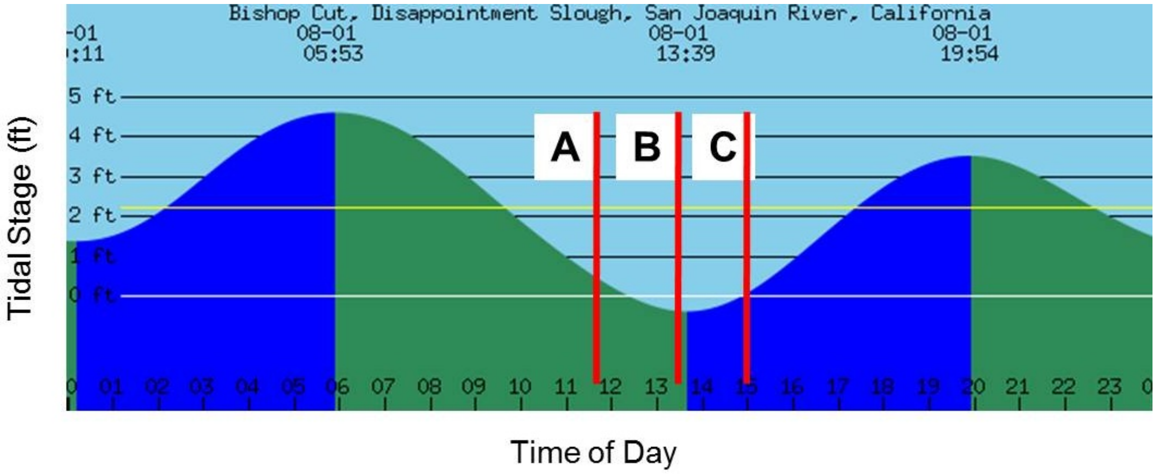

Figure 5.7: Tidal stage and timing (denoted by red vertical lines) of drifting experiments on August 1, 2008. Cases are specified in Table 5.1.

Channel velocities as measured by the ADCP varied over the tidal cycle. Three channel surveys were conducted to measure flow velocity at a cross section near the

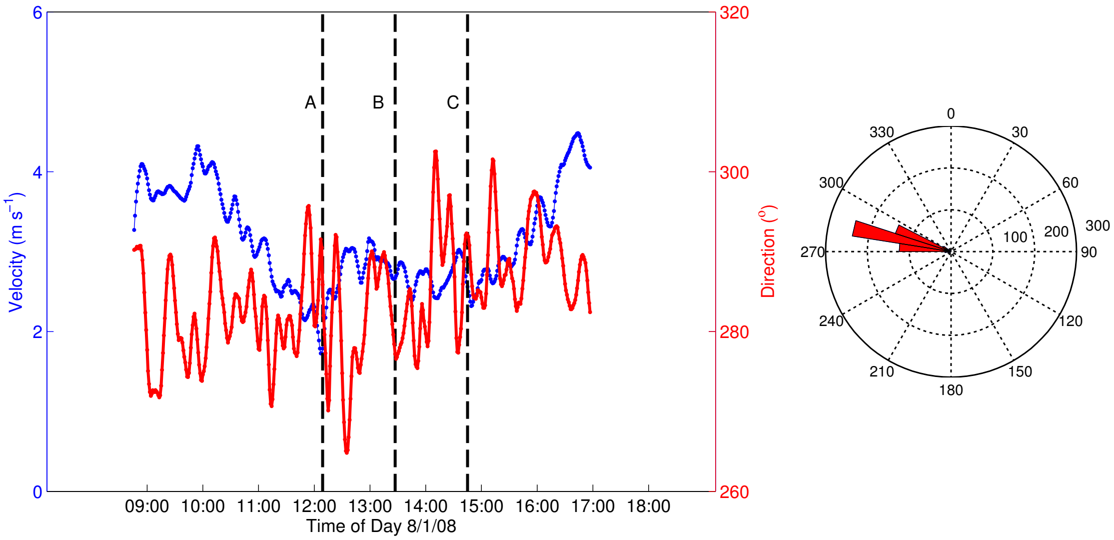

Figure 5.8: Time series of wind magnitude and direction for field experiment on August 1, 2008. Wind direction histogram (right) demonstrates that westerly winds dominated throughout the day. Timing of cases are delineated by dashed vertical lines (A, B, C, Table 5.1).

location of the raft. These surveys coincided with the three tidal phases studied here (Table 5.1). During each survey, the channel was traversed from south shore to north shore. The channel was approximately 50 m wide and the channel transect lasted 1-2 min. During ebb tide (transect time 12:09-12:11), the channel velocity peaked at 120 cm s^{-1} (Figure 5.9A). The direction of the flow was approximately aligned with the primary axis of the channel, which was 300° relative to true north (Figure 5.10A). Just before slack tide (transect time 13:27-13:28), the channel velocity reduced to 70 cm s^{-1} and the velocity direction was northerly (Figures 5.9B & 5.10B). Finally, on the flood tide (transect time 14:45-14:46), the channel velocity increased to almost 200 cm s^{-1}, with a direction approximately 180° opposite that of the ebb tide, again aligned with the primary axis of the channel (Figures 5.9C & 5.10C). These water velocity magnitudes were noticeably larger than those recorded by the instrumented raft (Figure 5.12). This difference is attributed to the fact that the ADCP could not measure the water velocity within 1 m of the surface; the ADV measured water velocity at a depth of 0.43 m.

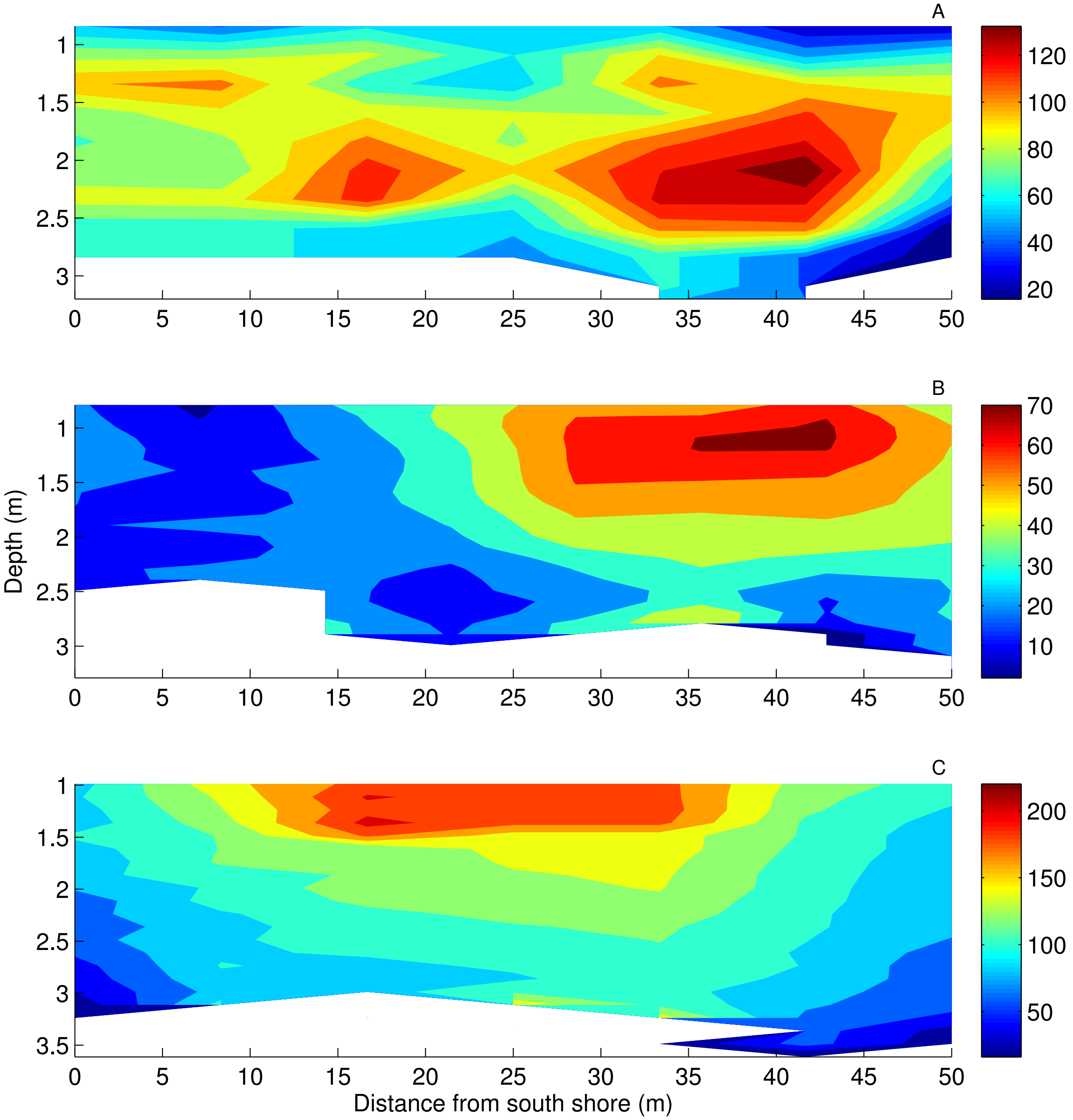

Figure 5.9: Velocity magnitudes (cm s^{-1}) across channel, taken from transects using ADCP for varying tidal conditions: (A) ebb (Case A), (B) slack (Case B), and (C) flood (Cases C1-C2). Transects began at south shore and ended at north shore and were taken at same cross section (dashed line in Figure 5.11).

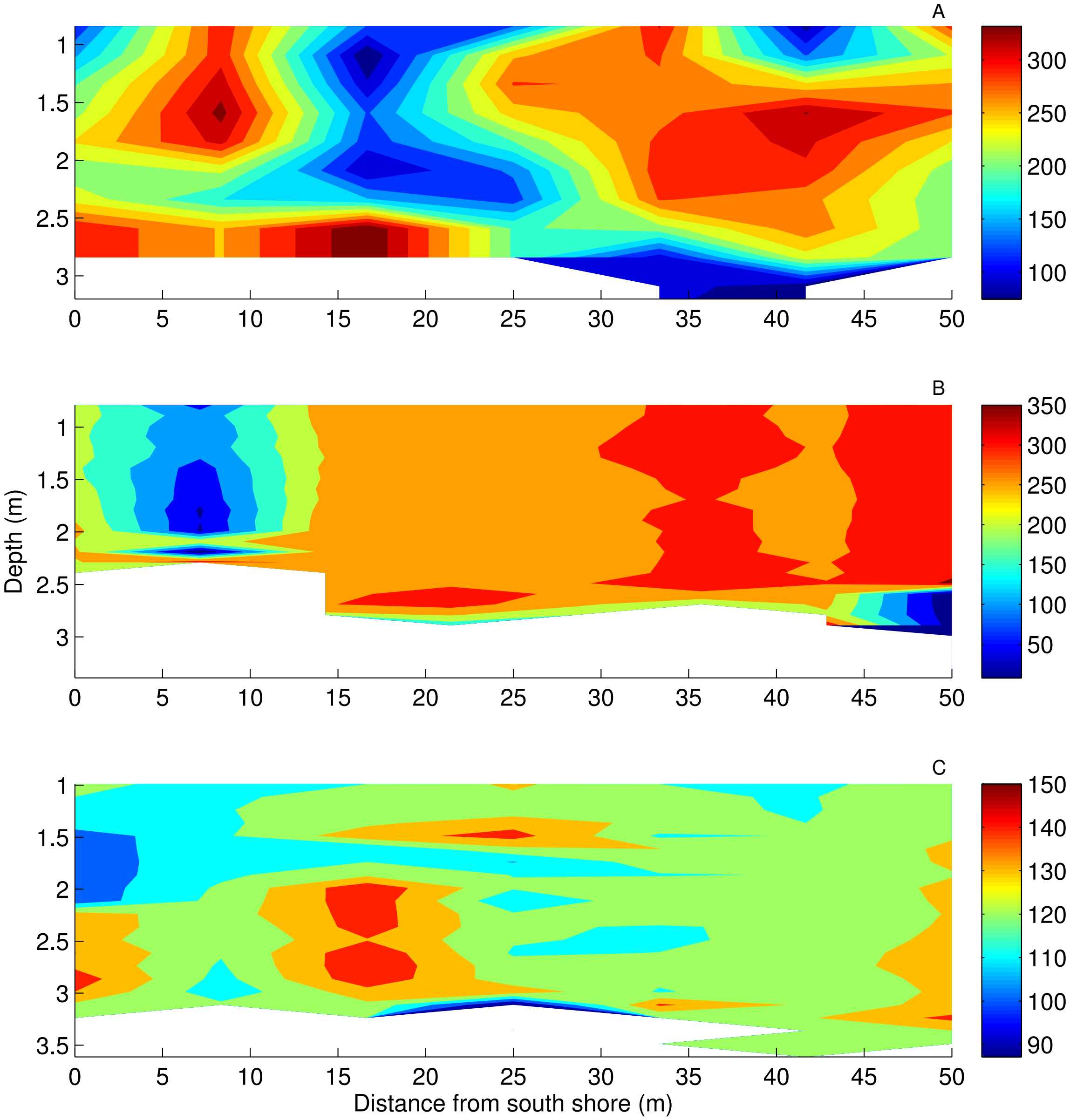

Figure 5.10: Velocity direction along channel cross section, in degrees clockwise from true north, taken from transects using ADCP for varying tidal conditions: (A) ebb (Case A), (B) slack (Case B), and (C) flood (Cases C1-C2). Panels correspond to velocity magnitudes in Figure 5.9.

5.3.2 Raft Trajectories

When present, water currents were the primary driver of raft motion, although wind had measurable effects. During ebb (falling) tide, the water current direction was toward the northwest and the wind direction was toward the east. The raft was primarily transported toward the northwest, with the water current (Case A, Figure 5.11). However, a slight deflection of the raft trajectory toward the east was evident. This deflection off of the primary streamline was presumably caused by the westerly wind. Near slack tide, the water velocity was near zero the wind direction remained toward the east; in this case the raft was transported downwind (Case B, Figure 5.11). During flood (rising) tide, the water current direction was toward the southeast and the wind direction remained toward the east. In this case, the raft was again transported primarily with the water current (Case C, Figure 5.11). As in Case A, a slight deflection of the raft trajectory toward the east was evident in Case C.

5.3.3 Comparison of Velocity Magnitudes

The relative magnitudes of the three velocities measured by the instrumented raft (ADV, raft, and water velocities) varied depending on tidal phase. During ebb tide, the water velocity magnitude was greater than that of both the ADV (relative velocity) and the raft (Figure 5.12A). This is reasonable since one component of the raft velocity was opposed by the wind, which exerts a drag force against the direction of motion. Near slack tide, the water velocity magnitude measured by the instrumented raft was low and approached zero near the predicted timing of slack tide (13:39, Figure 5.7). Coincident with the low water velocity near slack tide (near 13:35, Figure 5.12B), the magnitude of the relative water velocity approached that of the raft velocity, suggesting that water was no longer forcing the raft. During flood tide, the raft velocity magnitude was greater than that of both the ADV and the water (Figure 5.12C-D). During flood tide, the water velocity direction was toward the southeast and the wind direction was toward the east; in this case the easterly component of the raft velocity was aligned with the wind, which exerted a drag force along the direction of motion. For Case C2, the raft and water velocity magnitudes were the highest observed, approaching 30 cm s^{-1}, while the relative velocity magnitude remained low (Figure 5.12D). The highest relative velocities were observed near slack tide (Figure 5.12B).

The raft and water velocities were correlated during ebb and flood tides and anticorrelated during slack tide. During ebb tide, the water velocity was greater than the raft velocity and the correlation coefficient was positive with moderate value (Case A, Figure 5.13 and Table 5.2). During flood tide, the raft velocity exceeded the water velocity and the correlation coefficient was larger (Cases C1-C2, Figure 5.13

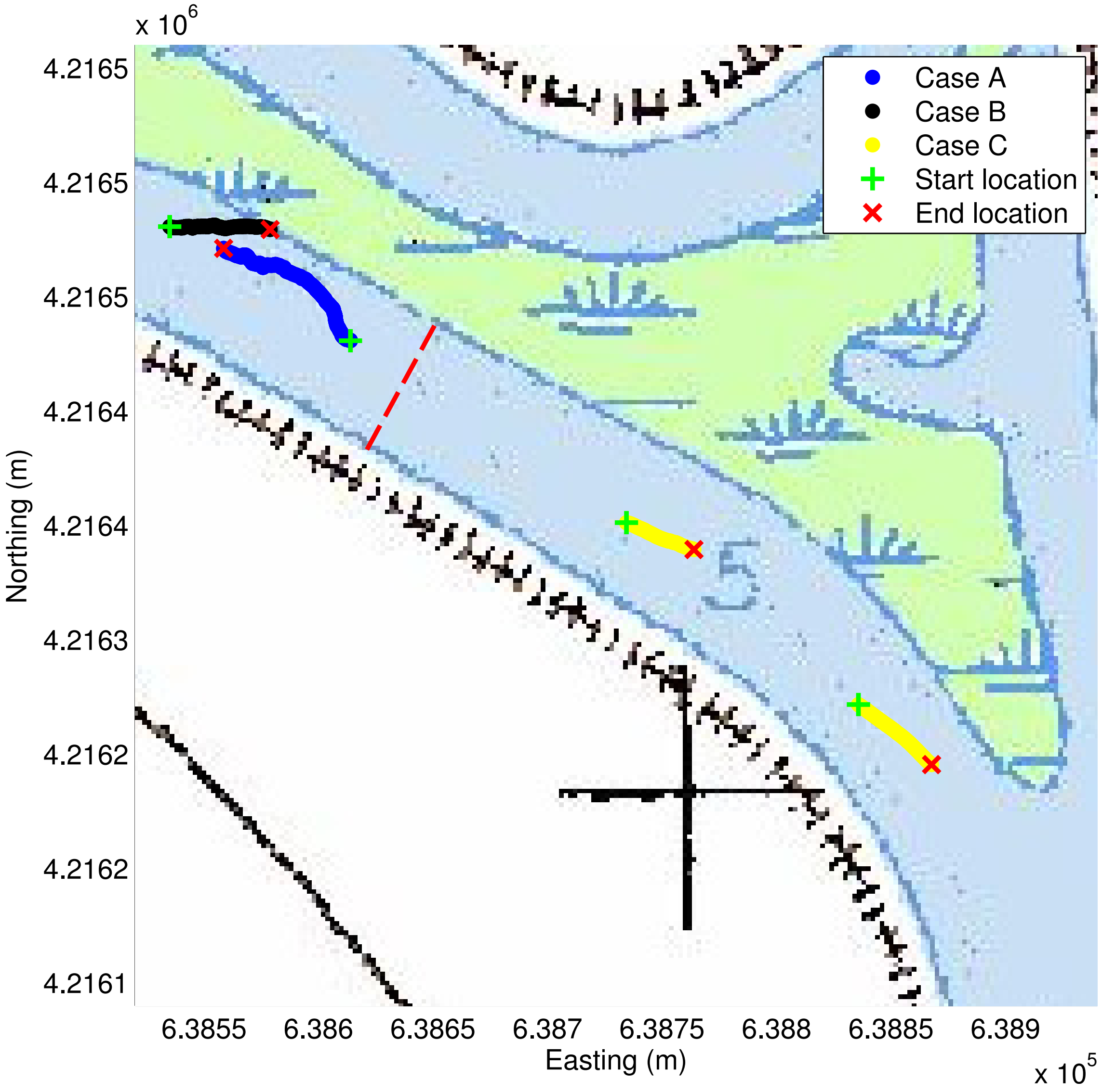

Figure 5.11: Raft trajectories under steady wind forcing and varying tidal conditions: ebb (Case A), slack (Case B), and flood (Case C). Starting and ending positions of the raft are denoted by green + and red × symbols, respectively. The raft trajectories during flood are further subdivided; in subsequent figures the left and right trajectories of Case C are referred to as Cases C1 and C2, respectively. Dashed line denotes location of transects using ADCP (Figures 5.9-5.10).

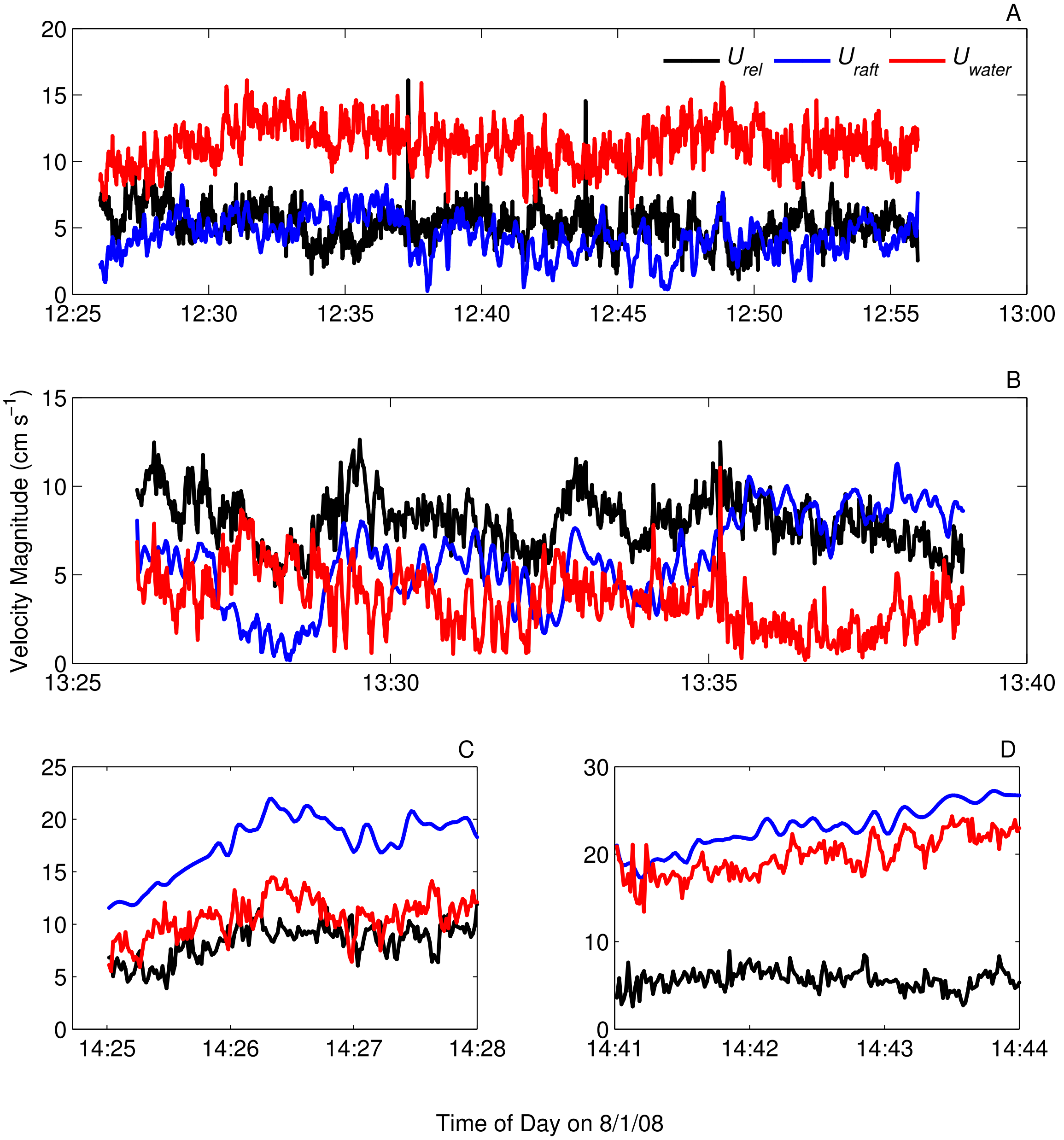

Figure 5.12: Time series of velocity magnitudes from ADV (relative velocity, $||U_{rel}||$), GPS (raft velocity, $||U_{raft}||$), and resulting water velocity ($||U_{water}||$, calculated from Equation (5.1)) for varying tidal conditions: (A) ebb (Case A), (B) slack (Case B), and (C)-(D) flood (Cases C1-C2, respectively).

and Table 5.2). As explained previously, I expect that the opposing components of wind and water velocities during ebb tide caused the lower raft velocity compared to the water velocity; the aligned components of wind and water velocities during flood tide caused the inverse relationship between raft and water velocities. During slack tide, the raft velocity was anticorrelated with water velocity, further suggesting that air forcing dominated transport (Case B, Figure 5.13 and Table 5.2). A similar comparison of air velocity to raft velocity was not possible because of the low sampling rate of the anemometer.

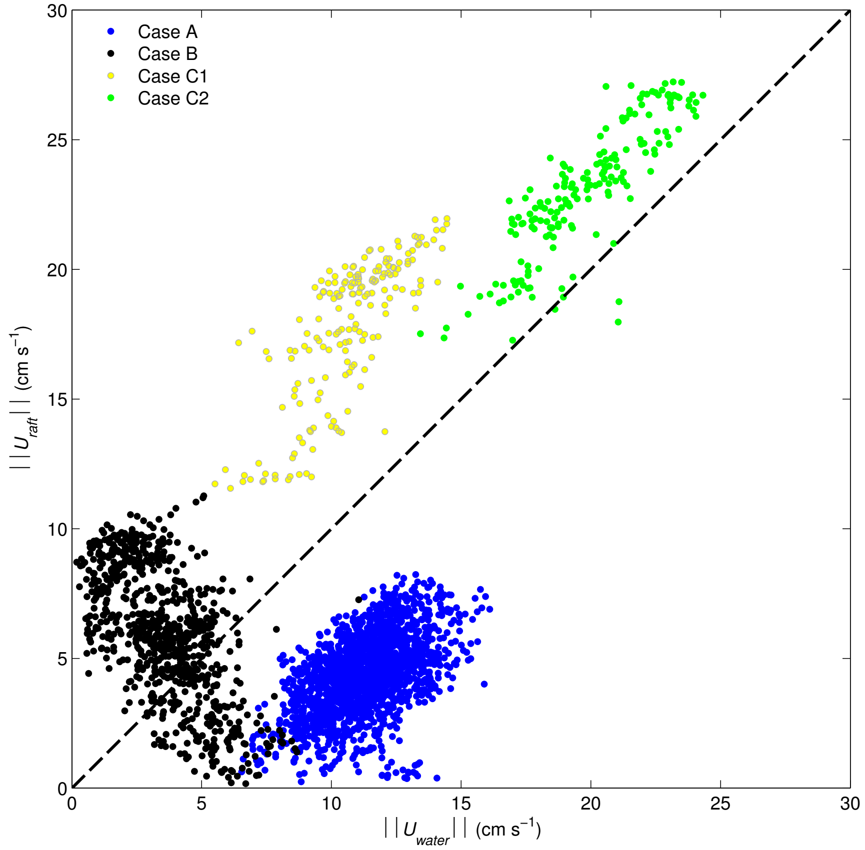

Figure 5.13: Scatter plot of velocity magnitudes for raft ($||U_{raft}||$) versus water ($||U_{water}||$) for ebb (Case A), slack (Case B), and flood (Cases C1 and C2) tide conditions under steady wind forcing. Dashed line denotes where $||U_{raft}|| = ||U_{water}||$.

Table 5.2: Comparison of water and wind headings and correlation coefficients between velocity magnitudes of raft and water for varying tidal conditions.

Case	Tidal Phase	Water Heading	Wind Heading	$(r_{\|\|U_{water}\|\|,\|\|U_{raft}\|\|})$
A	Ebb	NW	E	0.63
B	Slack	—	E	-0.61
C1	Flood	SE	E	0.79
C2	Flood	SE	E	0.92

5.3.4 Comparison of Field and Laboratory Observations

In Chapter 2, I concluded that water currents are expected to control transport of free-floating macrophyte rafts, based on laboratory observations of air- and water-induced drag. The field observations presented here indicate that water currents are the dominant driver of free-floating macrophyte raft transport, further supporting this conclusion. Under constant wind forcing, when water current magnitude was greater than about 5 cm s^{-1}, the rafts were primarily transported with the water current.

Although not the primary forcing mechanism, wind still plays an important role in the net transport of free-floating macrophyte rafts. As evidenced in the raft trajectories during ebb and flood tides (Cases A and C, Figure 5.11), there were obvious deflections of raft motion off the primary axis of the channel. This is assumed to be caused by the wind. Consider a plausible scenario in which wind forces a raft into a stream bank or an alcove. In this case, the raft may become trapped until the wind subsides and water currents are favorable for further transport. This has strong implications for net transport and dispersal of free-floating macrophytes in ecosystems with complex channel geometry (such as the Delta). I expect that free-floating macrophytes will accumulate in quiescent areas of an ecosystem that are downwind of the primary wind direction. For the Delta, which has consistent westerly winds in the summer, accumulation is expected along the eastern shores of slow-moving waters.

One limitation of this experiment was the coarse temporal resolution in wind velocity. Further comparison of wind velocity to raft velocity would strengthen the validity of the conclusions. However, the anemometer record demonstrates the wind was relatively constant in direction and magnitude throughout the experiments. This gives credibility to the primary conclusion that water currents dominate transport. Another limitation was the inability to study the primary species of interest, *E. crassipes*. However, since the morphology of *H. umbellata* is fundamentally similar, these results are indicative of the expected results for *E. crassipes*.

The field site offered an opportunity to study the effects of varying current direction on free-floating macrophyte raft transport, under nearly-constant wind. Further work should be conducted for varying wind velocities, including greater magnitudes. Additional observations in field sites having other hydrologic features of the Delta, such as flooded islands, would offer useful comparison.

As explained in Chapter 2.4.4, I expect that the results of this research are valuable to ecosystem managers. By considering the ambient environmental conditions in an ecosystem, managers can develop an understanding of primary dispersal pathways of free-floating macrophytes like *E. crassipes*. This knowledge is expected to improve the effectiveness of existing control strategies by allowing managers to take a proactive approach to managing an aquatic weed invasion. This approach can be adapted to improve control of other species of aquatic weeds.

5.4 Summary

Field experiments were performed in a tidal channel to observe the effects of varying water velocities on the transport of free-floating macrophyte rafts, under nearly-constant wind velocities. The field site was located in the Delta at the junction of two channels, White Slough and Bishop Cut. A free-floating macrophyte raft was equipped with a GPS and an ADV to measure raft position and relative water velocity. From these data, raft and water velocities were calculated. A boat-mounted ADCP measured velocity across the channel and a ground-based anemometer recorded ambient winds near the field site. Raft trajectories were observed over three phases of a tidal cycle on August 1, 2008: ebb, slack, and flood tides, during which the channel velocity varied in magnitude and direction.

Results indicate that water currents dominated raft transport during ebb and flood tides, and that wind dominated transport during slack tide. Raft and water velocities were correlated during ebb and flood tides and anticorrelated during slack tide. During ebb tide, wind opposed one component of the raft velocity, reducing its magnitude compared to water velocity. In contrast, during flood tide, wind was aligned with one component of the raft velocity, leading to raft velocities that exceeded water velocities.

These field observations corroborate the laboratory results of Chapter 2, suggesting water currents, when present, are the dominant dispersal mechanism for free-floating macrophytes. However, wind plays an important secondary role and must be considered along with ecosystem geometry. The combined research from these field and laboratory experiments forms the basis of a predictive model for free-floating macrophyte dispersal based on physical processes.

Chapter 6

Concluding Remarks

Free-floating macrophyte transport is affected by air and water currents; in turn free-floating macrophytes affect the dynamics of flow in these two fluids. Flow-biota interactions are fundamental controls on both ecological dispersal and water quality impacts. The aim of this research is to gain a better understanding of the physical interactions between free-floating macrophytes and their surrounding flows. Through laboratory and field studies, aspects of these questions have been answered. This research applies existing studies of vegetation canopy dynamics to the relatively unstudied root canopies of free-floating macrophytes.

To assess the effects of flow on free-floating macrophytes, direct force measurements of water and air drag on free-floating *E. crassipes* rafts were obtained from experiments conducted in a flume and a wind tunnel. The force versus flow velocity data were used to estimate drag coefficients in water and air for rafts of varying geometry. Water drag exceeded air drag for similarly-sized rafts over the same Reynolds number regime. Water drag coefficients were stronger functions of Reynolds number than air drag coefficients; this difference is expected to be caused by greater flexibility in root elements compared to leaf canopy elements allowing for root canopy streamlining in higher water velocities. Evaluation of plant biomechanics indicated the roots, stolons, and petioles consist of similar material and the element shape determines flexural rigidity. As root canopy dimensions increased, water drag increased due to increased viscous drag. The flow interacted differently with the root structure of an individual plant compared to that of a raft assemblage.

To assess the effects of free-floating macrophytes on flow, separate laboratory experiments were performed on root and leaf canopies to observe fluid-dynamic effects. For root canopies, the velocity structure around several root canopies was measured using an acoustic Doppler velocimeter in steady flow. In addition, for one canopy a high-resolution vertical profile of velocity was obtained from the region of fully-developed flow; these data were used to examine the details of the turbulent flow structure across the canopy-water interface. Results indicate that the presence of the root canopy in the channel altered the mean and turbulent flow structure. Flow was diverted around the root canopy and turbulence was generated at the canopy-water interface. As upstream water velocity increased, the distance to fully-developed conditions decreased and absolute values of both Reynolds stress and turbulent kinetic energy increased. Velocity profiles beneath the root canopy contained inflection points within the fully-developed region. The detailed vertical profile of mean streamwise velocity had the characteristic shape of a mixing layer, as seen in other forms of vegetated flows, which suggests the presence of hydrodynamic instabilities. The turbulent structure across the canopy-water interface demonstrated similarities to other vegetation canopies, along with important differences. As in other canopies, sweeps were observed at the canopy edge and ejections were observed in the open water beyond. The Reynolds stress profile featured two distinct peaks, a divergence from existing studies of vegetated canopies, perhaps caused by confined flow conditions. Regions of elevated Reynolds stress corresponded to regions of coherent velocity structures. Although turbulent mixing was increased outside the root canopy, very limited turbulent exchange was observed between the root canopy and the open water. This implies low momentum flux across the canopy-water interface; therefore in root canopies having similar structure to *E. crassipes*, residence time is expected to be dominated by horizontal advection.

For leaf canopies, the velocity structure around several leaf canopies was measured using a sonic anemometer in steady flow. In addition, for one canopy a velocity transect was obtained from one height above the canopy; these data were used to compare the effects of canopy length on the flow dynamics. Results indicate that the presence of the leaf canopy in the flow altered the mean and turbulent velocity structure. Flow was diverted around the leaf canopy and turbulence was generated at the canopy-air interface. The spatial development of the mean streamwise velocity profile generally agreed with a model of flow adjustment developed for terrestrial vegetation canopies; four of the five regions of adjustment were observed. Observations of heat flux and Monin-Obukhov length demonstrated that stable, unstratified conditions were present during data collection. As leaf canopy length increased, turbulence intensity, Reynolds stress, and turbulent kinetic energy increased, particularly in the downwind wake region.

Flow fields in water and air were measured for one particular raft to facilitate comparison of the fluid-dynamic effects between these fluids. A low-velocity wake region of similar normalized magnitude developed at the downstream end of both root and leaf canopies; in water there was greater acceleration of the flow outside the canopy and the wake region extended further downstream. Comparing the turbulent flow structures, the normalized Reynolds stress induced by the root canopy was three times that of the leaf canopy. The change in stress between upstream and downstream regions was one order of magnitude greater for the root canopy than for the leaf canopy, signifying the development of a larger-intensity wake region in water. Turbulence intensities in the downstream wake region were 1.5 times greater in water than in air. These results suggest the fluid-dynamic effects of the root canopy exceed those of the leaf canopy.

Field experiments were performed in a tidal channel to observe the effects of varying water velocities on the transport of free-floating macrophyte rafts, under nearly-constant wind velocities. The field site was located in the Delta region of California at the junction of two channels, White Slough and Bishop Cut. A free-floating macrophyte raft was equipped with a global positioning system and an acoustic Doppler velocimeter to measure raft position and relative water velocity. From these data, raft and water velocities were calculated. A boat-mounted current profiler measured velocity across the channel and a ground-based anemometer recorded ambient winds near the field site. Raft trajectories were observed over three phases of a tidal cycle: ebb, slack, and flood tides, during which the channel velocity varied in magnitude and direction. Results indicate that water currents dominated raft transport during ebb and flood tides, and that wind dominated transport during slack tide. Raft and water velocities were correlated during ebb and flood tides and anticorrelated during slack tide. During ebb tide, wind opposed one component of the raft velocity, reducing its magnitude compared to water velocity. In contrast, during flood tide, wind was aligned with one component of the raft velocity, leading to raft velocities that exceeded water velocities. These field observations corroborate the laboratory drag force measurements, suggesting water currents, when present, are the dominant dispersal mechanism for free-floating macrophytes. However, wind plays an important secondary role and must be considered along with ecosystem geometry.

This research takes an innovative approach to invasive species management through the development of a mechanistic transport model; these physically-based models are useful tools for predicting ecological dispersal. An important extension of this research would be to implement the mathematical model of raft transport presented in Chapter 2.1.2 using numerical simulations. The laboratory measurements of drag coefficients and the field observations of raft motions, which are inputs to the model, could be improved in the following aspects: *1*) measure drag forces on shorter leaf canopies using a higher-sensitivity force transducer; and *2*) observe environmental transport of a range of sizes of free-floating macrophyte rafts over longer time scales. For these field observations, the measurement of water velocity below the raft is not recommended. Instead, use only a compact global positioning system directly applied to the raft; this simplified instrumentation will obviate the bulky instrument frame, thereby minimizing disturbances to natural raft motions. The new knowledge presented in this work is valuable to ecosystem managers that control aquatic weed invasions. I expect that consideration of the ambient environmental conditions, particularly the water currents, would improve the effectiveness of existing control strategies. Using this new information, managers would have greater understanding of dispersal pathways and thus be able to take a proactive approach to managing an invasion. For invasions of other species of aquatic weeds, management can be similarly improved by adapting the model presented here.

Bibliography

Ackerman, J. D., and A. Okubo (1993), Reduced mixing in a marine macrophyte canopy, *Functional Ecology*, *7*, 305–309.

Adams, C. S., R. R. Boar, D. S. Hubble, M. Gikungu, D. M. Harper, P. Hickley, and N. Tarras-Wahlberg (2002), The dynamics and ecology of exotic tropical species in floating plant mats: Lake Naivasha, Kenya, *Hydrobiologia*, *488*(1-3), 115–122.

Alben, S., M. Shelley, and J. Zhang (2002), Drag reduction through self-similar bending of a flexible body, *Nature*, *420*(6915), 479–481.

Azza, N., P. Denny, J. van de Koppel, and F. Kansiime (2006), Floating mats: their occurrence and influence on shoreline distribution of emergent vegetation, *Freshwater Biology*, *51*(7), 1286–1297.

Batchelor, G. K. (2000), *An Introduction to Fluid Dynamics*, Cambridge University Press.

Belcher, S. E., N. Jerram, and J. C. R. Hunt (2003), Adjustment of a turbulent boundary layer to a canopy of roughness elements, *Journal of Fluid Mechanics*, *488*, 369–398.

Belcher, S. E., J. J. Finnigan, and I. N. Harman (2008), Flows through forest canopies in complex terrain, *Ecological Applications*, *18*(6), 1436–1453.

Bell, S. S., and M. O. Hall (1997), Drift macroalgal abundance in seagrass beds: Investigating large-scale associations with physical and biotic attributes, *Marine Ecology-Progress Series*, *147*(1-3), 277–283.

Bendat, J. S., and A. G. Peirsol (1986), *Random Data: Analysis and Measurement Procedures*, 2nd ed., John Wiley & Sons Ltd.

Biber, P. D. (2007), Hydrodynamic transport of drifting macroalgae through a tidal cut, *Estuarine Coastal and Shelf Science*, *74*(3), 565–569.

Bicudo, D. D., B. M. Fonseca, L. M. Bini, L. O. Crossetti, C. E. D. Bicudo, and T. Araujo-Jesus (2007), Undesirable side-effects of water hyacinth control in a shallow tropical reservoir, *Freshwater Biology*, *52*(6), 1120–1133.

Bock, J. H. (1969), Productivity of Water Hyacinth Eichhornia Crassipes (Mart.) Solms, *Ecology*, *50*(3), 460–464.

Bouma, T. J., M. B. De Vries, E. Low, G. Peralta, C. Tanczos, J. Van de Koppel, and P. M. J. Herman (2005), Trade-offs related to ecosystem engineering: A case study on stiffness of emerging macrophytes, *Ecology*, *86*(8), 2187–2199.

Boyd, C. E., and E. Scarsbrook (1975), Influence of nutrient additions and initial density of plants on production of water hyacinth, Eichhornia crassipes, *Aquatic Botany*, *1*, 253–261.

Bryan, S. E., A. Cook, J. P. Evans, P. W. Colls, M. G. Wells, M. G. Lawrence, J. S. Jell, A. Greig, and R. Leslie (2004), Pumice rafting and faunal dispersion during 2001-2002 in the Southwest Pacific: record of a dacitic submarine explosive eruption from Tonga, *Earth and Planetary Science Letters*, *227*(1-2), 135–154.

CAIP (1990), Center for Aquatic and Invasive Plants, University of Florida Institute of Food and Agricultural Sciences: Aquatic, Wetland, and Invasive Plants Line Drawings, online.

California Department of Boating and Waterways (2004), Water Hyacinth Control Program Executive Summary, *In* Water Hyacinth and *Egeria densa* 2004 Task Force Meeting, Sacramento, California.

Center, T. D., and N. R. Spencer (1981), The Phenology and Growth of Water Hyacinth (Eichhornia-crassipes (Mart) Solms) in a Eutrophic North-Central Florida Lake, *Aquatic Botany*, *10*(1), 1–32.

Chukwuka, K. S., and U. N. Uka (2007), Effect of water hyacinth (Eichhornia crassipes) infestation on zooplankton populations in Awba reservoir, Ibadan South-West Nigeria, *Journal of Biological Sciences*, *7*(6), 865–869.

Coles, G. C., and N. B. Kabatereine (2008), Water hyacinth and the transmission of schistosomiasis, *Transactions of the Royal Society of Tropical Medicine and Hygiene*, *102*(6), 619–620.

Cook, C. D. K. (1990), *Aquatic Weeds: The Ecology and Management of Nuisance Aquatic Vegetation*, chap. Origin, autecology, and spread of some of the world's most troublesome aquatic weeds, pp. 31–38, Oxford University Press, Oxford.

D'Antonio, C., L. Meyerson, and J. Denslow (2001), Exotic species and conservation - Research needs, in *Conservation Biology: Research Priorities for the Next Decade*, edited by S. M and O. G, pp. 59–80, Island Press, Washington, DC.

Denny, M. W. (1988), *Biology and the Mechanics of the Wave-Swept Environment*, Princeton University Press.

Downing-Kunz, M. A., and M. T. Stacey (2011), Flow-induced forces on free-floating macrophytes, *Hydrobiologia*, *671*, 121–135, doi:10.1007/s10750-011-0709-1.

Downing-Kunz, M. A., and M. T. Stacey (In Review), Observations of mean and turbulent flow structure in a free-floating macrophyte root canopy, *Limnology and Oceanography: Fluids and Environments*.

Drazin, P. G., and W. H. Reid (1981), *Hydrodynamic Stability*, Cambridge University Press.

Ennos, A. R. (1999), The aerodynamics and hydrodynamics of plants, *Journal of Experimental Biology*, *202*(23), 3281–3284.

Fonseca, M. S., M. Koehl, and B. S. Kopp (2007), Biomechanical factors contributing to self-organization in seagrass landscapes, *Journal of Experimental Marine Biology and Ecology*, *340*(2), 227–246.

Francis, L. (1991), Sailing downwind - aerodynamic performance of the Velella sail, *Journal of Experimental Biology*, *158*, 117–132.

Gambi, M. C., A. R. M. Nowell, and P. A. Jumars (1990), Flume observations on flow dynamics in Zostera-marina (Eelgrass) beds, *Marine Ecology-Progress Series*, *61*, 159–169.

Gay, P. A. (1960), Ecological-Studies of Eichhornia-crassipes Solms - In the Sudan 1. Analysis of Spread In the Nile, *Journal of Ecology*, *48*(1), 183–191.

Gaylord, B., C. A. Blanchette, and M. W. Denny (1994), Mechanical consequences of size in wave-swept algae, *Ecological Monographs*, *64*(3), 287–313.

Gaylord, B., J. H. Rosman, D. C. Reed, J. R. Koseff, J. Fram, S. MacIntyre, K. Arkema, C. McDonald, M. A. Brzezinski, J. L. Largier, S. G. Monismith, P. T. Raimondi, and B. Mardian (2007), Spatial patterns of flow and their modification within and around a giant kelp forest, *Limnology and Oceanography*, *52*, 1838–1852.

Ghisalberti, M., and H. Nepf (2002), Mixing layers and coherent structures in vegetated aquatic flows, *Journal of Geophysical Research-Oceans*, *107*(C2), 1–11.

Ghisalberti, M., and H. Nepf (2004), The limited growth of vegetated shear layers, *Water Resources Research*, *40*(7), W07,502.

Ghisalberti, M., and H. Nepf (2006), The structure of the shear layer in flows over rigid and flexible canopies, *Environmental Fluid Mechanics*, *6*, 277–301.

Gillies, J. A., N. Lancaster, W. G. Nickling, and D. M. Crawley (2000), Field determination of drag forces and shear stress partitioning effects for a desert shrub (Sarcobatus vermiculatus, greasewood), *Journal of Geophysical Research-Atmospheres*, *105*(D20), 24,871–24,880.

Gillies, J. A., W. G. Nickling, and J. King (2002), Drag coefficient and plant form response to wind speed in three plant species: Burning Bush (Euonymus alatus), Colorado Blue Spruce (Picea pungens glauca.), and Fountain Grass (Pennisetum setaceum), *Journal of Geophysical Research-Atmospheres*, *107*(D24), 1–15.

Gopal, B. (1987), *Aquatic Plant Studies 1. Water Hyacinth*, Elsevier, New York.

Green, J. C. (2005), Velocity and turbulence distribution around lotic macrophytes, *Aquatic Ecology*, *39*(1), 1–10.

Greene, D. F., and E. A. Johnson (1989), A model of wind dispersal of winged or plumed seeds, *Ecology*, *70*(2), 339–347.

Greenfield, B. K., M. Blankinship, and T. J. McNabb (2006), Control costs, operation, and permitting issues for non-chemical plant control: Case studies in the San Francisco Bay-Delta Region, California, *Journal of Aquatic Plant Management*, *44*, 40–49.

Greenfield, B. K., G. S. Siemering, J. C. Andrews, M. Rajan, S. P. Andrews, and D. F. Spencer (2007), Mechanical shredding of water hyacinth (Eichhornia crassipes): Effects on water quality in the Sacramento-San Joaquin River Delta, California, *Estuaries and Coasts*, *30*(4), 627–640.

Gunnarsson, C. C., and C. M. Petersen (2007), Water hyacinths as a resource in agriculture and energy production: A literature review, *Waste Management*, *27*(1), 117–129.

Heard, T. A., and S. L. Winterton (2000), Interactions between nutrient status and weevil herbivory in the biological control of water hyacinth, *Journal of Applied Ecology*, *37*(1), 117–127.

Henry-Silva, G. G., A. F. M. Camargo, and M. M. Pezzato (2008), Growth of free-floating aquatic macrophytes in different concentrations of nutrients, *Hydrobiologia*, *610*, 153–160.

Hibbeler, R. C. (2000), *Mechanics of Materials*, 4th ed., Prentice Hall, Upper Saddle River, New Jersey.

Higgins, S. I., and D. M. Richardson (1996), A review of models of alien plant spread, *Ecological Modelling*, *87*(1-3), 249–265.

Higgins, S. I., D. M. Richardson, and R. M. Cowling (1996), Modeling invasive plant spread: The role of plant-environment interactions and model structure, *Ecology*, *77*(7), 2043–2054.

Ho, C. M., and P. Huerre (1984), Perturbed Free Shear Layers, *Annual Review of Fluid Mechanics*, *16*, 365–424.

Hoerner, S. F. (1965), *Fluid Dynamic Drag: Practical Information on Aerodynamic Drag and Hydrodynamic Resistance*, Hoerner Fluid Dynamics.

Ikeda, S., and M. Kanazawa (1996), Three-dimensional organized vortices above flexible water plants, *Journal of Hydraulic Engineering-Asce*, *122*, 634–640.

Iosilevskii, G., and D. Weihs (2009), Hydrodynamics of sailing of the Portuguese man-of-war Physalia physalis, *Journal of the Royal Society Interface*, *6*(36), 613–626.

Jayanth, K. P. (1988), Successful biological-control of water hyacinth (Eichhornia-crassipes) by Neochetina-eichhorniae (coleoptera, curculionidae) in Bangalore, India, *Tropical Pest Management*, *34*(3), 263–266.

Jongejans, E., O. Skarpaas, and K. Shea (2008), Dispersal, demography and spatial population models for conservation and control management, *Perspectives in Plant Ecology Evolution and Systematics*, *9*(3-4), 153–170.

Kundu, P., and I. Cohen (2004), *Fluid Mechanics*, 3rd ed., Elsevier.

Lockwood, J., M. Hoopes, and M. Marchetti (2007), *Invasion ecology*, Blackwell Publishing.

Lu, S. S., and W. W. Willmarth (1973), Measurements of the structure of the Reynolds stress in a turbulent boundary layer, *Journal Of Fluid Mechanics*, *60*, 481–511.

Lugo, A. E., G. R. Utsch, M. M. Brinson, and E. Kane (1978), Metabolism and biomass of water-hyacinth Eichhornia crassipes dominated ponds and canals in the vicinity of Gainesville, Florida, *Geo-Eco-Trop*, *2*(4), 415–441.

Mackie, G. L. (2004), *Applied Aquatic Ecosystem Concepts*, Kendall/Hunt.

Madsen, T. V., and E. Warncke (1983), Velocities of currents around and within submerged aquatic vegetation, *Archiv Fur Hydrobiologie*, *97*, 389–394.

Malik, A. (2007), Environmental challenge vis a vis opportunity: The case of water hyacinth, *Environment International*, *33*(1), 122–138.

Masifwa, W. F., T. Twongo, and P. Denny (2001), The impact of water hyacinth, Eichhornia crassipes (Mart) Solms on the abundance and diversity of aquatic macroinvertebrates along the shores of northern Lake Victoria, Uganda, *Hydrobiologia*, *452*(1-3), 79–88.

Mazzeo, N., J. Gorga, D. Crosa, J. Ferrando, and W. Pintos (1995), Spatial and temporal variation of physicochemical parameters in a shallow reservoir seasonally covered by Pistia-stratiotes L in Uruguay, *Journal of Freshwater Ecology*, *10*(2), 141–149.

Meerhoff, M., N. Mazzeo, B. Moss, and L. Rodriguez-Gallego (2003), The structuring role of free-floating versus submerged plants in a subtropical shallow lake, *Aquatic Ecology*, *37*(4), 377–391.

Mishra, V. K., and B. D. Tripathi (2008), Concurrent removal and accumulation of heavy metals by the three aquatic macrophytes, *Bioresource Technology*, *99*, 7091–7097.

Mitsch, W. J. (1976), Ecosystem modeling of water-hyacinth management in Lake Alice Florida USA, *Ecological Modelling*, *2*(1), 69–89.

Molina-Aiz, F. D., D. L. Valera, A. J. Alvarez, and A. Madueno (2006), A wind tunnel study of airflow through horticultural crops: Determination of the drag coefficient, *Biosystems Engineering*, *93*(4), 447–457.

Morse, A. P., B. A. Gardiner, and B. J. Marshall (2002), Mechanisms controlling turbulence development across a forest edge, *Boundary-Layer Meteorology*, *103*(2), 227–251.

Naden, P., P. Rameshwaran, O. Mountford, and C. Robertson (2006), The influence of macrophyte growth, typical of eutrophic conditions, on river flow velocities and turbulence production, *Hydrological Processes*, *20*(18), 3915–3938.

Nathan, R., and H. C. Muller-Landau (2000), Spatial patterns of seed dispersal, their determinants and consequences for recruitment, *Trends in Ecology & Evolution*, *15*(7), 278–285.

Nepf, H. M., and E. R. Vivoni (2000), Flow structure in depth-limited, vegetated flow, *Journal of Geophysical Research-Oceans*, *105*(C12), 28,547–28,557.

Ngari, A. N., J. I. Kinyamario, M. J. Ntiba, and K. M. Mavuti (2009), Factors affecting abundance and distribution of submerged and floating macrophytes in Lake Naivasha, Kenya, *African Journal of Ecology*, *47*(1), 32–39.

Opande, G. O., J. C. Onyango, and S. O. Wagai (2004), Lake Victoria: The water hyacinth (Eichhornia crassipes Mart. Solms), its socio-economic effects, control measures and resurgence in the Winam gulf, *Limnologica*, *34*, 105–109.

Padial, A. A., S. M. Thomaz, and A. A. Agostinho (2009), Effects of structural heterogeneity provided by the floating macrophyte Eichhornia azurea on the predation efficiency and habitat use of the small Neotropical fish Moenkhausia sanctaefilomenae, *Hydrobiologia*, *624*, 161–170.

Pauchard, A., and K. Shea (2006), Integrating the study of non-native plant invasions across spatial scales, *Biological Invasions*, *8*(3), 399–413.

Penfound, W. T., and T. T. Earle (1948), The biology of the Water Hyacinth, *Ecological Monographs*, *18*, 447–472.

Pieterse, A. H., and K. J. Murphy (1990), *Aquatic Weeds*, Oxford University Press, Oxford.

Pimentel, D., L. Lach, R. Zuniga, and D. Morrison (2000), Environmental and economic costs of nonindigenous species in the United States, *Bioscience*, *50*(1), 53–65.

Poggi, D., A. Porporato, L. Ridolfi, J. D. Albertson, and G. G. Katul (2004), The Effect of Vegetation Density on Canopy Sub-Layer Turbulence, *Boundary-Layer Meteorology*, *111*, 565–587.

Raupach, M. R. (1992), Drag and Drag Partition on Rough Surfaces, *Boundary-Layer Meteorology*, *60*(4), 375–395.

Raupach, M. R., and A. S. Thom (1981), Turbulence in and above plant canopies, *Annual Review of Fluid Mechanics*, *13*, 97–129.

Raupach, M. R., R. A. Antonia, and S. Rajagopalan (1991), Rough-Wall Turbulent Boundary Layers, *Applied Mechanics Reviews*, *44*(1), 1–25.

Raupach, M. R., J. J. Finnigan, and Y. Brunet (1996), Coherent eddies and turbulence in vegetation canopies: The mixing-layer analogy, *Boundary-Layer Meteorology*, *78*, 351–382.

Reddy, K. R., and D. L. Sutton (1984), Waterhyacinths for water quality improvement and biomass production, *Journal of Environmental Quality*, *13*, 1–8.

Reddy, K. R., and J. C. Tucker (1983), Productivity and nutrient-uptake of water hyacinth, Eichhornia-crassipes 1. Effect of nitrogen-source, *Economic Botany*, *37*, 237–247.

Reddy, K. R., M. Agami, and J. C. Tucker (1989), Influence of nitrogen supply rates on growth and nutrient storage by water hyacinth (Eichhornia-crassipes) plants, *Aquatic Botany*, *36*(1), 33–43.

Sand-Jensen, K. (2003), Drag and reconfiguration of freshwater macrophytes, *Freshwater Biology*, *48*(2), 271–283.

Sand-Jensen, K., and J. Mebus (1996), Fine-scale patterns of water velocity within macrophyte patches in streams, *Oikos*, *76*, 169–180.

Sanford, L., and S. Crawford (2000), Mass transfer versus kinetic control of uptake across solid-water boundaries, *Limnology and Oceanography*, *45*, 1180–1186.

Schurr, F. M., W. J. Bond, G. F. Midgley, and S. I. Higgins (2005), A mechanistic model for secondary seed dispersal by wind and its experimental validation, *Journal of Ecology*, *93*(5), 1017–1028.

Sculthorpe, C. D. (1967), *The Biology of Aquatic Vascular Plants*, Edward Arnold, London.

Shaffer, J. A., D. C. Doty, R. M. Buckley, and J. E. West (1995), Crustacean community composition and trophic use of the drift vegetation habitat by juvenile splitnose rockfish Sebastes diploproa, *Marine Ecology-Progress Series*, *123*(1-3), 13–21.

Smith, S. D. (1993), Hindcasting iceberg drift using current profiles and winds, *Cold*

Regions Science and Technology, *22*(1), 33–45.

Stewart, H. L. (2004), Hydrodynamic consequences of maintaining an upright posture by different magnitudes of stiffness and buoyancy in the tropical alga Turbinaria ornata, *Journal of Marine Systems*, *49*, 157–167.

Stewart, H. L. (2006), Hydrodynamic consequences of flexural stiffness and buoyancy for seaweeds: a study using physical models, *Journal of Experimental Biology*, *209*(11), 2170–2181.

Stull, R. B. (1994), *An Introduction to Boundary Layer Meteorology*, Kluwer Academic Publishers.

Thiel, M., and P. A. Haye (2006), The ecology of rafting in the marine environment. III. Biogeographical and evolutionary consequences, in *Oceanography and Marine Biology - an Annual Review, Vol 44*, *Oceanography and Marine Biology*, vol. 44, pp. 323–429, Crc Press-Taylor & Francis Group, Boca Raton.

Thorndike, A. S., and R. Colony (1982), Sea ice motion in response to geostrophic winds, *Journal of Geophysical Research-Oceans and Atmospheres*, *87*, 5845–5852.

Tinka, A., I. Strub, Q. Wu, and A. M. Bayen (2010), Quadratic programming based data assimilation with passive drifting sensors for shallow water flows, *International Journal Of Control*, *83*(8), 1686–1700.

Toft, J. D., C. A. Simenstad, J. R. Cordell, and L. F. Grimaldo (2003), The effects of introduced water hyacinth on habitat structure, invertebrate assemblages, and fish diets, *Estuaries*, *26*(3), 746–758.

Usherwood, J. R., A. R. Ennos, and D. J. Ball (1997), Mechanical and anatomical adaptations in terrestrial and aquatic buttercups to their respective environments, *Journal of Experimental Botany*, *48*(312), 1469–1475.

Vogel, S. (1984), Drag and flexibility in sessile organisms, *American Zoologist*, *24*(1), 37–44.

Weber, J. E., and J. Debernard (2000), Slowly drifting sea ice with a corrugated underside, *International Journal of Offshore and Polar Engineering*, *10*(1), 41–49.

White, B. L., and H. M. Nepf (2007), Shear instability and coherent structures in shallow flow adjacent to a porous layer, *Journal of Fluid Mechanics*, *593*, 1–32.

Wilson, J. R., N. Holst, and M. Rees (2005), Determinants and patterns of population growth in water hyacinth, *Aquatic Botany*, *81*(1), 51–67.

Wolverton, B. C., and R. C. McDonald (1979), Water hyacinth (Eichhornia-crassipes) productivity and harvesting studies, *Economic Botany*, *33*(1), 1–10.

Yi, C. X. (2008), Momentum transfer within canopies, *Journal of Applied Meteorology* *and Climatology*, *47*(1), 262–275.

Yi, Q., C. Hur, and Y. Kim (2009), Modeling nitrogen removal in water hyacinth ponds receiving effluent from waste stabilization ponds, *Ecological Engineering*, *35*, 75–84.

Appendix A

Material Properties of *E. crassipes* Structures

Table A.1: Material properties of root structures of *E. crassipes*, determined via tensile stress-extension tests. For each specimen the following properties are presented: initial length (L_0); length at rupture (L_1); extension ratio ($\lambda = L_1/L_0$); initial diameter (d_0); diameter at rupture (d_1); moment of inertia (I); modulus of elasticity (E); and flexural rigidity (EI). See Chapter 2.2.6 for details of testing and calculations.

Specimen	L_0 (cm)	L_1 (cm)	λ [-]	d_0 (mm)	d_1 (mm)	I (m^4)	E (N m^{-2})	EI (N m^2)
1	6.4	7.06	1.10	1.1	0.8	2.44×10^{-14}	3.96×10^{7}	9.67×10^{-7}
2	7.3	8.12	1.12	1.2	1.0	4.17×10^{-14}	6.78×10^{7}	2.83×10^{-6}
3	7.0	7.50	1.07	1.3	1.1	6.68×10^{-14}	6.22×10^{7}	4.15×10^{-6}
4	4.0	4.40	1.10	1.0	0.9	3.22×10^{-14}	5.08×10^{7}	1.64×10^{-6}
5	3.5	3.88	1.11	1.4	1.3	1.49×10^{-13}	2.87×10^{7}	4.27×10^{-6}
6	2.6	3.15	1.21	1.0	0.9	3.22×10^{-14}	1.98×10^{7}	6.39×10^{-7}
7	3.8	4.33	1.14	1.1	0.9	3.22×10^{-14}	1.59×10^{7}	5.12×10^{-7}
8	4.0	4.40	1.10	1.1	1.1	6.68×10^{-14}	5.75×10^{7}	3.84×10^{-6}

Table A.2: Material properties of petiole structures of *E. crassipes*, determined via cantilever beam deflection tests. For each specimen the following properties are presented: moment arm length (L); major axis diameter (d_1); minor axis diameter (d_2); bending stiffness (F/w); moment of inertia (I); modulus of elasticity (E); and flexural rigidity (EI). See Chapter 2.2.6 for details of testing and calculations.

Specimen	L (cm)	d_1 (mm)	d_2 (mm)	$L^3/3$ (m^3)	F/w (N m^{-1})	I (m^4)	E (N m^{-2})	EI (N m^2)
1	4.0	5.7	4.2	2.13×10^{-5}	16.05	2.07×10^{-11}	1.65×10^{7}	3.42×10^{-4}
2	5.0	5.7	4.2	4.17×10^{-5}	8.75	2.07×10^{-11}	1.76×10^{7}	3.64×10^{-4}
3	4.5	5.7	4.2	3.04×10^{-5}	8.11	2.07×10^{-11}	1.19×10^{7}	2.46×10^{-4}
4	4.5	5.7	4.2	3.04×10^{-5}	8.57	2.07×10^{-11}	1.26×10^{7}	2.60×10^{-4}
5	5.0	5.7	4.2	4.17×10^{-5}	11.35	2.07×10^{-11}	2.28×10^{7}	4.73×10^{-4}
6	5.0	5.7	4.2	4.17×10^{-5}	9.00	2.07×10^{-11}	1.81×10^{7}	3.75×10^{-4}
7	4.8	5.7	4.2	3.57×10^{-5}	6.51	2.07×10^{-11}	1.12×10^{7}	2.33×10^{-4}
8	4.8	5.3	3.6	3.57×10^{-5}	7.54	1.21×10^{-11}	2.23×10^{7}	2.69×10^{-4}
9	4.8	5.3	3.6	3.57×10^{-5}	9.72	1.21×10^{-11}	2.87×10^{7}	3.47×10^{-4}
10	4.5	5.8	4.3	3.04×10^{-5}	11.40	2.28×10^{-11}	1.52×10^{7}	3.46×10^{-4}
11	4.5	5.8	4.3	3.04×10^{-5}	9.12	2.28×10^{-11}	1.22×10^{7}	2.77×10^{-4}
12	4.8	4.3	2.9	3.69×10^{-5}	3.66	5.07×10^{-12}	2.66×10^{7}	1.35×10^{-4}
13	4.8	4.3	2.9	3.69×10^{-5}	3.99	5.07×10^{-12}	2.90×10^{7}	1.47×10^{-4}
14	3.0	4.6	4.1	9.00×10^{-6}	10.10	1.52×10^{-11}	5.98×10^{6}	9.09×10^{-5}
15	3.0	4.6	4.1	9.00×10^{-6}	3.91	1.52×10^{-11}	2.32×10^{6}	3.52×10^{-5}
16	3.0	4.1	3.6	9.00×10^{-6}	10.24	9.34×10^{-12}	9.86×10^{6}	9.22×10^{-5}
17	3.2	4.6	3.5	1.09×10^{-5}	6.31	9.43×10^{-12}	7.31×10^{6}	6.89×10^{-5}
18	3.4	4.2	2.5	1.31×10^{-5}	3.18	3.30×10^{-12}	1.26×10^{7}	4.17×10^{-5}
19	2.9	4.2	3.0	8.13×10^{-6}	5.69	5.57×10^{-12}	8.31×10^{6}	4.62×10^{-5}
20	6.2	7.6	5.4	7.94×10^{-5}	6.43	5.84×10^{-11}	8.74×10^{6}	5.11×10^{-4}
21	5.5	5.4	4.3	5.55×10^{-5}	5.54	2.14×10^{-11}	1.44×10^{7}	3.07×10^{-4}
22	3.8	5.5	3.7	1.83×10^{-5}	3.33	1.39×10^{-11}	4.37×10^{6}	6.09×10^{-5}

Table A.3: Material properties of stolon structures of *E. crassipes*, determined via cantilever beam deflection tests. For each specimen the following properties are presented: moment arm length (L); major axis diameter (d_1); minor axis diameter (d_2); bending stiffness (F/w); moment of inertia (I); modulus of elasticity (E); and flexural rigidity (EI). See Chapter 2.2.6 for details of testing and calculations.

Specimen	L (cm)	d_1 (mm)	d_2 (mm)	$L^3/3$ (m^3)	F/w ($N\ m^{-1}$)	I (m^4)	E ($N\ m^{-2}$)	EI ($N\ m^2$)
1	5.0	4.8	4.2	4.17×10^{-5}	9.61	1.75×10^{-11}	2.29×10^{7}	4.00×10^{-4}
2	4.5	4.8	3.6	3.04×10^{-5}	1.92	1.10×10^{-11}	5.31×10^{6}	5.84×10^{-5}
3	5.3	4.8	4.1	4.82×10^{-5}	2.23	1.60×10^{-11}	6.72×10^{6}	1.08×10^{-4}
4	5.5	5.2	4.4	5.55×10^{-5}	4.53	2.22×10^{-11}	1.13×10^{7}	2.51×10^{-4}
5	5.3	5.0	4.2	4.82×10^{-5}	3.40	1.83×10^{-11}	8.95×10^{6}	1.64×10^{-4}
6	5.3	5.3	4.6	4.96×10^{-5}	9.45	2.46×10^{-11}	1.91×10^{7}	4.69×10^{-4}
7	5.7	5.0	4.2	6.17×10^{-5}	7.34	1.83×10^{-11}	2.47×10^{7}	4.53×10^{-4}
8	5.5	4.1	3.5	5.55×10^{-5}	2.81	8.44×10^{-12}	1.85×10^{7}	1.56×10^{-4}
9	5.4	3.8	3.5	5.25×10^{-5}	1.71	7.94×10^{-12}	1.13×10^{7}	8.95×10^{-5}
10	4.8	5.3	5.2	3.69×10^{-5}	11.44	3.56×10^{-11}	1.18×10^{7}	4.22×10^{-4}
11	5.4	5.5	4.8	5.25×10^{-5}	10.42	3.00×10^{-11}	1.83×10^{7}	5.47×10^{-4}
12	3.5	3.7	3.1	1.43×10^{-5}	6.03	5.55×10^{-12}	1.55×10^{7}	8.62×10^{-5}
13	4.4	3.6	3.1	2.84×10^{-5}	2.58	5.37×10^{-12}	1.36×10^{7}	7.32×10^{-5}
14	5.0	4.7	4.1	4.17×10^{-5}	7.02	1.56×10^{-11}	1.87×10^{7}	2.93×10^{-4}
15	5.0	4.7	4.6	4.17×10^{-5}	6.67	2.18×10^{-11}	1.28×10^{7}	2.78×10^{-4}
16	4.9	4.8	4.3	3.92×10^{-5}	7.00	1.90×10^{-11}	1.44×10^{7}	2.74×10^{-4}
17	5.0	4.7	4.3	4.17×10^{-5}	5.64	1.85×10^{-11}	1.27×10^{7}	2.35×10^{-4}
18	5.2	4.6	4.0	4.69×10^{-5}	4.60	1.39×10^{-11}	1.55×10^{7}	2.16×10^{-4}
19	4.7	4.4	3.7	3.46×10^{-5}	3.30	1.12×10^{-11}	1.02×10^{7}	1.14×10^{-4}
20	4.7	4.7	4.1	3.46×10^{-5}	6.42	1.56×10^{-11}	1.42×10^{7}	2.22×10^{-4}
21	5.5	4.7	3.8	5.55×10^{-5}	5.73	1.30×10^{-11}	2.44×10^{7}	3.18×10^{-4}